Design Optimisation of a High Intensity Beam Facility and Feasibility Experiment of a Solid Fragmented Target

THÈSE N^{O} 6162 (2014)

PRÉSENTÉE LE 13 JUIN 2014
À LA FACULTÉ DES SCIENCES DE BASE
LABORATOIRE DE PHYSIQUE DES ACCÉLÉRATEURS DE PARTICULES
PROGRAMME DOCTORAL EN PHYSIQUE

ÉCOLE POLYTECHNIQUE FÉDÉRALE DE LAUSANNE

POUR L'OBTENTION DU GRADE DE DOCTEUR ÈS SCIENCES

PAR

Nikolaos CHARITONIDIS

acceptée sur proposition du jury:

Prof. H. M. Rønnow, président du jury
Prof. L. Rivkin, Dr I. Efthymiopoulos, directeurs de thèse
Dr D. Kiselev, rapporteuse
Dr N. Simos, rapporteur
Dr T. Stora, rapporteur

ÉCOLE POLYTECHNIQUE
FÉDÉRALE DE LAUSANNE

Suisse
2014

This page was intentionally left blank

To Prof. Sofia Lambropoulou

For lighting up and holding the candle of my knowledge throughout the gloomy way - For teaching me who I want to be.

Thank you

Abstract

The present PhD thesis describes the design, execution and results of the HRMT-10 experiment performed at the HiRadMat facility of the CERN/SPS complex. The first part of the thesis covers the design optimization studies of the HiRadMat facility, focusing in particular on the radiation protection issues. A detailed Monte-Carlo model of the facility has been developed and validated through comparison with measurements. A very satisfactory agreement between the simulation and the experimental data is observed.

In the second part of this thesis, a novel feasibility experiment of a fragmented solid target for a future Neutrino Factory or a Super Beam facility, able to support high beam powers ($\geq 1\ MW$) is presented in detail. A solid granular target has been proposed as an interesting alternative to an open Hg jet target, presently considered as the baseline for such facilities, but posing considerable technical challenges. The HRMT-10 experiment seeks to address the lack of experimental data of the feasibility of a tungsten powder as such a target.

The instrumentation of the experiment was based on remote high-speed photography as well as on Laser-Doppler vibration measurements of the target containers (through a mirror setup and behind a specially designed shielding). The behavior of the powder as a function of the beam parameters is analyzed, and the different disruptive effects observed due to the beam impact are described. For the first time, the proton induced velocities of powder filaments were measured. Values of up to 1.5 m/s for a proton bunch intensity of 2.94×10^{11} at 440 GeV were observed. A theoretical model of the behavior of the target after the impact of the beam has been developed, and is found to be in good agreement with the experimental data.

The extrapolation from the measured disruption speeds to the nominal beam parameters of a Neutrino Factory show a projected maximum speed of 30 m/s for the powder grains. This speed appears to pose no practical problems for any foreseeable type of container, and therefore tungsten powder can be considered as a valid option for a future high-power beam facility able to support $\geq 1\ MW$ of beam power.

Keywords : high power targets, neutrino factory, feasibility experiment, beam-material interaction

Résumé

La présente thèse de doctorat décrit la conception, l'exécution et les résultats de l'expérience HRMT-10 effectuée à l'installation HiRadMat située au CERN/SPS. La première partie de cette thèse traite des études d'optimisation de HiRadMat, se focalisant en particulier sur des questions de radioprotection. Un modèle Monte-Carlo détaillé de cette installation a été développé et évalué par le biais de comparaison entre les mesures expérimentales : on constate un accord très satisfaisant entre la simulation et ces dernières.

Dans la seconde partie, une nouvelle expérience de faisabilité sur une cible solide fragmentée pour un futur Neutrino Factory ou une installation Super Beam, capable de soutenir des faisceaux de forte puissance (> 1MW), y est présentée en détail. Une cible granulaire est proposée alors comme une intéressante alternative à une cible d'un jet de Hg, actuellement considérée comme la base de telles installations, faisant cependant preuve de considérables défis techniques. Le HRMT – 10 tente ainsi d'aborder le manque de données expérimentales de la faisabilité d'une cible de poudre de tungsten comme telle.

L'instrumentation de l'expérience a été fondée sur la photographie haute vitesse à distance, tout comme sur le mesurage de vibrations Laser-Doppler des conteneurs de la cible Le comportement de la cible en fonction des paramètres du faisceau y est analysé, et les différentes disruptions observées dues à l'impact du faisceau y sont décrites. Les vitesses des filaments de la poudre, induites des protons, ont été mesurées pour la première fois. Des valeurs allant jusqu'à 1.5 m/s pour une intensité de faisceau de protons de 2.94 $\times 10^{11}$ à 440 GeV ont été observées. Un modèle théorique du comportement de la cible après l'impact du faisceau a été développé, lequel s'accorde parfaitement avec les données expérimentales.

L'extrapolation de la vitesse de disruption mesurée à partir des paramètres nominaux du faisceau d'un Neutrino Factory, prévoie une vitesse maximale des grains de poudre de 30 m/s. Cette vitesse semble ne poser aucun problème pratique pour tout type de conteneur, et, par conséquent, la poudre de tungsten peut être considérée comme une option valide pour une future installation de forte puissance de faisceau, capable de soutenir > 1 MW.

Mots-clés : cibles de forte puissance, neutrino factory, expérience de faisabilité, interaction faisceau - materiel

Acknowledgments

"Give credit where credit is due"

Many persons contributed with their own way in the completion of this thesis. However, in this section I would like to express my greatest gratitudes to the following persons, since without their active contribution, the completion of this work would be impossible.

Dr. Ilias EFTHYMIOPOULOS, my CERN supervisor. There are not enough words to express my gratitudes to him. From the first moment of my entrance in EN-MEF-LE section, he started to inspire me and, without demotivating me, to explain me how to cope with the difficulties that I would have to face if I wanted to learn physics. Always setting the highest level of excellency even at the smallest piece of scientific work, he taught me with his way to face the challenges of research in physical sciences, being reassuring when I was crossing the valleys of depression, and always respecting my opinion during some occasional disagreements on the road to be followed. He stood as nothing less but a father to me, and I hope that we will continue our collaboration. Ήταν "θέμα χημείας" ! Ευχαριστώ !

Dr. Adrian FABICH. It was an incredible windfall for me, that the one person that did a similar thesis with me 10 years ago, co-supervised my analysis. From his first moment in the section, Adrian was actively interested in my work, treating my thesis with the same interest as if it were his own work, and teaching me not to be afraid of software codes. Always willing to be interrupted by me from his full schedule in order to discuss my new results with me, he taught me to be irreconcilable with "less than perfect" quality of work, and, without even being my official supervisor, he was demanding from me to "stand on my feet" and being innovative, scientific & precise. Thank you, Adrian !

Prof. Leonid RIVKIN. Without Prof. Rivkin this thesis would have never taken place; he gave me the unique opportunity of being enrolled as a doctoral student in EPFL. Despite his very busy schedule, Lenny was always there to resolve any problem that could appear, and give his scientific opinion for my thesis, always being reassuring and without stressing me. Thank you !

The HiRadMat design & operation team. During the design phase of the facility, I worked with many persons each one of them taught me something different. Hereby I want to thank: Chris THEIS and Helmut VINCKE for their valuable help in HiRadMat's radiation protection studies; Michael LAZZARONI who helped me with the experimental drawings, and showed me how to interact with the technical personnel; Catherine MAGNIER answered all my pedantic questions concerning distances & materials; Aboubakr EBN RAHMOUN (Abou) provided me with his everlasting support when a crazy idea was generated in my mind, and he had his way to make things work; Dino DE PAOLI, for his continuous presence in the experimental area and his prompt replies and willingness to help concerning every aspect of the facility; Jerome LENDARO willingly answered my numerous questions concerning the cables and electronics of the facility and the experiments, and gave me his support even at last moment's notice; Kurt WEISS, with his smile and his strict style, was always there for HiRadMat, and even in weekends he posed himself available to allow, as radio-protection official, access in the facility. Ans PARDONS and Sebastien EVRARD for being always willing to give me any information on dimensions, materials & construction details despite my "intrusion" in their office. Thank you very much !

The "RAL" team, Drs: Chris DENSHAM, Ottone CARETTA, Peter LOVERIDGE and Tristan DAVENNE, for their contribution in designing the experiment. We had a nice time during the data taking and very useful discussions of scientific nature! Foreseeing our next collaboration :)

Marco SILARI, my MSc thesis supervisor, with his everlasting interest in my PhD thesis and my work, giving me useful ideas and proposing new experimental challenges. His prompt replies to my e-mails always relieved my stress, and his friendly behavior created a comfortable work environment. I hope to the continuation of our collaboration !

My life at CERN had as basis the habitants of b. 530. Each and everyone of them contributed to my daily happiness with their own way: Michael JECKEL, David McFARLANE and Lau GATIGNON for stopping by my office and telling me important stuff concerning science or not; Erwan HARROUCH for smiling at me and stealing my tea; Marlene TURNER for always stopping by my office to press me for coffee brakes; Gersende PRIOR for her scientific interest and willingness to discuss with me any subject of scientific or personal life; Theo RUTTER for giving a tone of smile and optimism in the building; Yisel MARTINEZ-PALENZUELA for her jokes and chocolates; Gianluca CANALE and Mats WILHEMSSON for keeping the building in place; Also Sylvain GIROD for having always beers to offer. Thank you all guys!

Without the Greek gang@Suisse, life would be way too boring; Andrea(s) with whom we spend weeknights, weekdays and weekends working in my office, discussing several aspects of our thesis, playing with the high-speed camera and the vibrometer, always together *learning* physics. We had one another; and we will continue...Anna with her smile organizing activities that nobody else would; Matina, maybe the best cooker around; Manto and Christos for sharing with me their inner thoughts about the future;

Vittorio for the "Mizzika" Saturday mornings; Athina, Iosifina & Sofia for the nights @ Cheval Blanc 16, with songs & coffee; Domna, Vasilis, Alkisti & Stasa for taking care of my outnumbered teeth; Nathalie for the french courses and a lot of more things; Love you all guys!

Ole - Martin HANSEN & Bartolomej BISKUP, both deserve a special note. The officemate during a PhD thesis is like a roommate; he shares with you your happiness, your sadness, and he is there to support you in the difficult (and not difficult!) times! Hardly there are words to describe how much I enjoyed you being my *friends* guys. I hope we manage to stay in touch...I was lucky to meet you!

My sister Eleni and my parents, Polydoros & Litsa know that there is no need for acknowledgments here. They have been always believing in my choices and supporting them without doubt...! Thank you !

Two more persons need to be mentioned here. S. that was here when everything started, and her back-then motivation. L., with whom I shared every day of the last difficult months...and she was there trying very hard to relieve my stress. Thank you, I will do the same for you...!

The research leading to these results has received funding from the European Commission under the FP7 Capacities project ***EuCARD****, grant agreement no.* ***227579****.*

Contents

1 Introduction

1.1 Beam-Material Interactions

The heating of materials exposed to intense, high-energy particle beams has been observed since the early years of accelerators. More specifically, when a highly energetic particle beam impinges on a material, thermal effects caused by the direct energy deposition of the beam particles are induced to the material. Additionally, since the duration of the particle burst is in the order of microseconds or even shorter, the heating of the irradiated material proceeds in times during which heat conduction is negligible [1, 2] and therefore mechanical stresses are created by this rapid non-uniform temperature increase.

Stresses caused by non-uniform heating in general have been extensively studied in the framework of *Thermoelasticity*, for which extensive literature is available (for example, see [3]). Nevertheless, the study of the stress waves caused by a particle beam and their impact on the target materials lacks experimental and theoretical data. A first theoretical approach for simple geometries began in the 1970's [4], along with some experiments [5]. The present theoretical framework [6, 7] states that these induced thermo-mechanical stresses can be categorized into three dynamic regimes, as a function of increasing deposited energy: elastic stress waves, plastic stress waves and shock waves.

The common practice when the design of near beam components or targets is concerned, is to rely on the simulated prediction of the material behavior under the effect of the beam by advanced, highly non-linear numerical tools and Monte−Carlo simulation codes. The means of computation of the energy deposition from the beam is performed using sophisticated physics models based on cross-section libraries and high-energy hadronic and electromagnetic models of the particle interactions with the matter. This energy deposition map of the material is then imported either in standard finite element codes (e.g ANSYS ®) or Hydrocodes [8] for the calculation of the stresses and the induced deformation. These computational codes and tools are mainly based on mathematical models that are poorly or not at all validated with experimental data [9, 10].

1.2 Accelerator Components and Beam Targets

In modern accelerators, injectors or colliders like the **S**uper **P**roton **S**ync-hrotron (SPS) [11] or **L**arge **H**adron **C**ollider (LHC) [12], two main issues should be carefully considered, from material point of view: (a) the correct design of the near beam components, that must be able to receive the full beam power without structural failure and (b) the target design.

A prime example concerning the latter is neutrino physics, a field that is relatively unexplored. The production of neutrinos can only be achieved through the interaction of primary, highly energetic protons with a target. In the case of CNGS [13] or a perspective Neutrino Factory [14], the flux of the secondary pions that decay to muons and subsequently in neutrinos must be as much as possible in order to allow the study of these particles. Due the high power (~4MW) of the primary beam, the design of a target system able to accept such a beam becomes challenging.

It is therefore imperative to validate the simulation results for such target systems, and to evaluate the existing models before they can be trusted for future target designs. Since the only way for these unknown phenomena to be studied is through experimental observation, several experiments of damage to LHC collimators, as well as on material robustness under the effect of the beam have been performed in the past [15] at **C**onseil **E**uropéen pour la **R**echerche **N**ucléaire (CERN) and elsewhere [16, 17, 18, 19]. Despite these efforts, the exact mechanisms that dominate the propagation of these thermal phenomena in solid, liquid and granular targets are, until today, far from being well understood.

The majority of the aforementioned experiments and tests have been performed on temporary installations or beam line facilities, with the corresponding planning difficulties and the safety issues from potential impact on the operating beam lines. For these reasons, it was decided to build a dedicated facility for performing experiments that would allow the study of beam - material interactions at CERN.

1.3 The HiRadMat Facility

1.3.1 Beam line

The **Hi**gh **Rad**iation to **Mat**erials (HiRadMat) facility is located in the CERN West Area [20, 21]. The primary proton or ion beam is extracted from SPS (Figure 1.1). The nominal proton momentum is 440 GeV/c. The beam structure consists of several pulses, each one consisting of a number of bunches. The proton beam parameters available in HiRadMat are summarized in Table 1.1.

The SPS is operated in a so-called "multicycling" mode: the machine continuously runs a repetitive sequence of beam injections, accelerations and extractions of various particles, serving all the experimental areas and facilities of CERN. These repetitive sequences are called "supercycles". The SPS supercycle serving HiRadMat has a duration of either 16.8 s (short supercycle) or 44 s (long supercycle), depending on the beam parameters chosen each time. Once per this time interval, the beam can be extracted to the facility through a dedicated, newly constructed extraction beam line.

This extraction beam line, given the code name “TT66”, was designed to offer great flexibility in the beam parameters (intensity, spot size, horizontal and vertical position) in order to serve the purpose and specifications of each experiment [22].

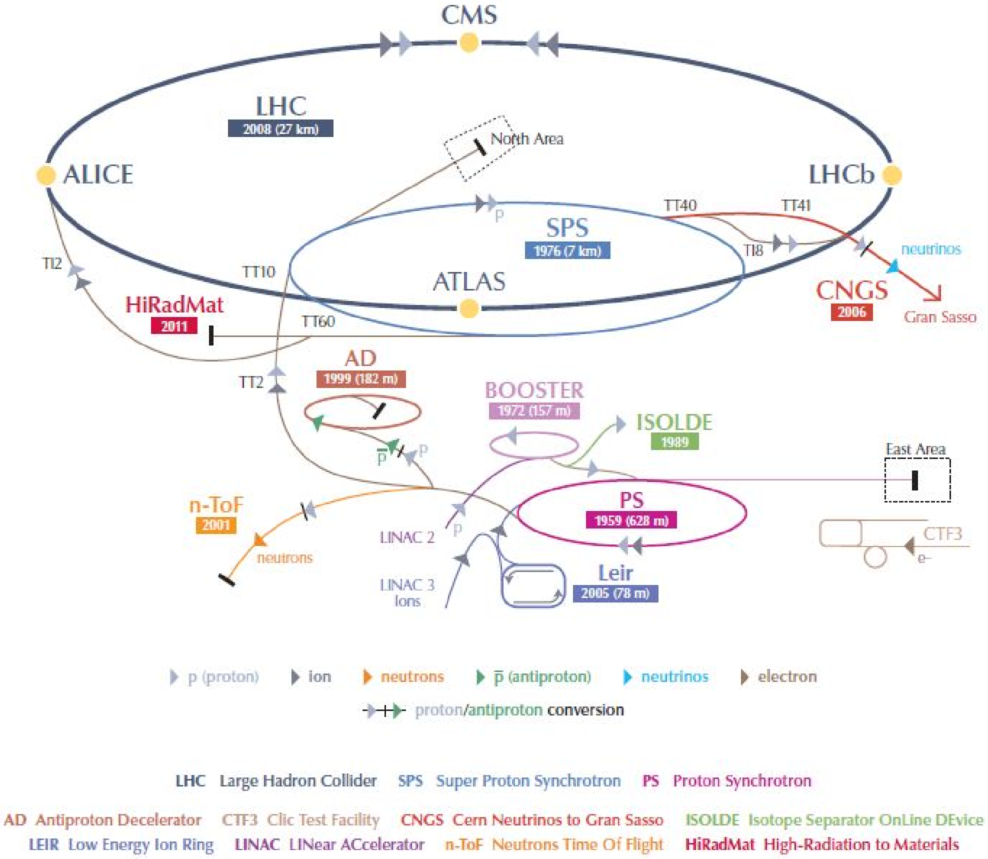

Figure 1.1: *Schematic view of the CERN accelerator complex*

Parameter	Value
Energy	440 GeV
Bunch Intensity (max)	1.7×10^{11} protons
Number of bunches	1 up to 288
Pulse Intensity (max)	4.9×10^{13} protons
Bunch Length	11.24 cm
Bunch Spacing	25, 50, 75, 150 ns
Pulse length	7.2 μs

Table 1.1: *The HiRadMat beam parameters. Depending on the specific needs of each experiment, the number of bunches per pulse, the bunch spacing, as well as the total number of extractions can be adjusted.*

The beam is extracted from the SPS and then is transported for ~200 m to the HiRad-

Mat experimental area, where it is focused on the test objects. The beam focal points can be found in Figure 1.2, while the beam dump is located at a distance of 4 m beyond focal point 3.

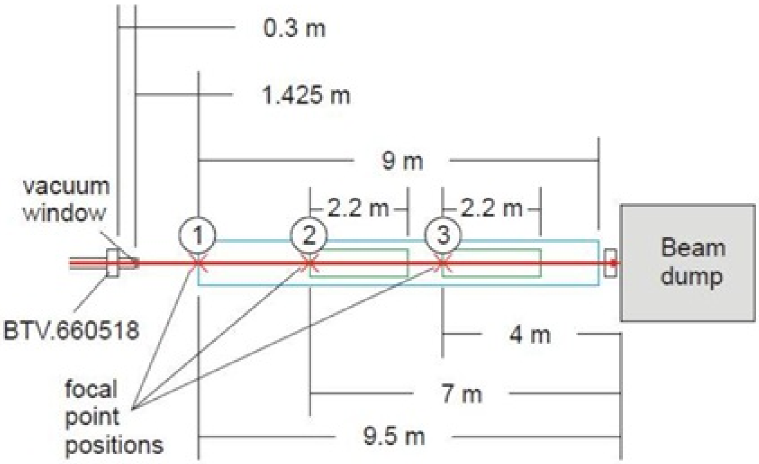

Figure 1.2: *The focal points of the HiRadMat beam (1-3), with the corresponding distances from the beam dump and the final window of the beam line. For more information see [22, 23].*

1.3.2 Layout

HiRadMat is integrated in the CERN's existing underground tunnel infrastructure. It consists of the surface access building (given in the CERN convention of buildings and tunnels the code name "BA7"), an access shaft equipped with an elevator (code name "PA7"), an interconnecting tunnel (code name: "TA7"), the experiment preparatory area (code name: "TJ7") and the experimental area tunnel (code name "TNC"). Tha facility is located about 35 m below the surface level. A 2D technical drawing of the underground areas is shown in Figure 1.3. A 3D representation of the tunnel infrastructures can be found in Figure 1.4 while a 3D drawing of the experimental area can be seen in Figure 1.5.

Access of personnel and material to the underground areas of HiRadMat is possible through the surface building BA7, using factory-type elevators. While the background ambient dose equivalent ($H^*(10)$) in the TA7 and TJ7 tunnels is around 3 $\mu Sv/h$, the dose is significantly higher in the TNC tunnel, due to the activation of the beam dump. Therefore, access in the TNC experimental area is generally prohibited, and allowed only under special circumstances and the consent of the responsible Radiation Protection Officer.

1.3.3 Experimental Area

A photo of the HiRadMat experimental area can be seen in Figure 1.6. The experimental area covers the final 10 m after the end of the TT66 beam line and up to the beam dump. At that point, three special stands ("base tables") were designed and installed. The

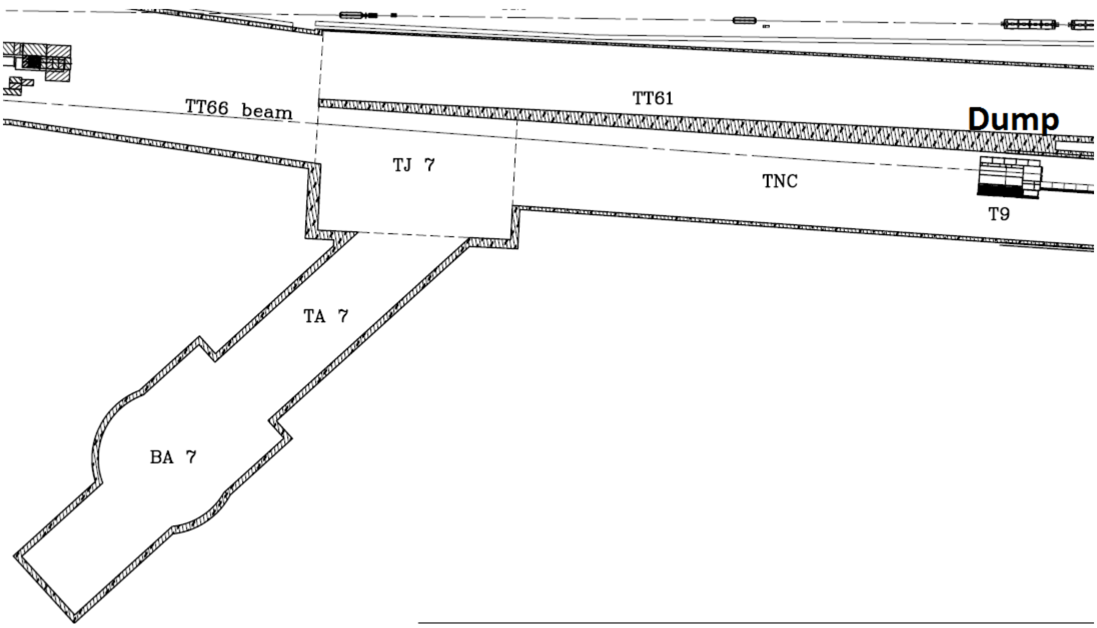

Figure 1.3: *HiRadMat Underground Areas Drawing. The names of the underground areas are marked. As discussed in the text, HiRadMat consists mainly of the access area tunnel (TA7), the preparation area tunnel (TJ7) and the experimental area tunnel (TNC).*

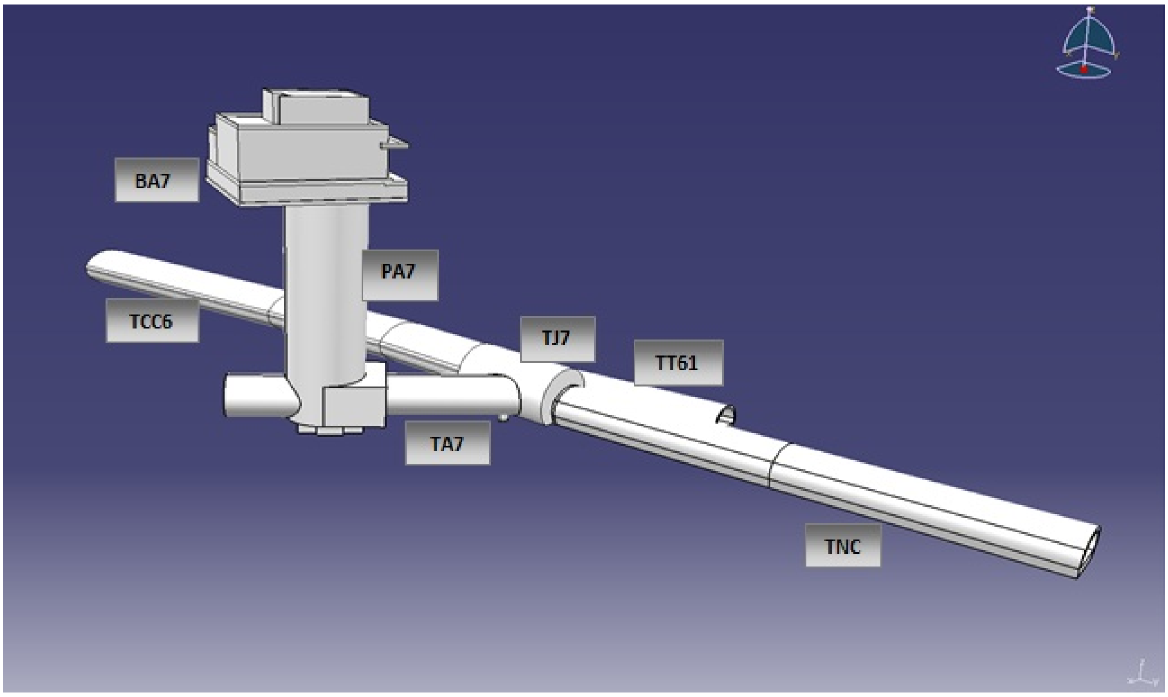

Figure 1.4: *HiRadMat Tunnel Layout 3D model.*

positioning of the base tables (each with a length of ~2.2 m) corresponds to the beam focal points (for details, see [23]). Apart from these base tables, several mobile stands ("mobile tables") that can be remotely mounted on the base tables with the use of an

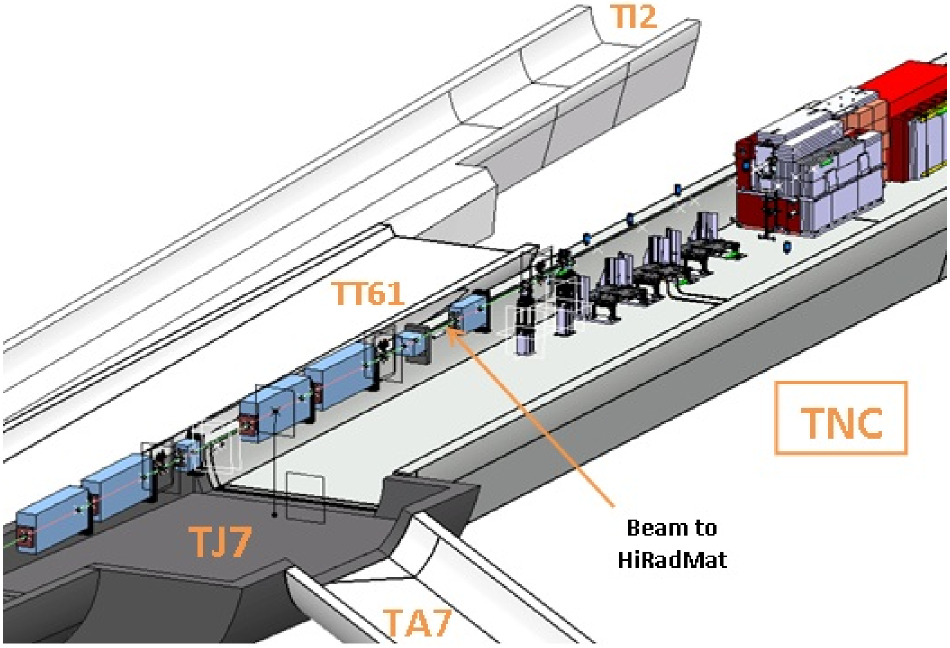

Figure 1.5: *HiRadMat underground areas. The newly constructed beam line (given the code name "TT66") and the beam dump appear inside TNC tunnel.*

overhead crane have been designed and manufactured. Each experimental setup can be installed on one mobile table and then be remotely transported to the experimental area. The purpose of this procedure is to facilitate the setup of the experiments that can be completed in the surface or in the preparatory TJ7 tunnel, while minimizing the dose to which the personnel is exposed. On the base and mobile tables, a system of generic connectors has been installed in order to be used by the experimental teams, either for providing electrical power or for data acquisition purposes. For technical details concerning the HiRadMat experimental area as well as the manipulation of the mobile tables, one may consult the facility's safety file [24].

Figure 1.6: *Photo of the HiRadMat Experimental Area. The end of the TT66 beam line can be seen. Installed on the middle base table, a mobile table with an installed experiment is shown. The beam dump is situated 7 m beyond the experiment.*

2 Radiation Protection Studies for HiRadMat

Since HiRadMat is designed with the purpose of hosting beam-material interactions experiments and not as an irradiation facility where large doses on equipment can be accumulated, it was decided that a maximum of 10^{16} protons per year will be delivered to the facility by the SPS. This proton budget would be shared amongst 10 experiments on average per operation year.

The radiation protection studies for such a facility are of high concern for the following reasons:

- The design of the facility had to be done in such a way that, the surface and underground areas of the facility had to be classified accordingly in order to define the access of the personnel during the operation of the facility, as well as during the no-beam periods. The limits defined by CERN for the classification of the areas [25] for non permanent workplaces can be found in Table 2.1.

Type of Area	**Maximum Dose Equivalent Rate ($\mu Sv/h$)**	**Access**
Non Designated	< 2.5 $\mu Sv/h$	No Restriction
Supervised	< 15 $\mu Sv/h$	Supervised by RP
Simple Controlled	< 50 $\mu Sv/h$	Controlled by RP
Limited Stay	< 2 mSv/h	Controlled by RP
High Radiation	< 100 mSv/h	Controlled by RP
Prohibited	> 100 mSv/h	Controlled by RP

Table 2.1: *Classification of radiation areas by CERN Radiation Safety Code. Only the limits concerning the non-permanent workplaces are shown.*

- After each experiment, workers and scientists have to access the irradiation area in order to install the equipment for the forthcoming experiment. The background radiation from the beam dump or the activated tunnel equipment (beam line elements, walls of the tunnel, etc.) may contribute to an increased radiation dose to these persons. Therefore, the background radiation levels have to be closely examined and access to the area must be planned accordingly.

- The activated objects, after the irradiation, are transported in a special "cool down" zone, almost 100 m downstream of the HiRadMat experimental area. The cooling time for such an operation has to be calculated beforehand for each experiment, and be constantly monitored with the appropriate radiation monitoring systems.

For the aforementioned reasons, studies at the design phase, addressing the above issues and consequently providing guidelines and optimization loops were very important and obligatory, since they defined the operational envelope for the facility. The results of the radiation protection studies are presented in the following sections.

2.1 Monte − Carlo Simulation framework

The radiation protection studies for HiRadMat were carried out through a combination of Monte−Carlo simulations and predictions made via analytical models. The chosen code for these simulations was FLUKA [26, 27], alongside with the graphical front-end FLAIR [28]. FLUKA was chosen among other codes since is very well benchmarked in radiation protection studies and accelerator physics (for example, see [29, 30, 31]).

Since HiRadMat was a new facility, the Monte-Carlo model of the surface and underground areas had to be designed from the beginning. In Figure 2.1, the model of the geometry implemented for the simulations is shown.

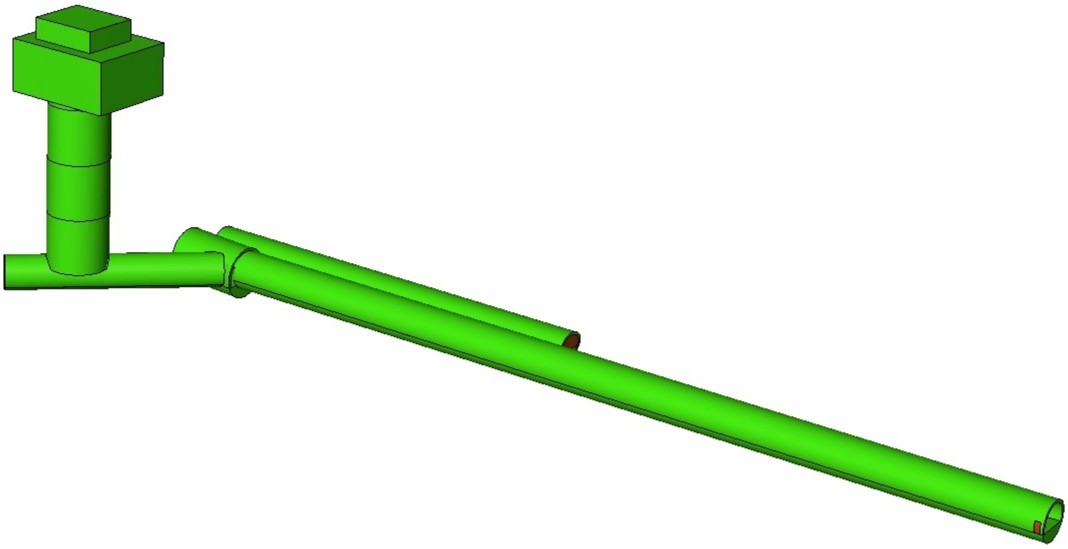

Figure 2.1: *The FLUKA model designed for the HiRadMat area, visualized with Simple-Geo® [32]*

The newly created HiRadMat model is based on the civil engineering plans and is very accurate in terms of dimensions of the tunnel and building structures. Small differences exist due to the fact that the exact physical geometry of the structures is not always possible to model using only fixed shapes and regions.

Concerning the beam line elements, the beam dump [33], and the electromechanical equipment present in the facility, only the elements that would significantly contribute to the prompt or activation dose rate were modeled and they are in absolute agreement with the engineering drawings.

2.2 Simulation Scenarios

For the purpose of these studies, several sets of simulations have been performed. In all the presented results, an average of 10 experiments per year, each one of them using 10^{15} protons, is assumed as a nominal operation scenario for the facility. For better presentation of the results, the studies have been divided into four categories: (a) prompt dose calculations, (b) activation calculations, (c) background calculations and (d) cooling water calculations.

2.2.1 Prompt Ambient Dose Equivalent Rate Calculations

In the prompt calculations scenario, the nominal HiRadMat beam is simulated to impinge on an "optimum target" (copper rod of 1 m length and a radius of 3 cm). This target is placed at focal point 1 of the irradiation area (see Figure 1.2 for the beam focal points). This "optimum target" configuration yields an interaction probability of 99.9% for the beam particles and thus can be regarded as the envelope case for the prompt radiation to be expected from the facility in normal operation mode. This position of the target was chosen because it represents the closest one of the perspective experimental positions to the surface building, which should be accessible from the personnel during operation, since it hosts the facility's control room. A visualization of the model used for these studies can be seen in Figure 2.2.

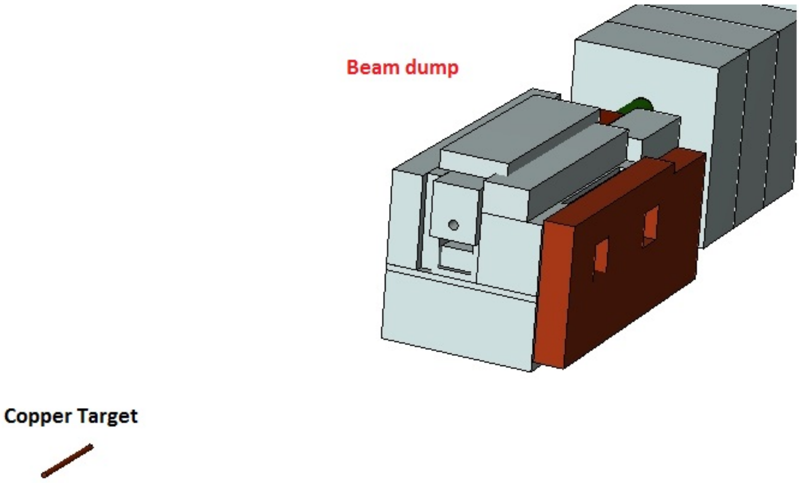

Figure 2.2: *The model of the copper target placed at focal point 1. The beam impinges on the target from the left side. The different colors correspond to the different construction materials of the dump.*

The quantities scored in all the underground areas (TNC, TJ7, TA7) as well as in the surface building (BA7) were:

1. *Ambient Dose Equivalent* ($H^*(10)$), given in terms of $\mu Sv/h$ normalized with respect to two SPS cycles: The long one (a total of 10^{15} protons spread over 30 extractions, with the duration of the supercycle equal to 44 seconds) and the short one (a total of 10^{15} protons spread over 30 extractions, with the duration of the supercycle equal to 16.8 seconds). In addition, an operational envelope scenario was studied, consisting of a total of 4.89×10^{15} protons spread over 100 extractions, each one lasting 20 s.

2. *The 1MeV equivalent neutron fluence* [34] in TNC, TJ7 and TA7 tunnels. This fluence is a general quantifier of displacement effects (also referred to as "**N**on-**I**onizing **E**nergy **L**oss") (NIEL).

3. *The fluence of hadrons with E > 20MeV* in all the aforementioned tunnels. High-energy hadrons are considered to be most dangerous for the equipment, since their cross sections for creating displacement effects are quite high. For more information on the cross sections and relative experiments, one may consult [35].

Surface buildings

In order for the safety of the personnel and the environment to be ensured, the dose rate on the surface building (code name "BA7") was calculated. The results for the operational envelope scenario can be seen in Figure 2.3.

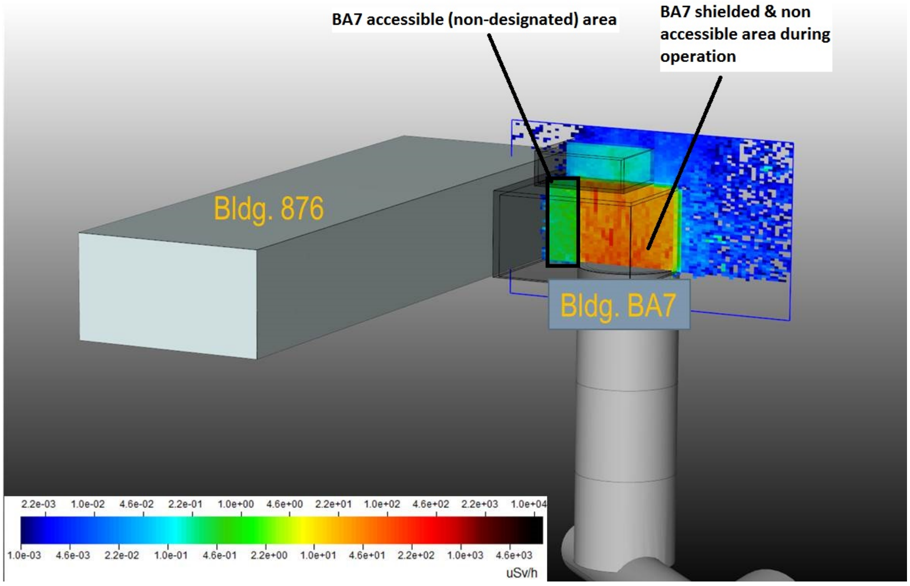

Figure 2.3: *The calculated dose rate at the accessible areas as well as the roof of the surface building for the operational envelope scenario is less than 0.4 $\mu Sv/h$. The total uncertainty of the simulation is less than 10 %.*

Since the dose rate in BA7 for the worst-case scenario was calculated to be less than $0.4\ \mu Sv/h$, all the accessible areas of the facility were classified as "non-designated areas". That means that unreserved access can be given to the personnel, even during the facility's operation. Furthermore, the existing shielding of the building roof was proven to be sufficient even in the case of necessary construction works on the roof of this building during the operation of the facility.

An accident scenario was also studied. The highest doses in publicly accessible areas around BA7 are to be expected in case of a beam loss on equipment, e.g., a magnet, which is located in the TJ7 tunnel and as such, closest to the access shaft leading to the surface buildings. In order to simulate such a situation under worst-case conditions, the previously described optimum target was placed in TJ7, on line of sight with respect to the access tunnel TA7.

Figure 2.4 illustrates the results. It was calculated that outside the building the highest expected dose equals ~$5 \times 10^{-15} \pm 25\ \%\ \mu Sv$ per lost proton. Therefore, in the improbable case that the full proton load of one experiment (10^{15} protons) is lost unnoticed, the total dose for such an event is expected to be ~$5\ \mu Sv$ in publicly accessible areas outside the building, while a total dose of ~$20\ \mu Sv$ or less is expected at the accessible by CERN users surface areas.

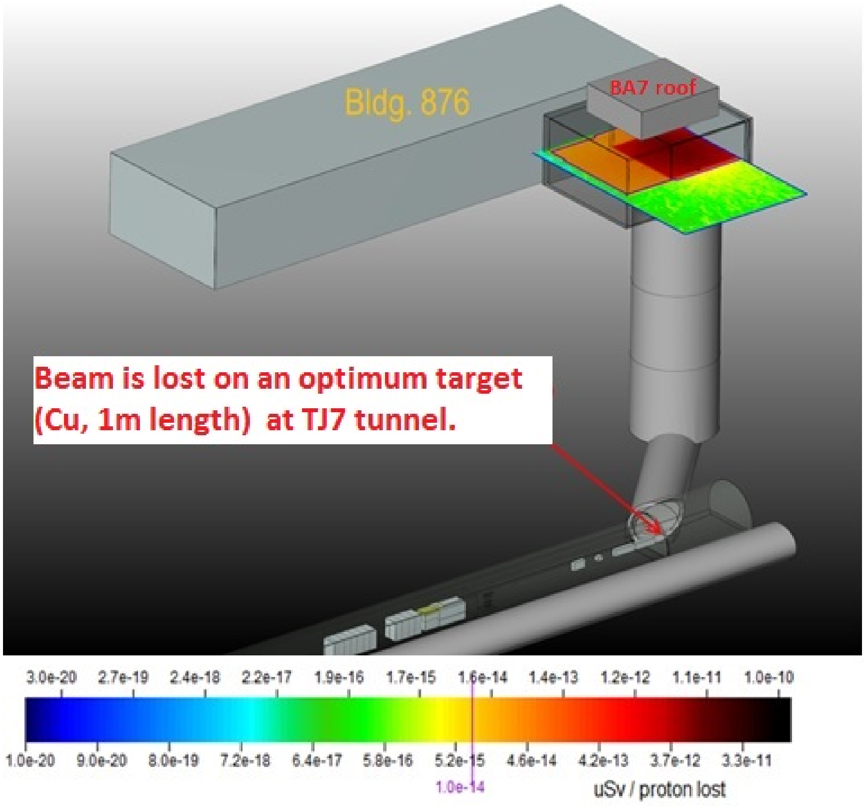

Figure 2.4: *Total dose equivalent per lost proton in the accessible areas around BA7 for the worst case accident scenario. It was found that in publicly accessible locations the highest expected dose equals* ~5×10^{-15} *μSv/lost proton* $\pm$ *25%.*

These dose rates can be considered as negligibly low impact for an accident with such a low probability. However, in addition to the theoretical assessment an ionization chamber is located next to the entrance of the shielded access shaft in BA7 (see [36] for details). In case that the radiation levels for low-occupancy non-designated areas are exceeded (> 2.5 $\mu Sv/h$) this monitor would raise an alarm in the control room and the RP service.

Underground Tunnels

The prompt dose rate in the underground tunnels was calculated with the same geometry, and for the operational envelope scenario of 4.89×10^{15} protons, corresponding to the maximum number of bunches (288) with the maximum bunch intensity (1.7×10^{11} protons), averaged over 100 extractions with duration of 20 seconds each. An example of the prompt equivalent dose rate (in $\mu Sv/h$) is shown in Figure 2.5.

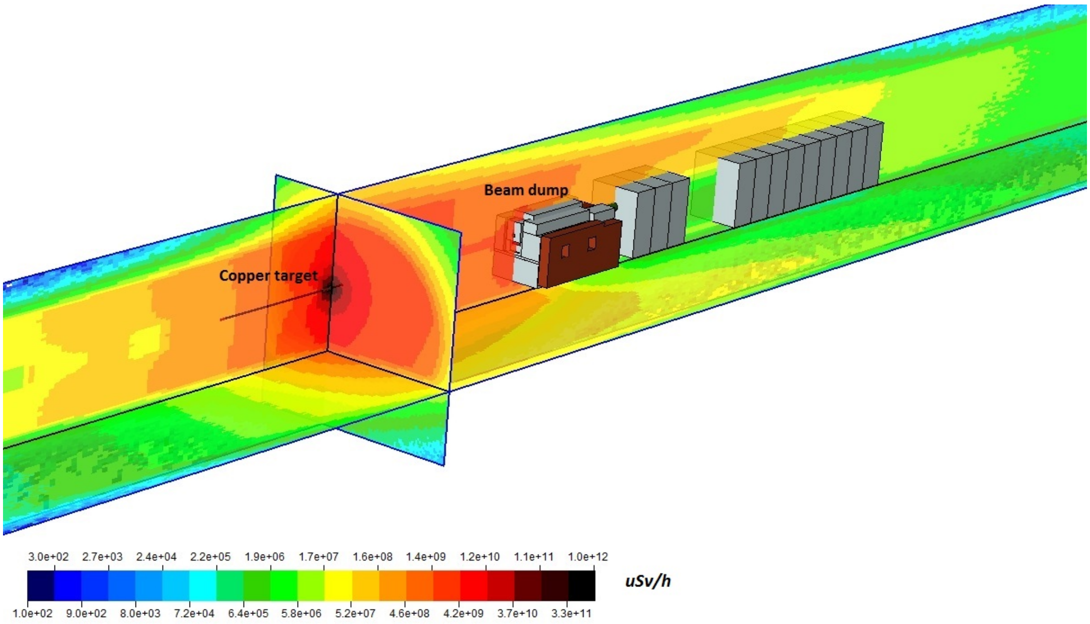

Figure 2.5: *Prompt dose equivalent in the TNC tunnel. The dose rates as expected are in the order of magnitude of 10ns of* Sv *at distances up to 1* m *upstream the target, while in contact with the irradiated object they are in the order of magnitude of thousands of* Sv*.*

Since the prompt dose rate during the operation is very high, all the underground areas of HiRadMat were classified as ”prohibited areas”, and access of personnel there during the operation is not allowed.

2.2.2 Activation Calculations

For the activation (residual) dose rate calculations, the model of a collimator [37] placed on an aluminum table at beam focal point 3 was studied after seven different cooling times (1 hour, 12 hours, 1 day, 2 days, 1 week, 1 month, 2 months). The irradiation profile chosen for this scenario was the short SPS cycle (10^{15} protons over 504 s), representing one experiment. Under this scenario, calculations for the underground areas of the facility (TNC, TJ7 and TA7) and the irradiated collimator were performed. For each of the experiments that later took place in the facility, similar studies were carried out. These studies were important in order to determine the cooling time intervals to access the facility and the handling of the radioactive objects. The full results of the activation studies of the facility can be found in reference [38], while specific activation studies for the experiments in [39, 40, 41]. The results show that the dose rate in the HiRadMat irradiation area decreases from few tens of mSv/h after a cooling time of 1 hour to about 1 mSv/h after one day of cooling time at a distance of more than 50 cm from the irradiated object, with respect to the beam axis. An example of the residual dose rate is shown in Figure 2.6. After one month of cooling time, the dose rate at a distance of 50 cm from the irradiated object has been reduced to 10 $\mu Sv/h$. However, the dose rate in contact with the collimator remains at about 1 mSv/h. Therefore, human intervention in the vicinity of these objects is foreseen to be kept at a bare minimum, with the implementation of a fully remote transport system which was installed in the facility, as already mentioned in section 1.3.3.

As far as the TJ7 tunnel is concerned, the average dose rate decreases from about 70 $\mu Sv/h$ (excluding current background radiation levels of a few tens of $\mu Sv/h$) after a cooling time of 1 hour to about 12 $\mu Sv/h$ after a cooling time of half-a-day. Therefore, in case that emergency access is necessary to the underground areas immediately after an experiment, it is possible after at least 12 hours of cooling time.

2.2.3 Background Calculations

Since in the first year of operation of the facility the number of experiments to take place in the facility was not fully defined, and the possibility of tight scheduling was significant, the background radiation remnant on the tunnel after an irradiation was calculated. Two sets of calculations were performed. In the first, the beam was simulated to hit on the jaw of the collimator used in the activation studies, which was afterwards removed from the irradiation area. The background dose on the tunnel was then calculated. In addition to that, as a worst-case scenario of an activated object, a cylindrical copper target, was placed at focal point 3. The irradiation profile used for both scenarios was 10^{16} protons over one year, representing the average total number of protons in the experimental area within one year's time.

From the moment that the irradiated object will have been remotely removed from the irradiation area, the beam dump remains the main source of radiation in the tunnel. Nonetheless, after 12 hours of cooling time, the dose rates (except in direct contact with the beam dump) remain in the level of 16 $\mu Sv/h$ at a distance of 30 cm from the dump, while they further decrease in the order of magnitude of few $\mu Sv/h$ after one week of cooling time. These latter do not further decrease, since the main source of radiation now in the tunnel are the long-lived isotopes produced in the beam dump. The results for TNC tunnel and four cooling times are illustrated in Figure 2.7.

The background radiation in TJ7 tunnel is reduced to a few $\mu Sv/h$ after 1 hour of

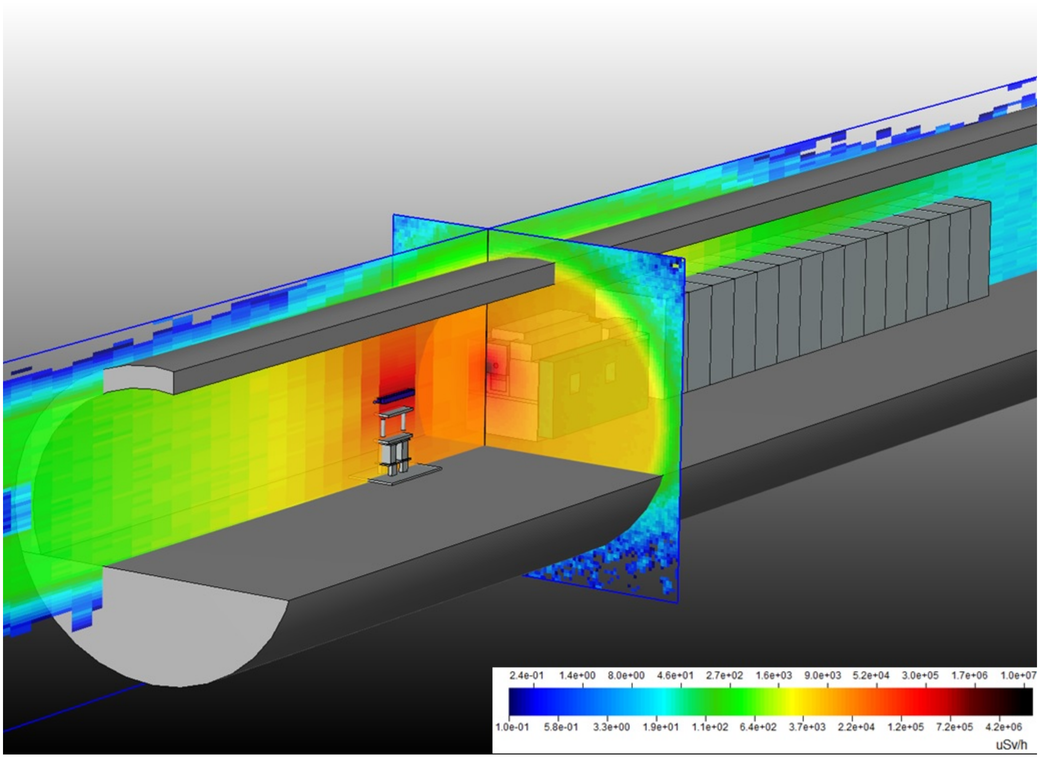

Figure 2.6: *Residual dose rate in the TNC tunnel after 1 hour of cooling time, at distances more than 50 cm from the activated object. The dose rate is about 10 mSv/h.*

cooling time while it becomes completely negligible after a cooling time of 1 week.

2.2.4 Cooling Water Activation Calculations

An estimate of the induced radioactivity in the cooling water pipes of the beam dump was carried out for two different irradiation scenarios in order to predict the possible activation of the water in these pipes. Compliance with the limits of the Swiss and French legislation had to be ensured in order to determine whether the water would have to be classified as radioactive. If that was the case, a special handling would need to be arranged. For this purpose, two different beam-impact scenarios were studied:

1. The beam was simulated to impinge on a graphite collimator located at focal point 3, which represents a *normal operational scenario*

2. The full beam was simulated to hit directly on the dump core, which represents a *worst-case scenario* since the water pipes are in direct contact with the core.

Moreover, two different irradiation profiles were used:

1. An average number of 10^{16} protons over one year, which represents a *nominal operational scenario* of the facility;

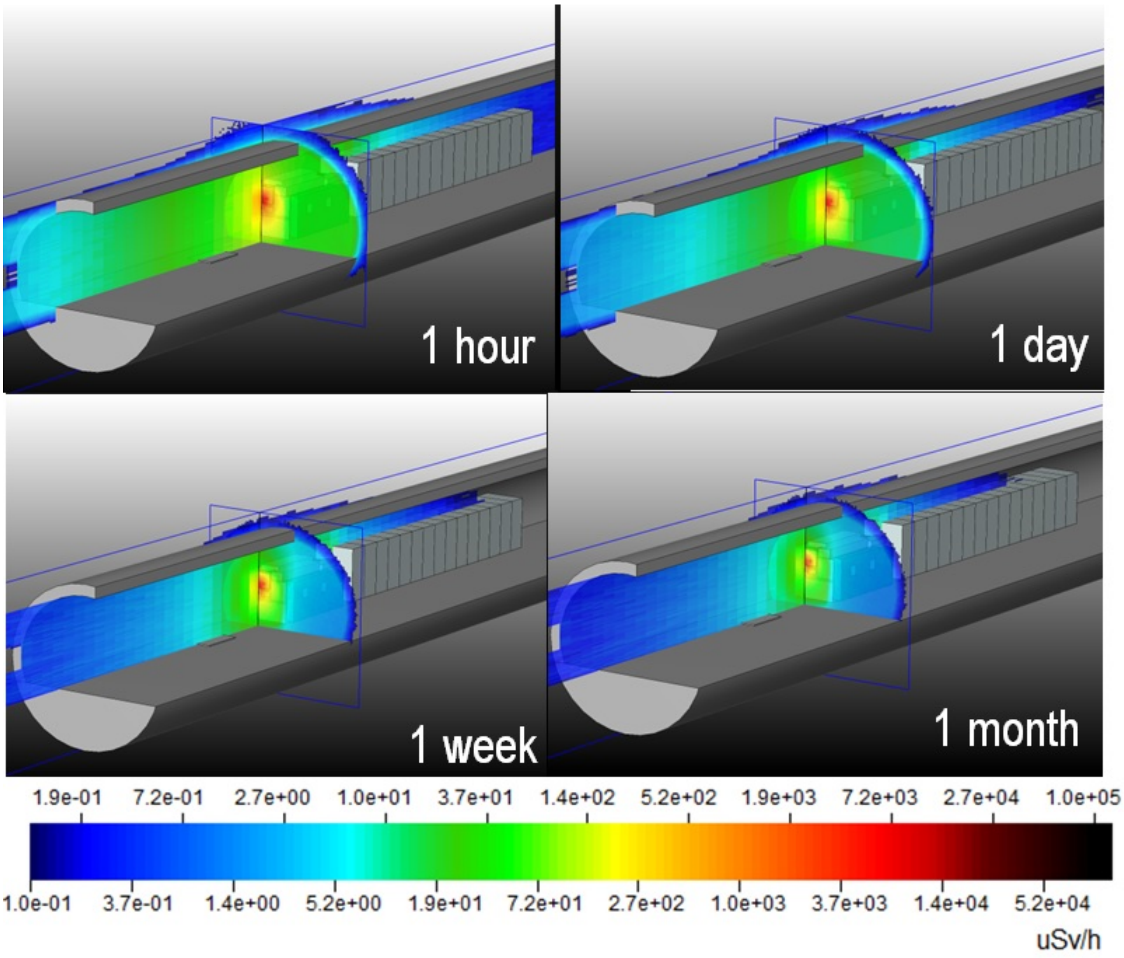

Figure 2.7: *The background radiation in TNC tunnel after the irradiated copper target has been removed. The main source of activation is the beam dump.*

2. An average number of 10^{17} protons over 10 years, which represents a *long-term scenario*.

Operational Scenario - Results

- For 10^{16} protons over one year, the specific activity in the cooling water of the dump was calculated to be $45 \;\; Bq/l$ from ^3H and 89 Bq/l from ^7Be.
- For 10^{17} protons over 10 years, the specific activity in the cooling water of the dump was calculated to be $353 \;\; Bq/l$ from ^3H and 89 Bq/l from ^7Be.

Worst Case Scenario - Results

- For 10^{16} protons over one year, the specific activity from ^3H in the cooling water of the dump was calculated to be 102 Bq/l and from ^7Be to be 198 Bq/l.
- For 10^{17} protons over 10 years, the specific activity from ^3H in the cooling water of the dump was calculated to be 1020 Bq/l and from ^7Be to be 1999 Bq/l

According to the relevant Swiss legislation [42], which is stricter than the French one, effluents are considered as radioactive if the following conditions are met: (1) the *specific activity* of certain radioisotopes (specific for each effluent) exceeds 1% of the **E**xemption **L**imit (LE) as a weekly mean and (2) the *total activity* of the effluent exceeds by 100 times the LE. In the case of water, the levels of tritium ^3H and ^7Be are considered critical. The value of 1% of the LE value for ^3H is 6000 Bq/l and 100 times the LE value for the total activity equals 60 MBq. In the case of ^7Be the respective values are 4000 Bq/l and 40 MBq.

According to the calculations, either in the operational or in the worst-case scenario these limits are not exceeded. Nevertheless, since the half-life of ^7Be is significantly lower than for ^3H, a worst-case short-term scenario was also studied: The beam of ten consecutive experiments, performed within the shortest possible time, would imping directly on the beam dump. This calculation of the maximum ^7Be levels showed a maximum of 946 Bq/l which is still below the limit of 4000 Bq/l. The results from all the studies are summarized in Table 2.2.

Based on the above, the risk of water activation in the beam dump core cooling circuits was found to be below the applicable limits, and therefore no special manipulation of the water has to be foreseen.

Isotope	$t_{1/2}$	**Bq/l-1 year**	**Bq/l-10 years**	**Legal Limit [Bq/l]**
Conservative Scenario - Beam directly on the dump				
^3H	12.4 years	102	1020	6000
^7Be	53.3 days	198	1999	4000
Operational Scenario - Beam on the collimator				
^3H	12.4 years	45	353	6000
^7Be	53.3 days	89	89	4000

Table 2.2: *The results of cooling water activation studies. The limits are not exceeded neither in the operational nor in the worst-case scenario, therefore no special handling of radioactive water has to be foreseen.*

2.3 Comparison with Measurements

CERN's radiation protection group operates a network of robust ionization chambers that are installed inside the accelerator tunnels, in order to perform remote reading of ambient dose rate equivalents of the underground structures. These monitors, with the trade name "PMI, PTW, Type 34031", consist of a non-confined air ionization plastic chamber which is operated under atmospheric pressure [43]. Five of these detectors are installed in HiRadMat's TNC tunnel, in the positions shown in Figure 2.8. As can be seen from the figure, PMI's 1-3 are located at decreasing distances from the dump, and therefore, when the beam impinges on the dump, the particle fluence in these detectors is inversely proportional to their distance from the dump. PMI-5 is located at a distance of only 30 cm from the dump, being therefore subject to the largest amount of radiation. PMI-4 is located in the opposite side of the tunnel, thus having a diagonal distance from the dump of about 5 m.

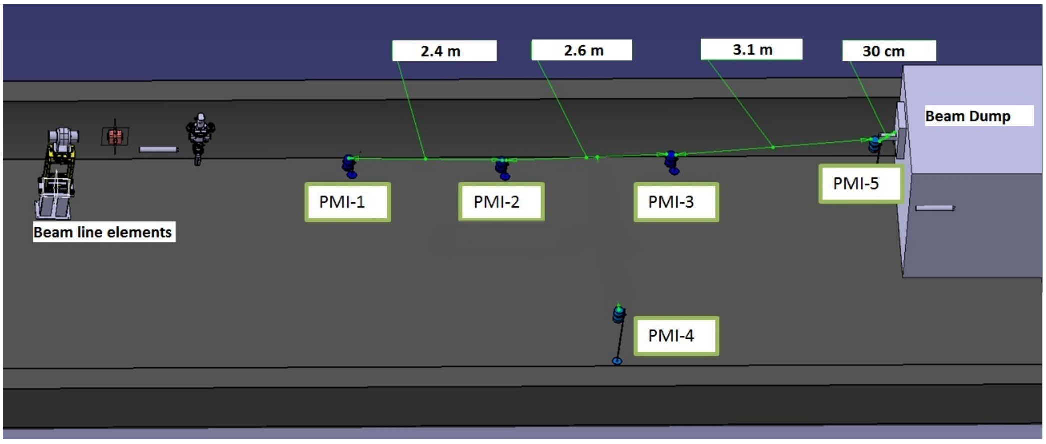

Figure 2.8: *The exact positions and distances of the PMI ionization chambers inside HiRadMat's experimental area. PMI-5 is located at a distance of* 30 cm *from the dump, where PMI-3, PMI-2 and PMI-1 are located at distances of approximately* 3.2, 5.8 *and* 8.2 m*, respectively.*

In order to evaluate the accuracy of the simulations for the facility, a detailed set of Monte - Carlo calculations was performed in order to compare the dose equivalent given by FLUKA, and the actual dose rate measurements of these detectors when the primary proton beam hits the beam dump.

2.3.1 Simulation Details

More specifically, the five detectors were modeled as rectangular air boxes, with their exact dimensions, at the exact positions as they are in reality. The calculation of the chambers' response was performed with the use of a special FORTRAN routine: The fluence of all particles reaching the detector area was scored, and the average energy deposition per beam particle was recorded. Using the W-Factor [44] (33.9 eV per e^-/ion pair), the energy deposition value was transformed into the number of e^-/ion pairs produced. Taking into account that 1 pC was required to trigger one detector count, the simulation result could directly be compared with its measured counterpart (converting Sv/h to pC based on the calibration of the detectors). In Figures 2.9 to 2.13 the calculated fluence of all the particles reaching each detector's volume can be found.

2.3.2 PMI Data

During the commissioning of the facility, several proton pulses were directed on the facility's dump, for the purpose of evaluating the beam line instrumentation. The commissioning took place on the 27th and 28th of June 2011. The pulse intensity was recorded with CERN's monitoring framework, TIMBER [45], which allows the retrospective retrieval of all the beam instrumentation data. The PMI data were retrieved by the CERN RAMSES system. For the purposes of the present comparison, only a fraction of the total number of the shots were used. More specifically, six shots were chosen with an

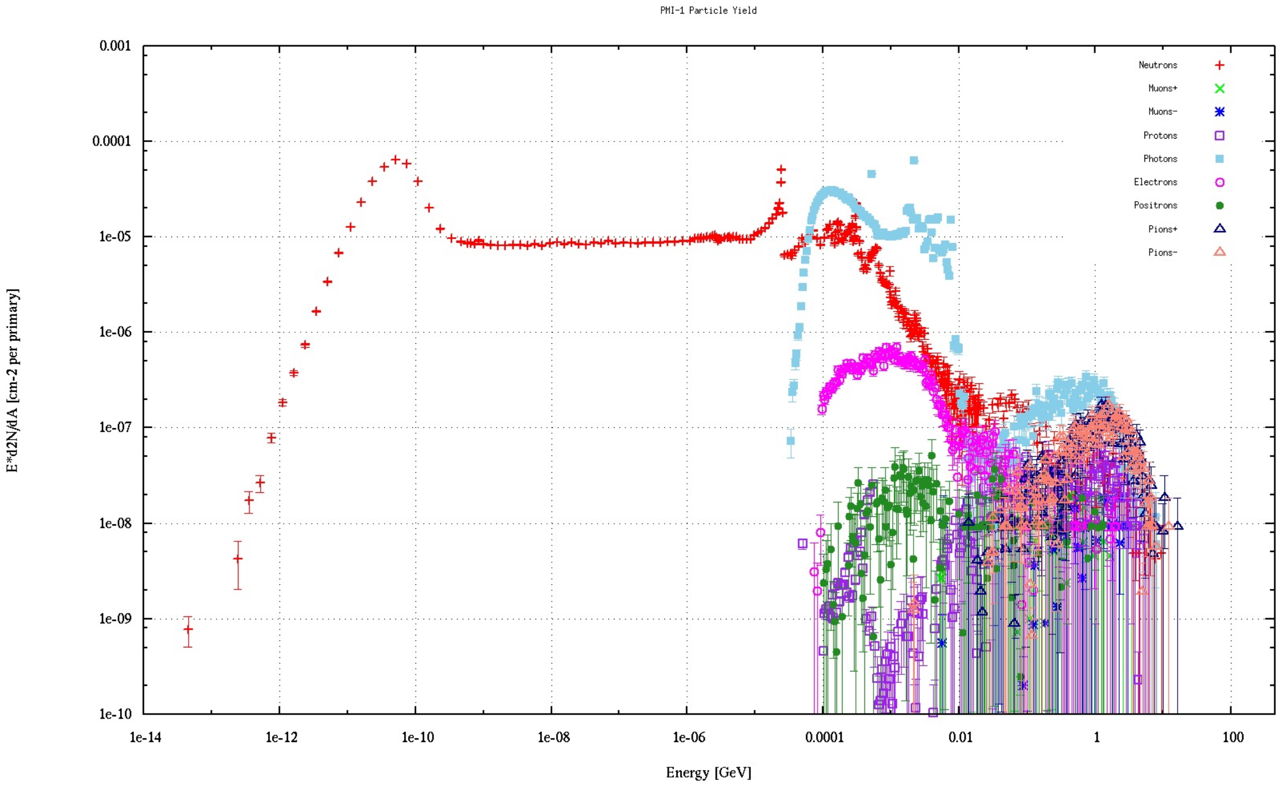

Figure 2.9: *The particle yield reaching the volume of PMI-1 detector (FLUKA simulation). The energy is given in GeV.*

increasing intensity and with similar horizontal and vertical position, as well as comparable beam losses. The data used in the analysis are summarized in Table 2.3.

Time Stamp	Intensity ($\times 10^9$ p.o.t)	PMI-1 (mSv/h)	PMI-2 (mSv/h)	PMI-3 (mSv/h)	PMI-4 (mSv/h)	PMI-5 (mSv/h)
28/11,15:59:12	2.52	3.29	5.08	7.27	3.84	24.9
28/11,17:39:02	4.75	3.42	5.29	7.54	4.02	25.7
28/11,21:12:06	6.92	4.73	7.08	10.1	5.43	33.1
27/11,17:10:10	7.34	4.97	7.32	10.4	5.56	34.3
27/11,14:57:34	8.36	5.16	7.70	10.9	5.86	35.7
28/1114:56:01	8.51	5.23	7.76	11.0	5.89	35.9

Table 2.3: *The dataset from the facility's commissioning used in the present analysis, and the recorded doses by the five PMI's. The time is UTC+1.*

2.3.3 Comparison Results

The background radiation from the already activated beam dump was not included in the simulations. Therefore, a constant underestimation of the simulated charges compared with the measured ones is expected, and illustrated for an intensity of 7.34×10^9 protons in Figure 2.14. In order therefore for the measured and simulated charges to be

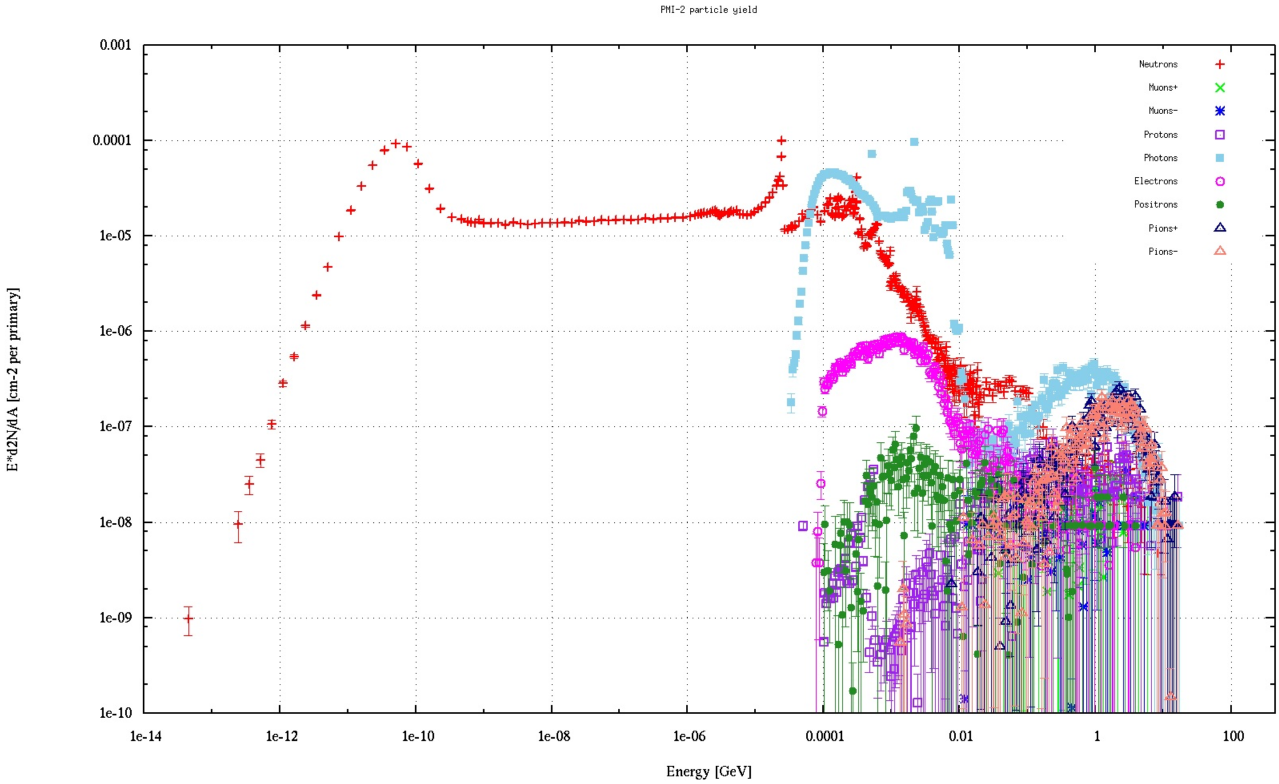

Figure 2.10: *The particle yield reaching the volume of PMI-2 detector (FLUKA simulation). The energy in the x-axis is given in GeV.*

directly comparable, the data of the farthest detector from the dump, PMI-1, were scaled to match the simulation results. The simulated results of all the other four detectors were scaled by same factor. The results of the comparison can be seen in Figures 2.15 to 2.20.

From the comparison figures it can be seen that the simulated and measured charges are in excellent agreement. More specifically, for PMI's 1-4, the difference between the measured and the simulated values lies within around 5%. Since the statistical uncertainty of the simulation fluctuates around 10%-15 % this result is very satisfactory. As far as the PMI-5 is concerned, the difference between the measured and the simulated charges is higher compared with the other detectors, lying between 20%-50%. This can be explained by the fact that PMI-5 is the detector closest to the interaction point. It is, therefore, subject to the residual radiation by the activated beam dump.

In conclusion, the agreement between the simulations and the measurements of the ambient dose equivalent are proved to be quite satisfactory. Additionally, the model of the facility is found to be trustworthy for future calculations.

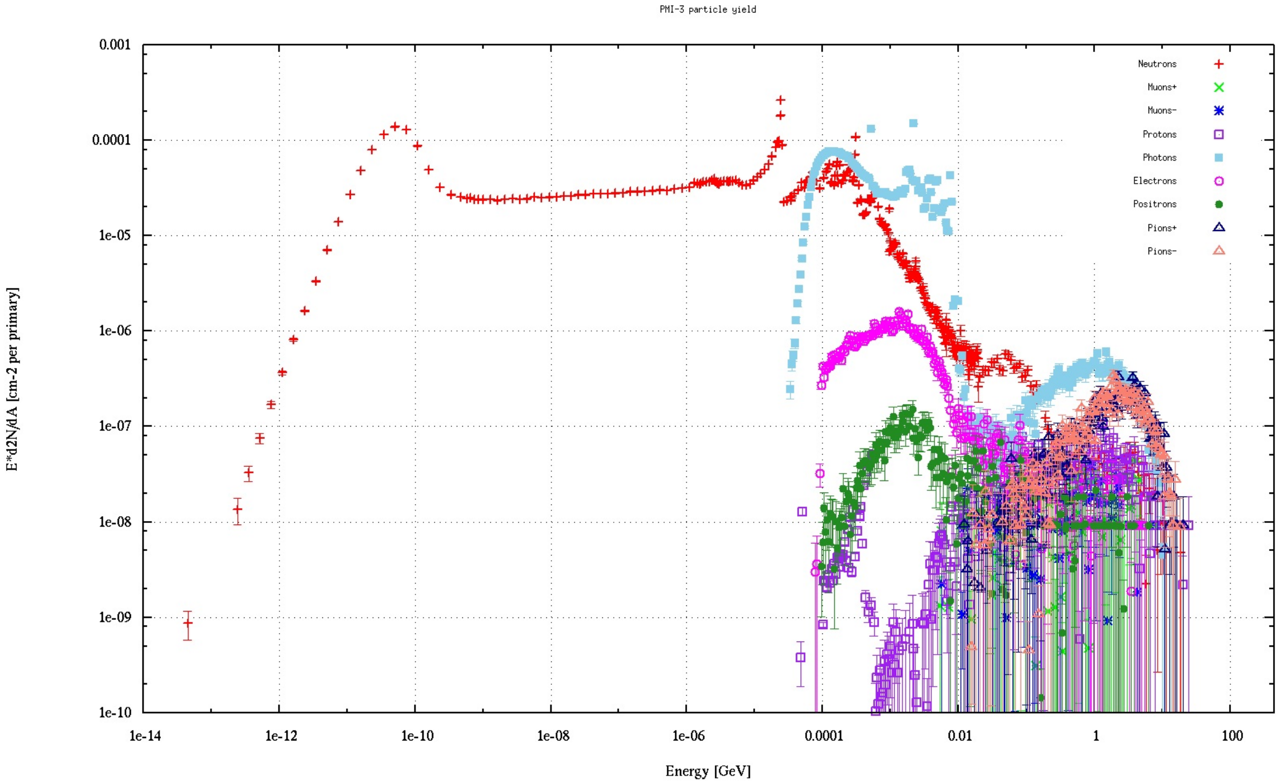

Figure 2.11: *The particle yield reaching the volume of PMI-3 detector (FLUKA simulation).The energy in the x-axis is given in GeV.*

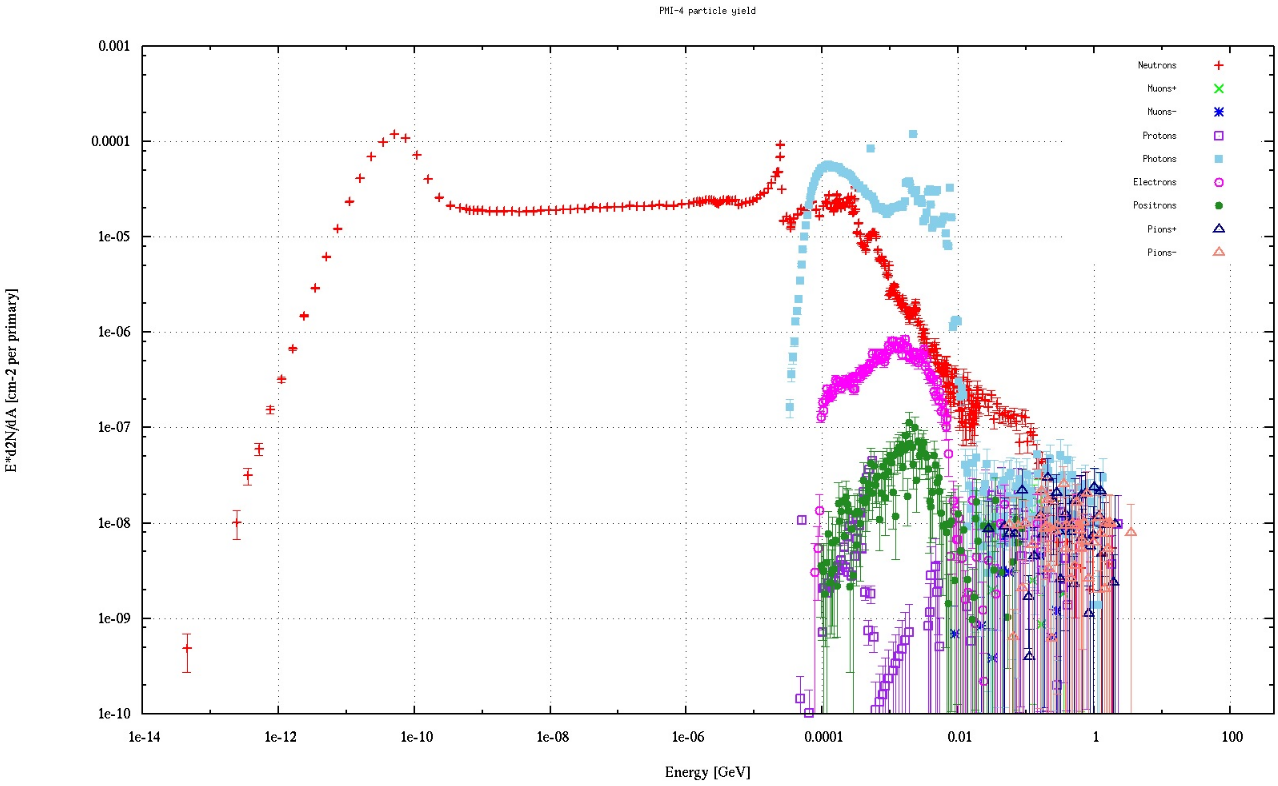

Figure 2.12: *The particle yield reaching the volume of PMI-4 detector (FLUKA simulation). The energy in the x-axis is given in GeV.*

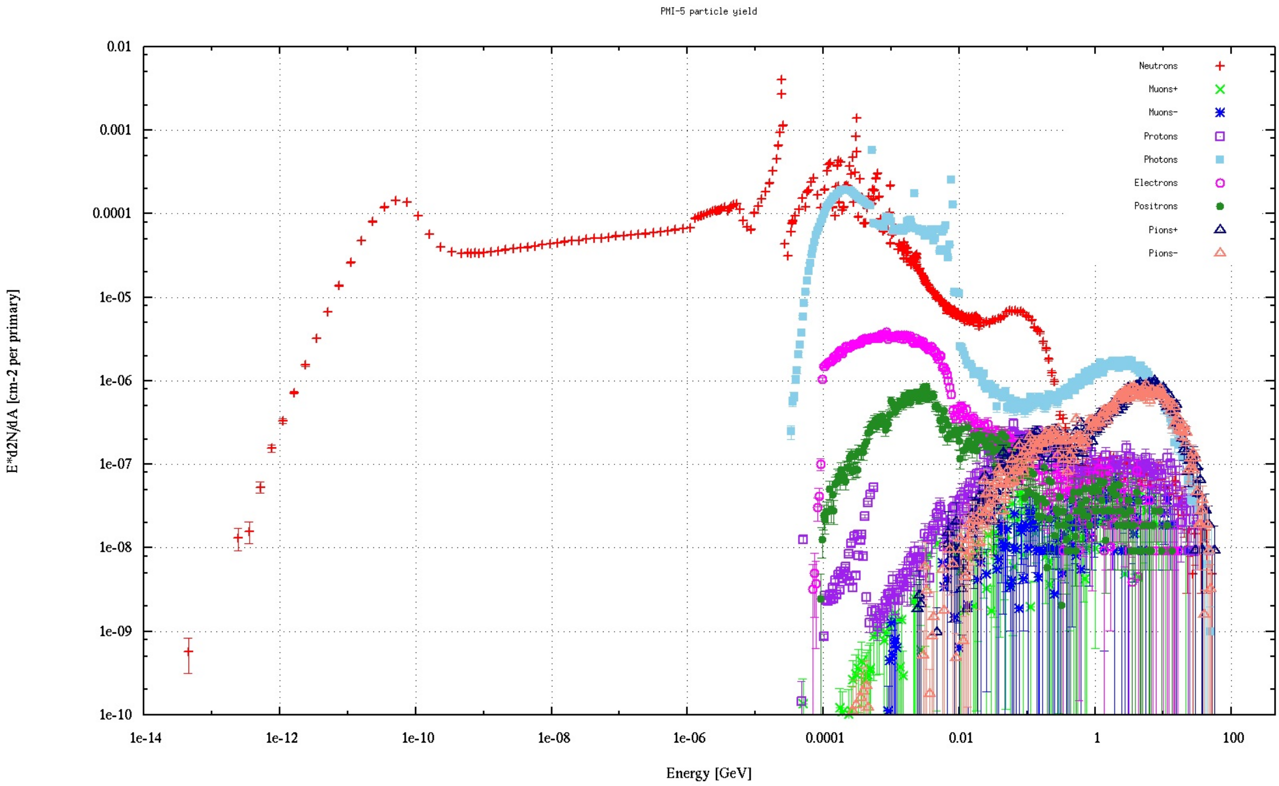

Figure 2.13: *The particle yield reaching the volume of PMI-5 detector (FLUKA simulation). The energy in the x-axis is given in GeV.*

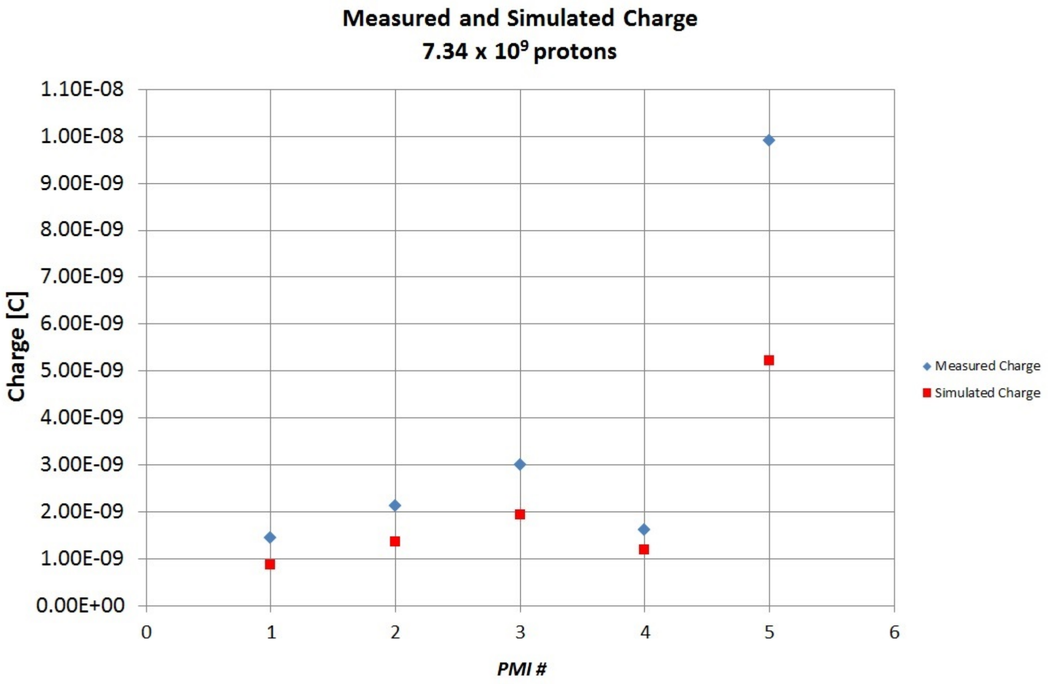

Figure 2.14: *A constant underestimation of the simulated charged compared with the measured one is expected due to the background radiation, as discussed in the text.*

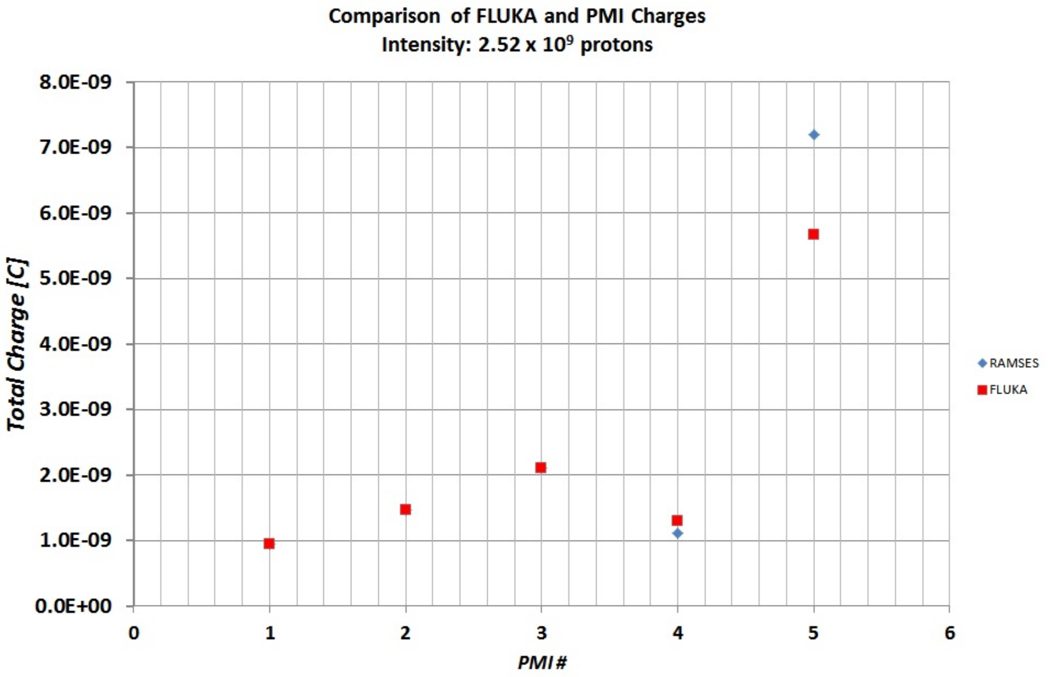

Figure 2.15: *Comparison between the simulated and measured charges for a pulse intensity of 2.52 $\times 10^9$ protons for the 5 installed PMI detectors.*

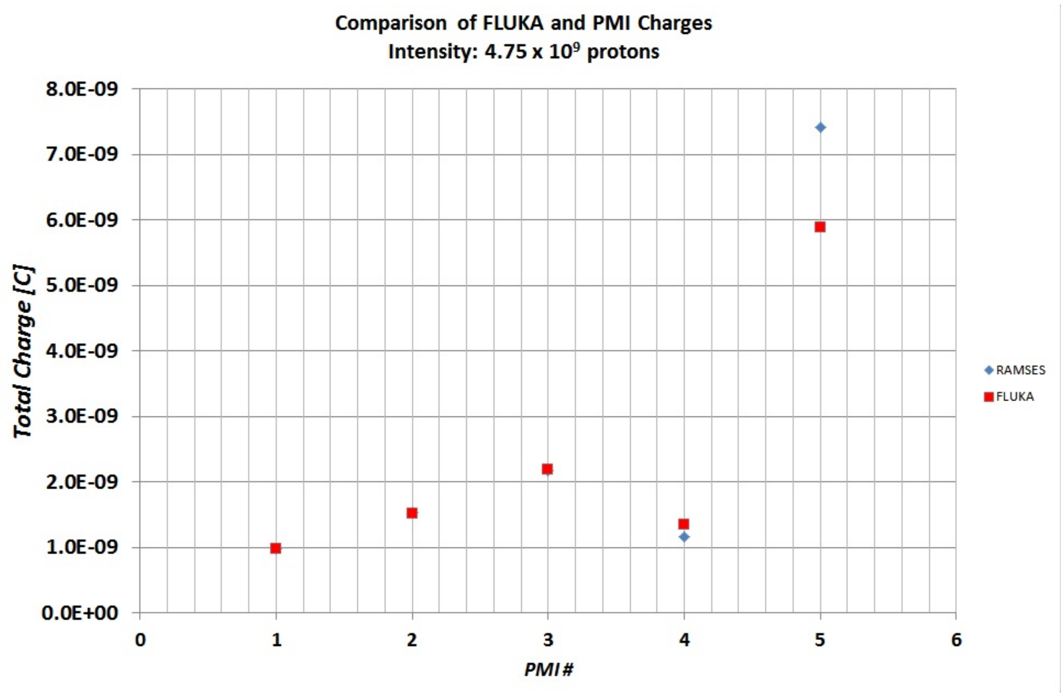

Figure 2.16: *Comparison between the simulated and measured charges for a pulse intensity of 4.75 $\times 10^9$ protons for the 5 installed PMI detectors.*

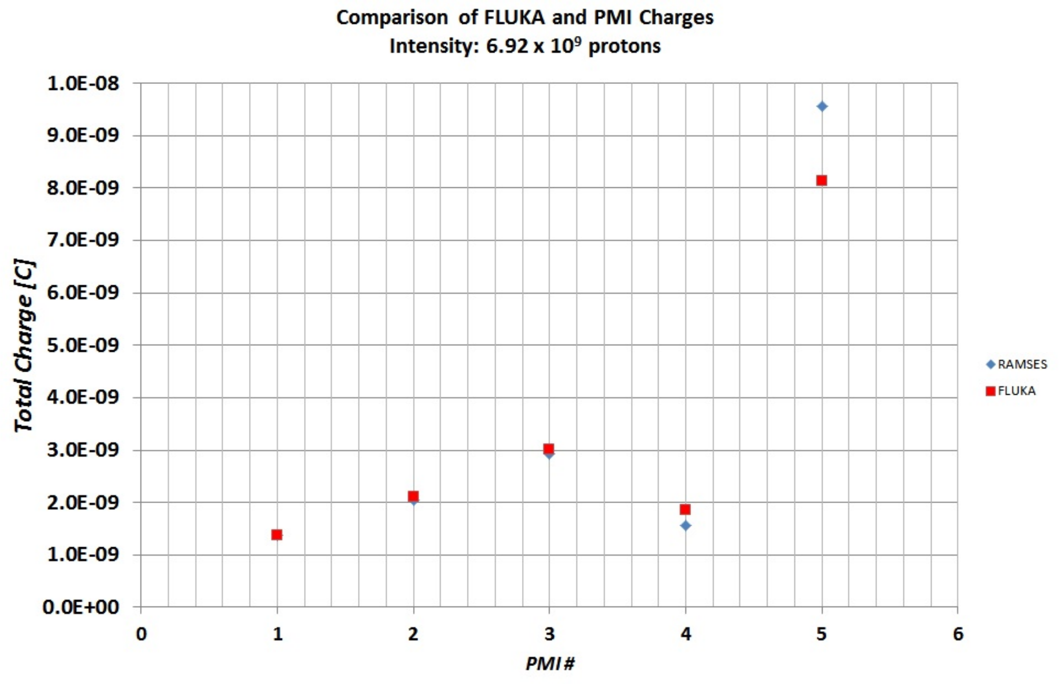

Figure 2.17: *Comparison between the simulated and measured charges for a pulse intensity of 6.92 $\times 10^9$ protons for the 5 installed PMI detectors.*

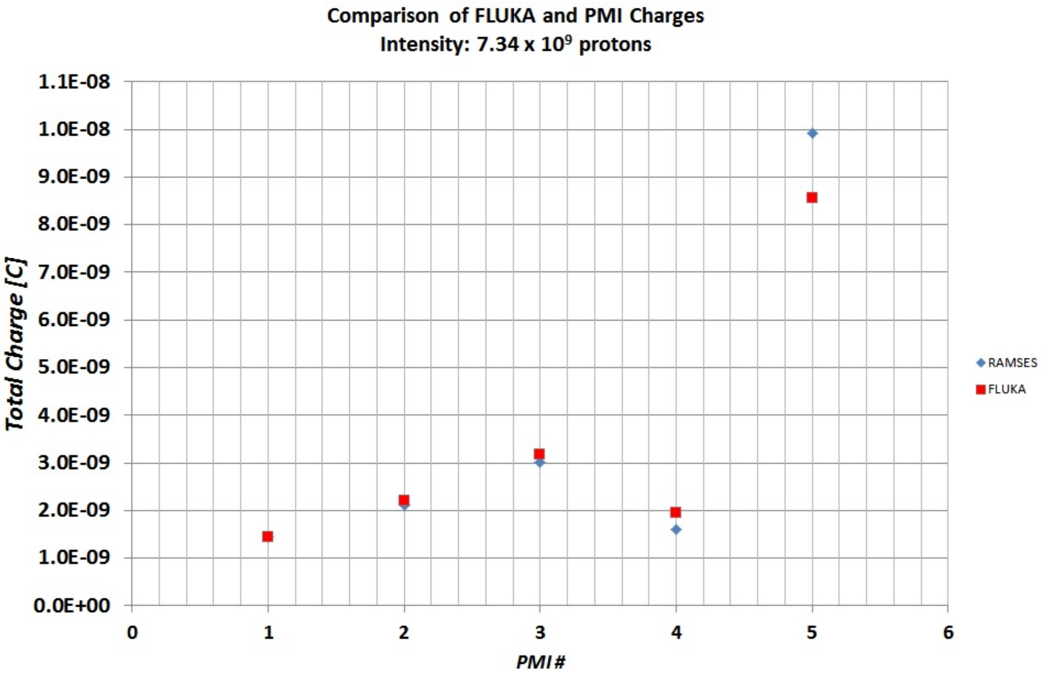

Figure 2.18: *Comparison between the simulated and measured charges for a pulse intensity of 7.34 $\times 10^9$ protons for the 5 installed PMI detectors.*

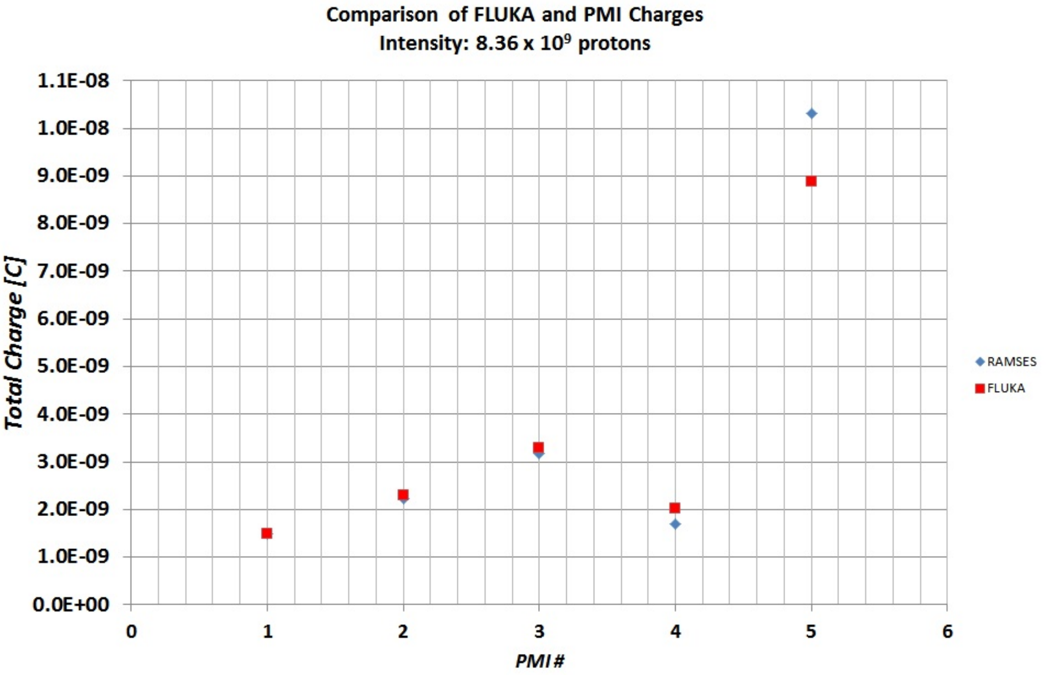

Figure 2.19: *Comparison between the simulated and measured charges for a pulse intensity of 8.36 $\times 10^9$ protons for the 5 installed PMI detectors.*

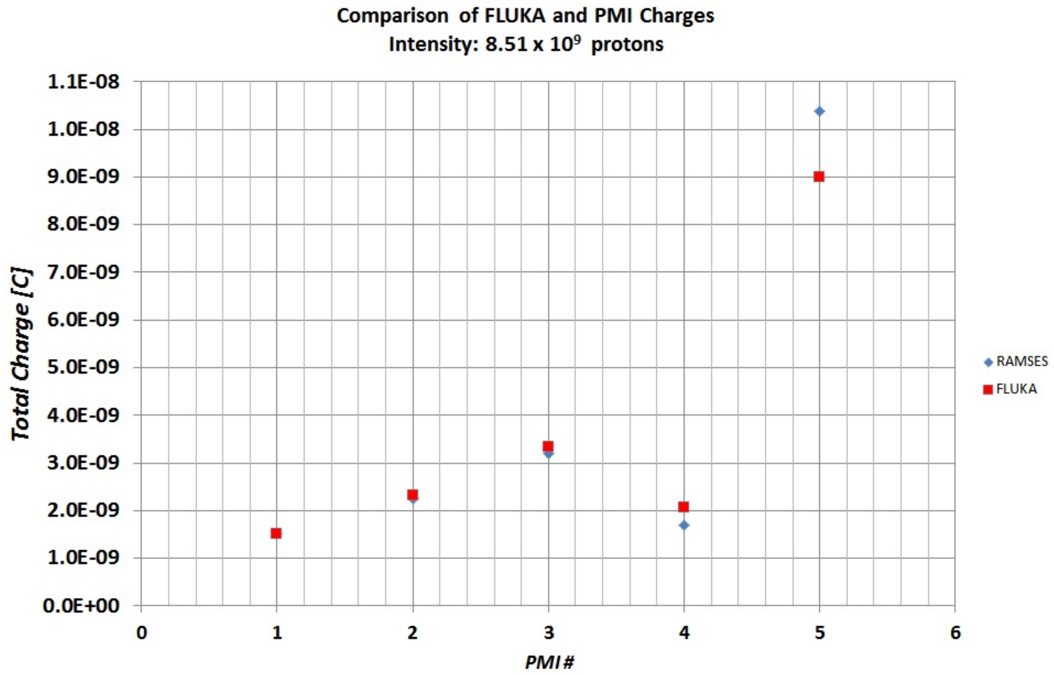

Figure 2.20: *Comparison between the simulated & measured charges for the intensity of 8.51* $\times 10^9$ *protons for the 5 installed PMI detectors.*

3 The HRMT-10 Experiment

3.1 Introduction

The requirement for future high-luminosity accelerator facilities like the $\mu^+\mu^-$ collider [46] or for a future neutrino factory, in which the secondary (rare) particles are created through interaction of primary protons with a target material, drives the need of addressing the “targetry” problem, i.e the correct design of the target system. Of particular importance among the target station parameters proposed for these future facilities is the requirement for a pulsed multi-MW proton beam. No existing target system would survive in the extreme conditions of such a powerful beam, since the target has to dissipate large amounts of energy, survive the strong pressure waves induced by the short beam pulses and also the long-term effects of radiation damage [47]. Extensive R&D is currently being performed on this area, and several solutions are under consideration. However, up to date, three generic target categories exist: Solid, liquid and granular. The advantages and disadvantages of each category are briefly hereby presented.

Solid targets in the form of rotating metal bands [48, 49], small carbon or zircaloy rods [50], or tantalum or depleted uranium plates [51] have been proposed or are today used in many accelerator facilities worldwide. The effects of a short pulsed, high power proton beam on solid materials have been thoroughly discussed (see for example [52, 53]). The most critical challenges for a solid target are (i) the radiation damage on the target material, (ii) the shock wave propagation caused by the instantaneous temperature increase which leads to transient stresses and (iii) the high heat flux cooling, which is imperative in order to prevent a target melting or even sublimation. The effort to overcome these has led to R&D studies of new materials as well as innovative methods of cooling. As the demand for higher beam power (in the multi-MW order of magnitude) appears, however, the limitations of solid materials as high performance targets become prominent.

In an attempt to overcome the limitations of solid targets, liquid mercury has been adopted as the target technology for the latest neutron facilities ”SNS” and ”J-SNS”, located at the ORNL and J-PARK research facilities respectively [54], while, following the results of the MERIT experiment, a liquid mercury jet moving inside a strong magnetic induction field constitutes nowadays the baseline for a future neutrino factory or a muon collider. The solution of a liquid mercury target presents considerable advantages compared to the solid targets. Some of these advantages are:

- the liquid state of the target allows for rapid exchange of the whole target for each proton pulse, thus evading the density changes due to the evaporation caused by the high energy deposition;
- the relatively easy circulation of a liquid mercury target allows for quick dissipation of the beam-induced heat;
- Hg is a relatively high-Z material, which offers a satisfying secondary particle yield;

However, the solution of mercury presents considerable technical challenges, such as cavitation due to the evaporation of the target which can be compromising for the target container and its toxic nature (both in its liquid phase and gas vapors) which can be dangerous for personnel. Until today, the implementation of a high velocity mercury jet as a high power target remains questionable.

3.1.1 Solid Fragmented Targets - The HRMT-10 Experiment

An alternative approach to the high power targetry problem are fragmented or granular solid targets. Several proposals for granular targets have been published (see for example [55]). However, the recent proof of fluidised tungsten powder pneumatic conveyance [56] merits the idea of evaluating the possibility of replacing the mercury jet with a tungsten powder jet. The advantages of a granular target include:

- The intrinsic resilience of individual grains to beam induced shock wave damage;
- It can be theorized that, beam - induced stress waves are contained within each separate grain of the material, and therefore the splashing of the target material (as observed in mercury) due to a shock-wave propagation can be avoided.
- No cavitation can occur in a powdered solid material within a carrier gas, since this is a phenomenon associated with liquids and solids only.

The choice of tungsten as a target material is based on its unique natural properties. In particular the high atomic number ($Z = 74$) and the density of 9 g/cm^3 when in powder form, offer a satisfactory [57, 58] muon yield. The high melting point (3695 K) allows robustness in terms of cooling. Therefore, like the mercury based target, a fluidized powder target would allow recirculation of a batch of target material so that the cooling can be performed off-line.

Despite its potential usefulness, the behavior of tungsten powder under an intense proton beam has not been tested yet. The lack of experimental data on high-power beam induced effects on a static, granular target drove the decision to perform a systematic evaluation of such a target.

The experiment, named ”HRMT-10” took place on 31/5/2012 at the HiRadMat facility of CERN/SPS. Since HRMT-10 was the first study of the interaction of a high-energy proton beam with tungsten powder, the underlying physics of such an interaction were investigated. The main scientific goal was to observe and understand the following effects :

- Possible disruption of the powder under the effect of the beam;
- Possible melting or agglomeration of the powder grains;
- A possible evaluation of the shock wave caused by the rapid temperature increase.

For the above reasons, and in order to directly evaluate the feasibility of such a target, it was decided to perform a single-pulse experiment of static, non-compressed powder, since such a setup would allow a first evaluation of the proton induced effects, that can be extrapolated for a jet target. An illustration of the original idea of the experimental apparatus for HRMT-10 experiment appears in Figure 3.1.

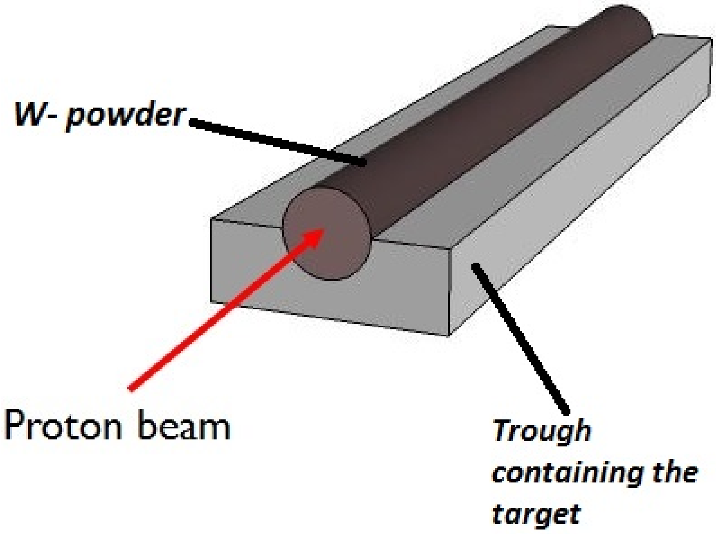

Figure 3.1: *An illustration of the HRMT-10 experimental apparatus conception idea. A static solid granular target would be intercepted by the HiRadMat proton beam.*

3.2 Experimental Design

3.2.1 Beam Parameters

A direct comparison between a mercury target and a tungsten powder target was intended. The beam parameters of a perspective neutrino factory (according to the **N**eutrino **F**actory **I**nternational **D**esign **S**tudy (NF-IDS) at the date of the experiment) and HiRadMat can be found in Table 3.1.

In order to define the exact beam parameters and the total number of protons that would be needed to obtain the same deposited energy with the HiRadMat beam impinging on a tungsten powder target, as the proposed neutrino factory beam impinging on

Parameter	Neutrino Factory	HiRadMat
Beam energy	8 GeV	440 GeV
Beam spot size	around 1 mm^2	variable from 0.01 - 4 mm^2
Protons per pulse	6.25 $\times 10^{13}$	1-288 bunches / max. 1.7E11 p/bunch
Target Material	Hg ($\rho = 13.53\ g/cm^3$)	W-powder ($\rho = 9\ g/cm^3$)

Table 3.1: *Comparison between the proposed neutrino factory beam parameters and HiRadMat beam parameters*

a mercury target, Monte - Carlo simulations were performed, a summary of which is hereby presented.

3.2.2 Energy Deposition Studies

The simulations were performed with the FLUKA code. The target was simulated as a cylinder with a diameter of 16 mm and a length of 30 cm. Tungsten powder was simulated as a compound consisting of 56% tungsten and 46% air (by volume), and a total density of 9 g/cm^3. The beam spot was simulated to have a Gaussian profile with $\sigma = 2\ mm$ in both the horizontal and vertical plane, and a momentum of 440 GeV/c impinging on one face of the cylinder, 6 mm below the tungsten free surface. The maximum energy deposition, in a scoring mesh of $0.5 \times 0.5 \times 300\ mm^3$ around the beam impact point, normalized per primary proton, is shown in Figure 3.2. The maximum calculated energy deposition of $4.5\ GeV/cm^3$ per primary proton, occurs at ~10 cm from the target front. It was therefore decided that the sampler holder should be constructed in such a way, in order to allow for an observation of this exact area of the target.

As can be seen in Figure 3.3, with a beam momentum of 440 GeV/c and a beam spot size of 2 mm^2 in both planes, a total intensity of 3.74×10^{12} protons per pulse is necessary in order to obtain the same maximum deposited energy per gram on tungsten powder as on mercury with a neutrino factory pulse.

The maximum temperature increase on the target was also calculated. For a pulse of 3.74×10^{12} the maximum temperature increase in the center of the target is calculated to be around 2200 K. The temperature distribution over the length of the target is presented in Figure 3.4. Therefore, since the melting point of tungsten is 3695 K, no melting of the grains should be observed.

3.3 Experimental setup

Two observation techniques were applied in order to quantify the target reaction to the proton beam exposure:

- High Speed Photography

  High speed photography was chosen as the basic instrumentation of the experiment. It has been employed in past experiments like MERIT as a diagnostic tool for recording the interaction of materials & particle beams with success. For the HRMT-10 experiment, a black & white high speed camera by RedLake® (model

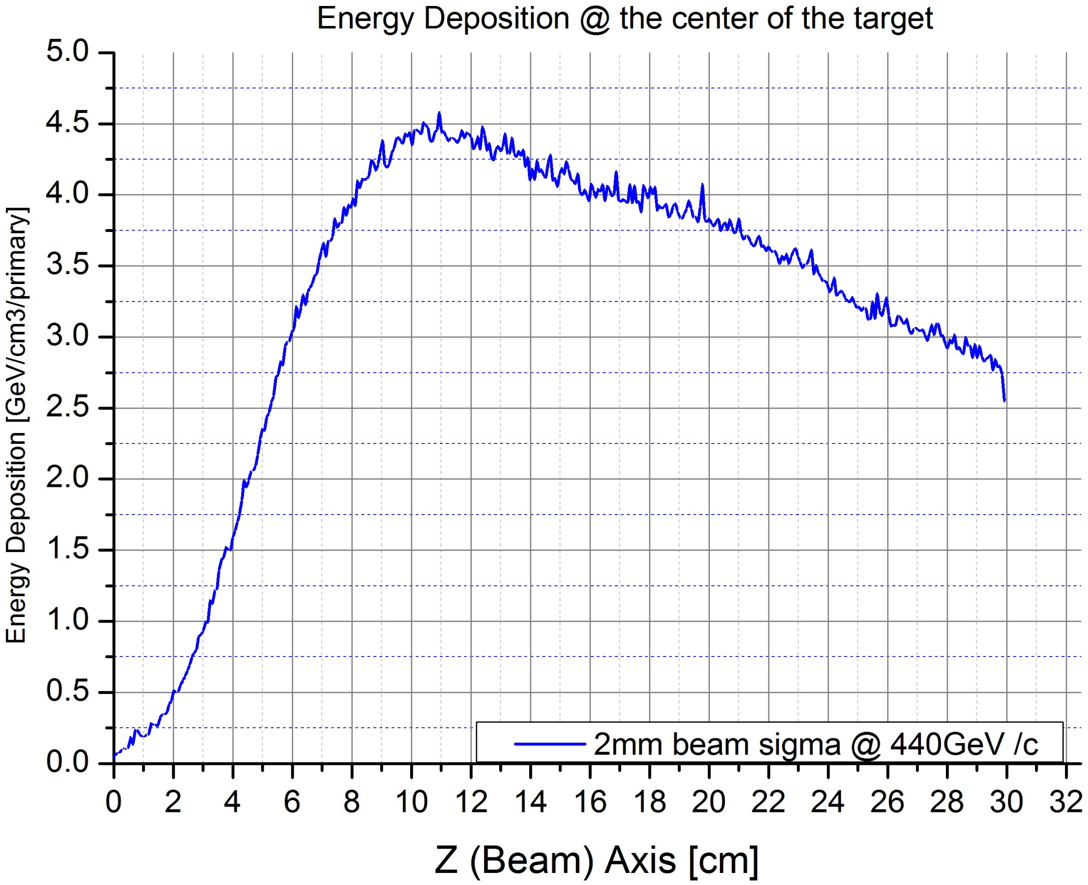

Figure 3.2: *The energy deposition in the center of the target,normalized per primary proton.*

MotionXtra HG-100k) with a capability of recording up to 10^5 **f**rames **p**er **s**econd (fps) was used. Technical details and a description of the camera can be found in [60].

- Laser - Doppler Vibrometry

  Laser - **D**oppler **V**ibrometers (LDV) are nowadays used in many industrial applications for the remote measurements of speed and displacement, as well as in previous targetry experiments [**?**]. For the HRTM-10 experiment, an LDV by Polytec® (model OFV-505), with maximum sampling frequency of 10.24 MHz was employed. Technical details for the vibrometer device (instrument & controller) can be found in [62, 63].

In addition, pressure gauges and temperature sensors were placed at several points in the interior of the experimental apparatus, in order to monitor possible temperature and pressure changes due to the beam impact.

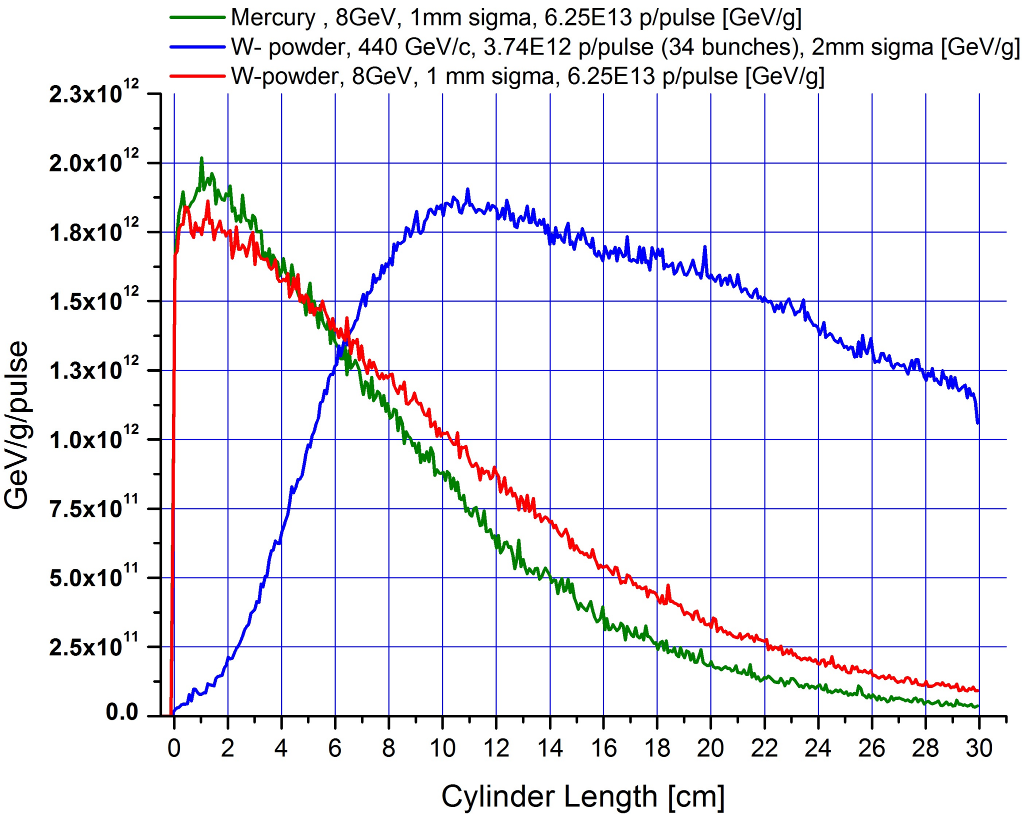

Figure 3.3: *Comparison of the energy deposition per gram on (i) the Hg proposed target after one pulse with the NF proposed beam parameters (ii) the tungsten powder target after one pulse with the HiRadMat beam parameters and (iii) the tungsten powder target after one pulse with the NF proposed beam parameters.*

The design of the experimental apparatus and the layout of the experiment in the facility were designed in such a way in order to fully exploit the capabilities of those instruments. More details for the specific parameters of the camera and the LDV used in HRMT-10 are given at later point.

3.3.1 Experimental Apparatus

In order to ensure the safe irradiation of the target, the experimental apparatus designed for HRMT-10 consisted mainly of a "sample holder", comprising of a U-shaped titanium trough with an inner width of 15 mm and a maximum height of 22.5 mm. The powder grain diameters distribution is illustrated in Figure 3.5, while a high-resolution microscope image of the grains is shown in Figure 3.6. Approximately 210 g of W-powder were placed inside the sample holder in total.

Primary & Secondary Trough

The beam would intercept the target along its axis, with its vertical position at 6 mm below the powder top surface. The interior trough containing the tungsten powder

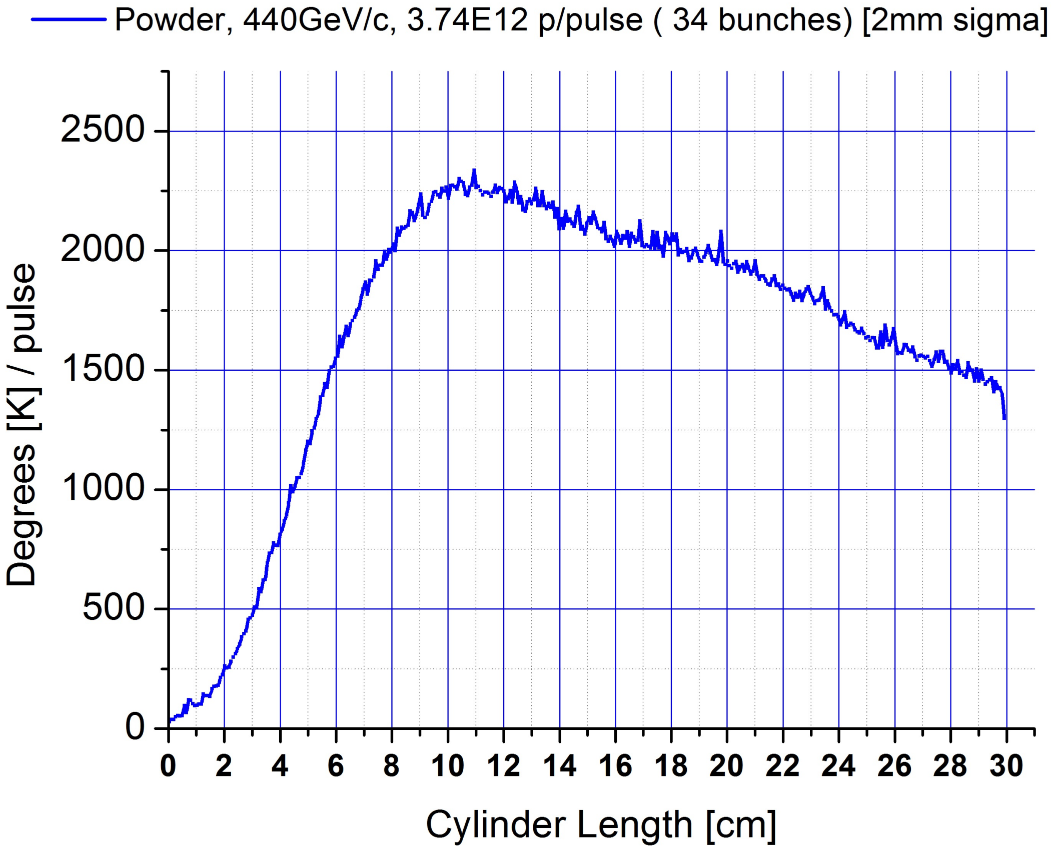

Figure 3.4: *Temperature increase on the center of the target, calculated for a pulse of* 3.74×10^{12} *protons. The maximum temperature increase is well below the tungsten melting point of 3695* K.

was surrounded by a second titanium trough, of similar construction with the primary one, but not directly in contact with the powder. A hole at a position of 8-10 cm from the beginning of the target allowed the LDV to measure the vibration of the inner container. An engineering drawing cross section of the setup can be found in Figure 3.7.

This double-trough geometry was chosen in order to measure the velocity both of the inner trough (containing the powder) and the outer trough in shots with similar intensity. From comparison between the two measurements, the source of the vibrations could be possibly determined and the magnitude of a possible shock wave propagating into the powder could be evaluated.

Containers

Since a possible disruption of radioactive powder was expected and in order to avoid possible contamination of the experimental area, two rectangular aluminum containers were constructed to surround the target. Two 3 mm thick soda-lime glass windows, were placed at the same position in both the inner and the outer container to allow a direct view onto the target. An engineering drawing depicting the setup is presented in

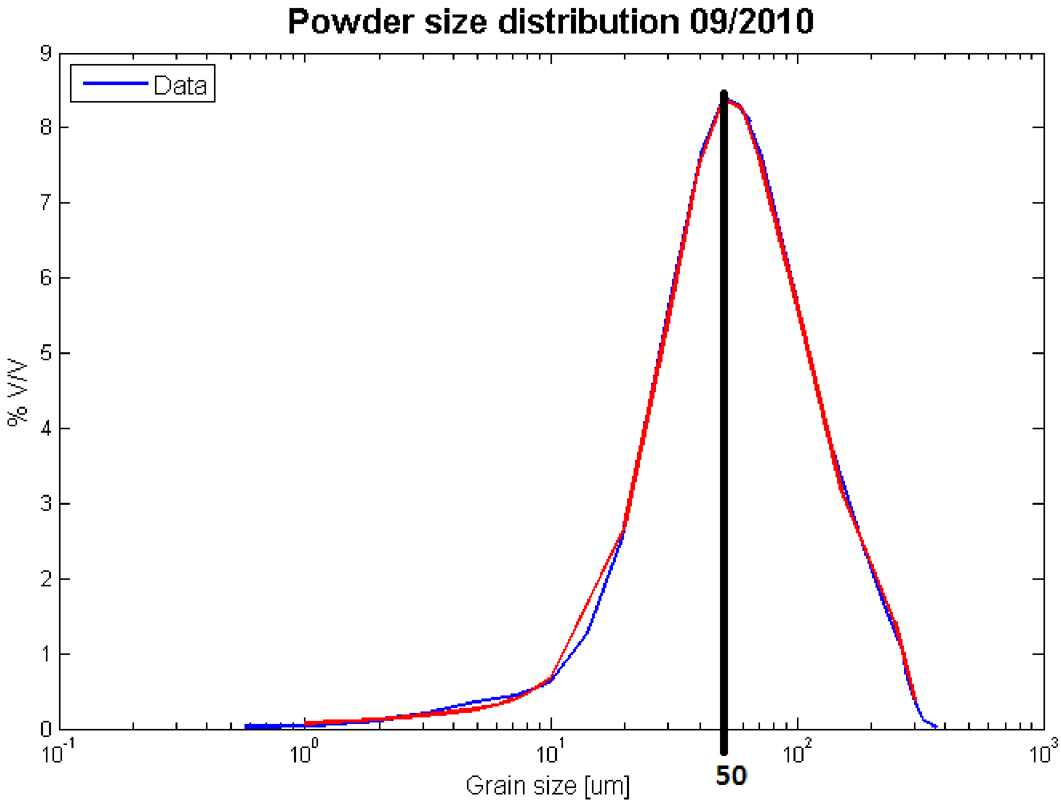

Figure 3.5: *The grain size distribution of the powder used in the experiment. Courtesy: RAL*

Figure 3.8, while a photo of the two containers appears in Figure 3.9. The beam entrance and exit windows were constructed from titanium, and both had a thickness of 1 mm.

To ensure that no combustion of the powder would occur due to the beam-induced temperature increase, the two containers were filled with helium gas at a nominal pressure of 1 bar.

Target Illumination

Many factors potentially contribute to the quality of a photographic image, such as the technology and resolution of the camera CCD sensor, the optical focusing lenses, the stability of the camera, the ambient lighting and many others; in the case of remote high-speed photography however, the determining factors for the quality of the images are (a) the small exposure interval, since recording in the kHz frame rate entails exposure intervals in the order of magnitude of ms, and (b) the very long observation distance which contributes to the optical power loss due to attenuation. These two factors impose the need of a strong illumination of the target.

For the HRMT-10 experiment, the illumination of the target was carried out by 12 powerful LED clusters (model: Oslon 10 Cluster White), placed onto six copper bases, for cooling purposes. The orientation of the LED stations can be seen in Figure 3.10. The

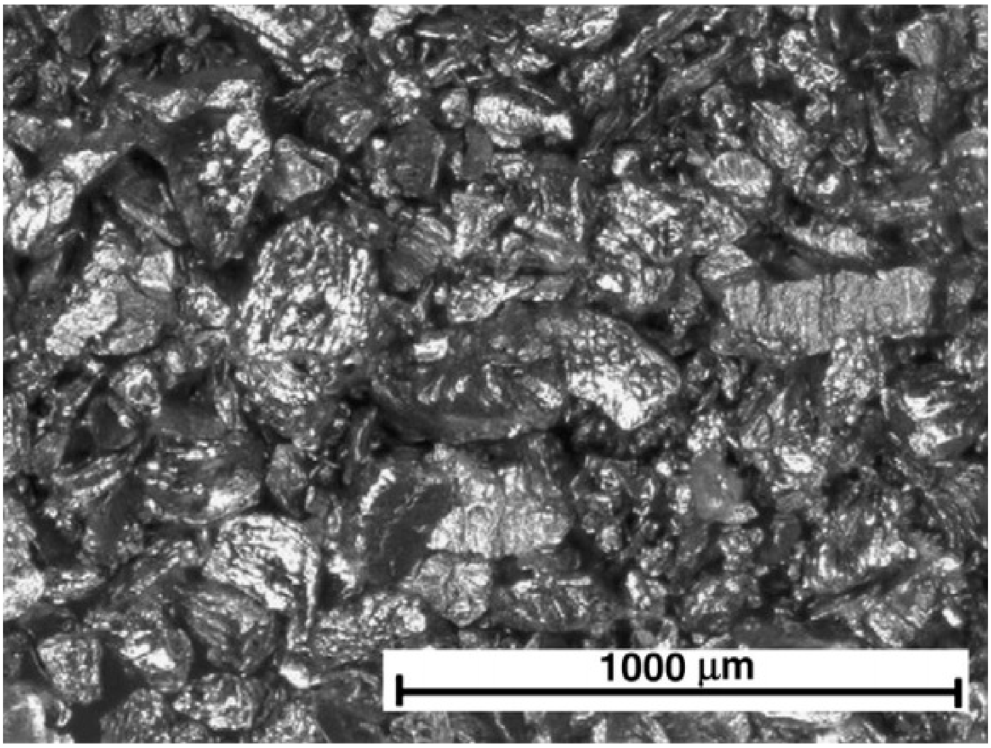

Figure 3.6: *A microscopy image of the tungsten powder grains used in the experiment. Courtesy: RAL*

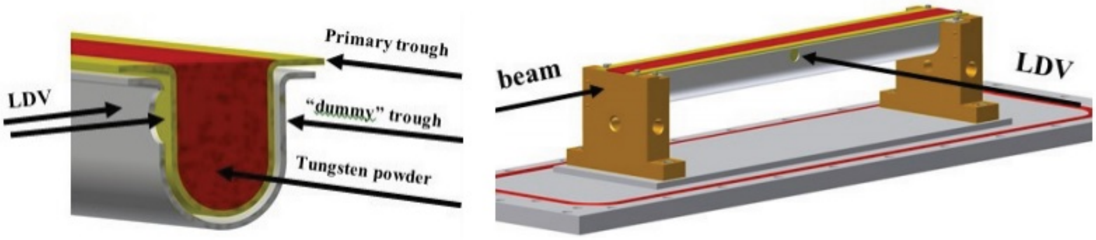

Figure 3.7: *Detailed cut view of the primary and the secondary trough. The two LDV positions (to the inner and the outer trough) are marked on the left image, while on the right image the complete setup is presented, as well as the measurement position of the LDV.*

total luminous flux of the LED's was 192 klm when their temperature was at about 40 degrees, while it was reduced to 178 klm when their temperature reached 70 degrees. Therefore it was decided to turn off the LED's between the beam pulses on target, in order to maintain their temperature as low as possible.

The complete setup of the apparatus is shown in Figure 3.11, while a direct view of the target trough through the two observation windows can be seen in Figure 3.12. A total length of $14\ cm$ of the target was visible through the window. In order to be able to measure the height of a perspective disruption, a grid was manufactured and placed

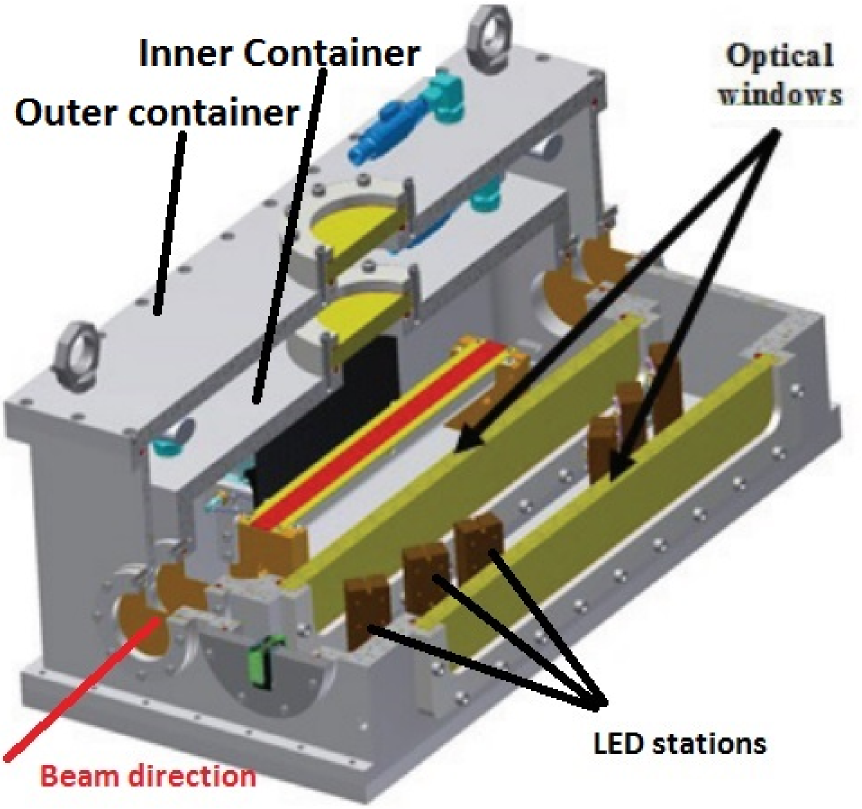

Figure 3.8: *A section-drawing of the complete setup. The two containers and the two observation windows can be seen. 6 powerful LED-cluster stations placed inside the first container were used for the illumination of the target.*

Figure 3.9: *Photograph of the inner and outer container.*

behind the target trough. The experimental apparatus was installed on HiRadMat's mobile table. More specifically, it was installed on a special platform (which was bolted on the table) that could vertically move it into and out of the beam's trajectory. The power and control cabling of this motor, along with the power switches of the LED's and the

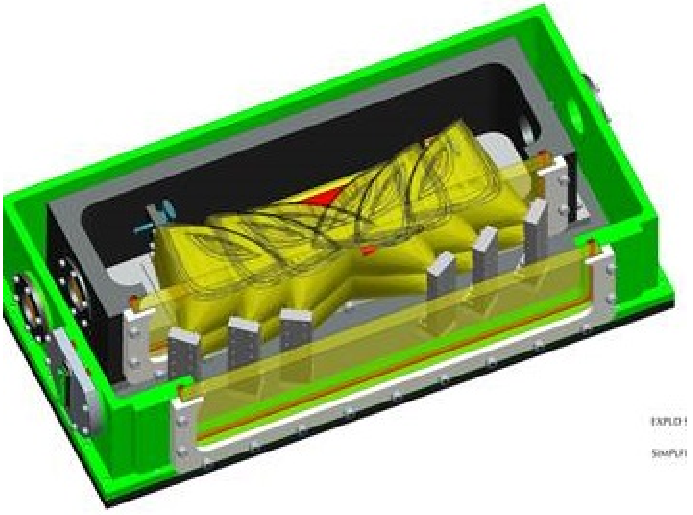

Figure 3.10: *Drawing of the LED stations and the illumination of the target.*

data cabling of the pressure and temperature sensors of the apparatus, were connected to the connectors of the mobile table. Through the facility's cabling infrastructure the signals were transmitted to the control room, from where the remote control of the LEDs and the data logging of the sensors was possible at any moment during the experiment.

Figure 3.11: *Photograph of the designed experimental apparatus. On the left side the cabling for the temperature and pressure gauges can be seen, connected to the data logger in the right side.*

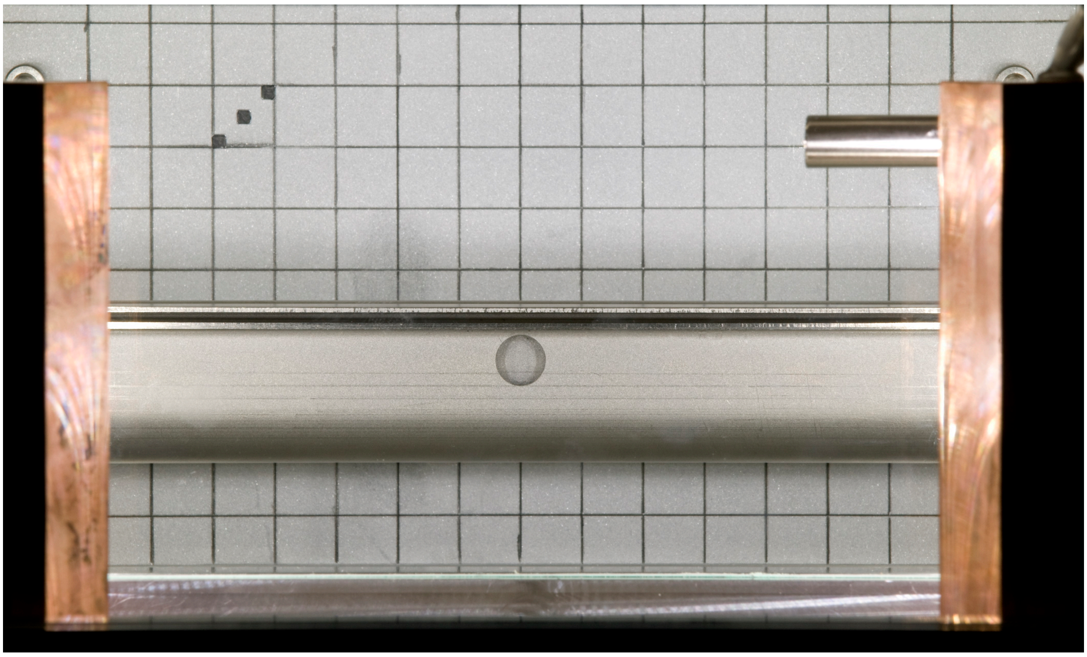

Figure 3.12: *Image of the target through the two observational windows. In left and right of the image, two of the copper bases of the LED stations can be seen. A grid was manufactured and placed behind the trough, in order to be able to easily measure the height of a possible disruption.*

3.3.2 Experimental Layout

Prompt Radiation and Concrete Bunker

Detailed Monte - Carlo simulations were carried out in order to assess the prompt and activation radiation expected from the target. A detailed model of the apparatus, very accurate in dimensions and materials was prepared and shown in Figure 3.13. In Figure 3.14 the prompt dose equivalent for one pulse of 3.74×10^{12} protons is depicted.

The prompt dose on the target is several thousands of Sievert, while just few centimeters away from the experimental apparatus, the dose is several hundreds of Sievert. This amount of prompt radiation precluded the placement of any electronic equipment near the mobile table. Both the high-speed camera and the LDV had to be placed at a safe distance from the target and be shielded from the prompt radiation. In order to deal with this situation, the following solution was implemented: the high-speed camera and the LDV were placed inside a custom-made concrete bunker, placed in the TJ7 tunnel about 35 meters away from the target. The optical guidance of the camera and the LDV beam on the target was performed through a system of two mirrors for each one of the devices. The first mirror was placed near the bunker in the TJ7 tunnel, and the other near the target (in the TNC tunnel). The second mirror was common for both instruments, and was attached on the mobile table. A schematic of the setup can be found in Figure 3.16 and a photo of the second mirror can be seen in Figure 3.17. The TJ7 mirror through which the LDV beam was directed onto the troughs was placed

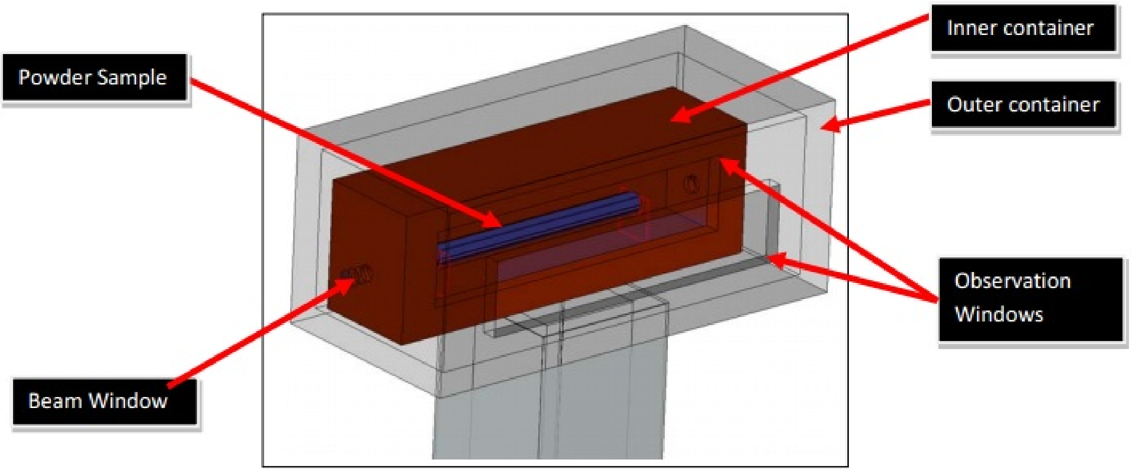

Figure 3.13: *FLUKA model of the experimental apparatus of HRMT-10. The sample holder, the secondary trough and the two containers with the two observation windows are accurately modeled.*

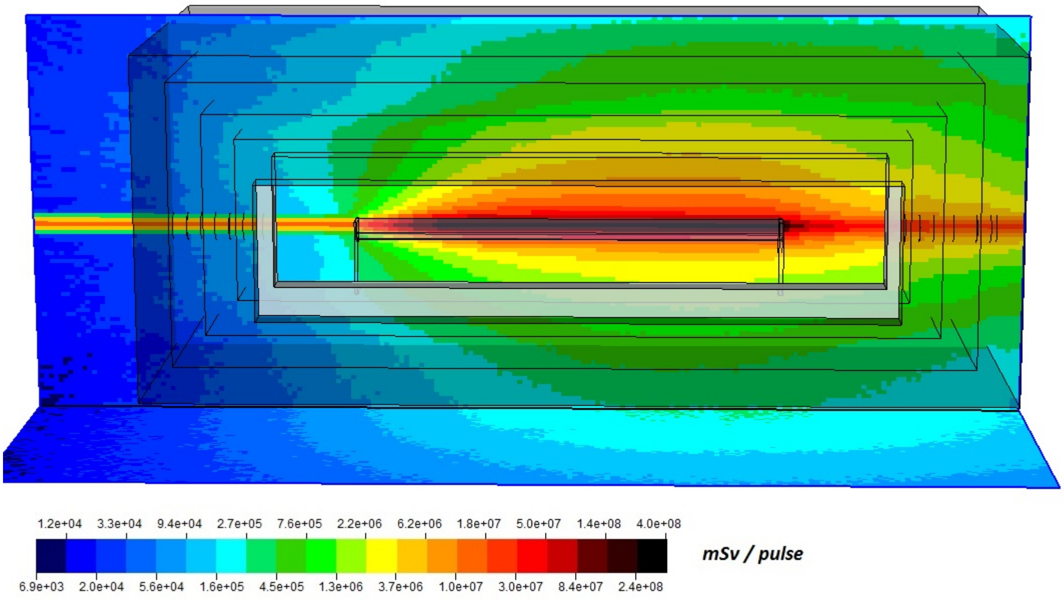

Figure 3.14: *Prompt Dose Equivalent of the apparatus for* 3.74×10^{12} *protons. The prompt dose of the target itself approaches thousands of Sievert for this number of protons.*

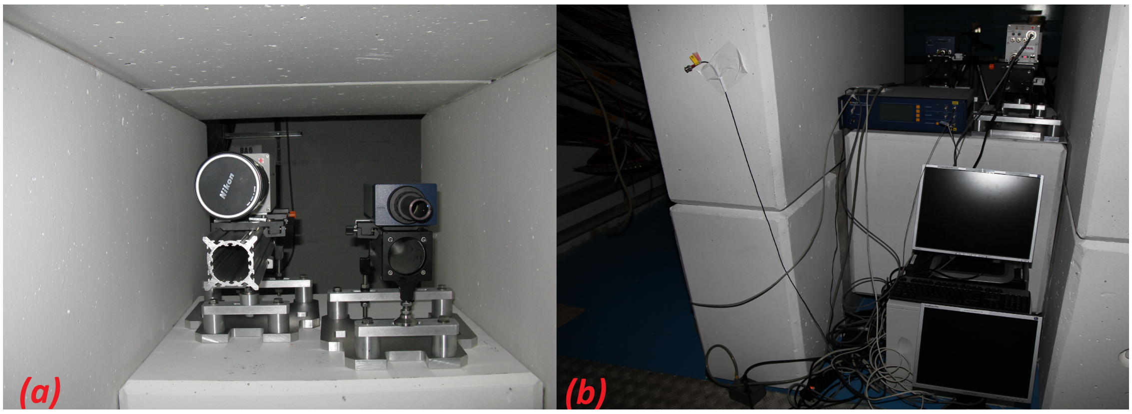

Figure 3.15: *Photos of the LDV and the High Speed Camera installed inside the concrete bunker. In (a) the front face of the camera and the LDV can be seen, while in (b) the two computers used for the data acquisition of the devices are shown.*

on an electronic, remotely controllable translation device. The horizontal translation of the mirror, allowed the remote translation of the LDV beam from the inner to the outer trough.

In Figure 3.15 photos of the High Speed Camera and the LDV installed in the TJ7 bunker can be found. In (a) the front face of the camera and the LDV inside the concrete bunker, stabilized on the special aluminum bases can be seen while in (b) the back view of the diagnostic equipment is shown. Two computers connected on CERN's network allowed the remote control of the data taking procedure.

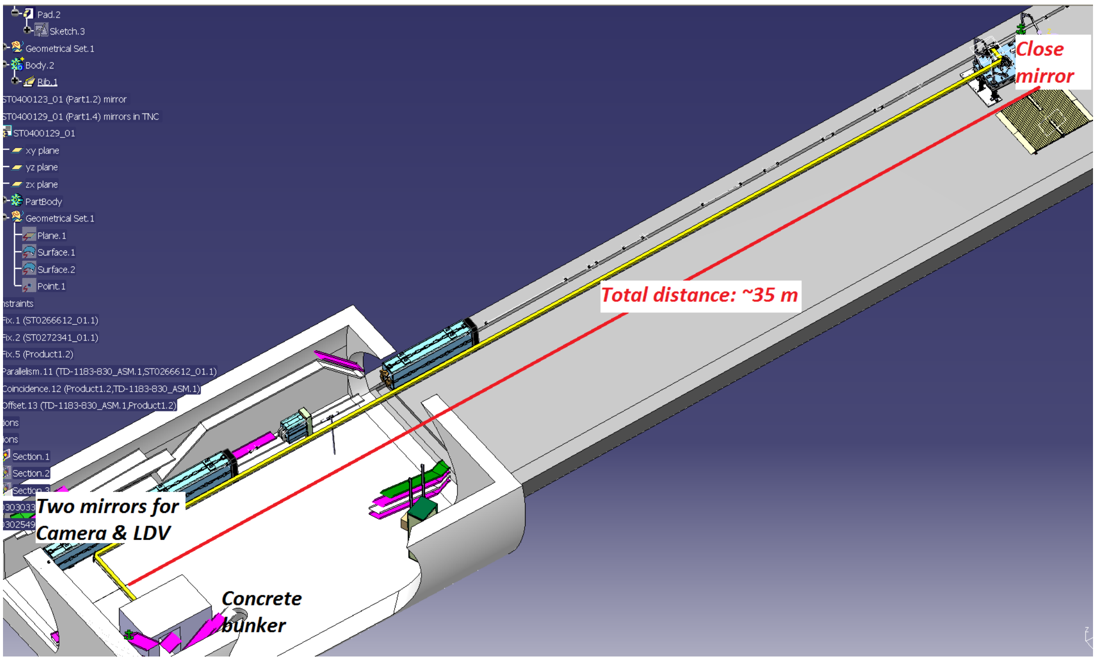

Figure 3.16: *The experimental layout of the HRMT-10 experiment.*

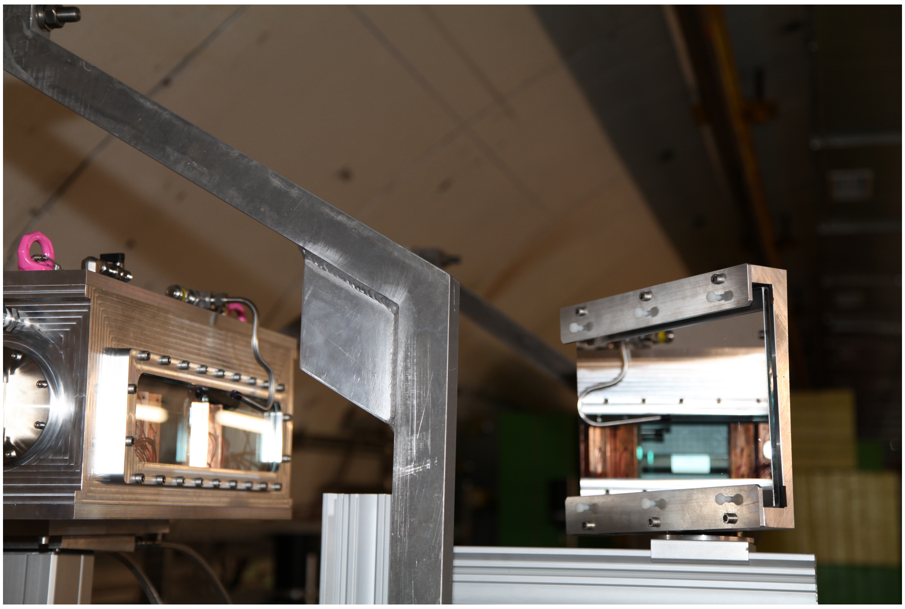

Figure 3.17: *The fixed mirror attached on the mobile table, close to the target. Both the camera view & the LDV beam were guided through the same mirror on the target.*

The thickness and the exact dimensions of the concrete bunker were optimised with different sets of Monte - Carlo simulations. The model of the final bunker design can be seen in Figure 3.18 and the calculation of the dose that the equipment would be subject to for a proton pulse of 3.74×10^{12} protons in Figure 3.19.

3.3.3 Instrumentation Parameters

The high-speed camera was placed inside the concrete bunker, and was connected through an ethernet controller to a PC, while the LDV and the electronic translator of the LDV mirror were connected to another. Both computers were also placed inside the bunker and were connected in CERN's network infrastructure. That way, they could be remotely accessed and controlled from the surface. The camera was placed on an aluminum base, bolted on the concrete bunker, explicitly constructed for ensuring its stability. In order to focus the camera on the sample holder through two mirrors, a telephoto lens (model NIKORR-40) with a focal length of 2000 mm was mounted on the camera. In addition, two secondary lenses ("teleconverters") were also mounted on the camera, the first of strength 2x and the second of strength 1.4x. The effect of the teleconverters is to multiply the focal length of the camera lens. As a result, the total focal length of the high-speed camera was about 4800 mm. The frame rate was initially chosen to be 2000 fps (2 kHz) but during the experiment, it was realized that 1000 (1 kHz) fps were also sufficient to fully observe the powder movement. Therefore some of the shots are recorded with 2000 fps while the rest with 1000 fps. Due to the very small distance between the target center and the grid, the camera was simultaneously focused on the grid and on the target.

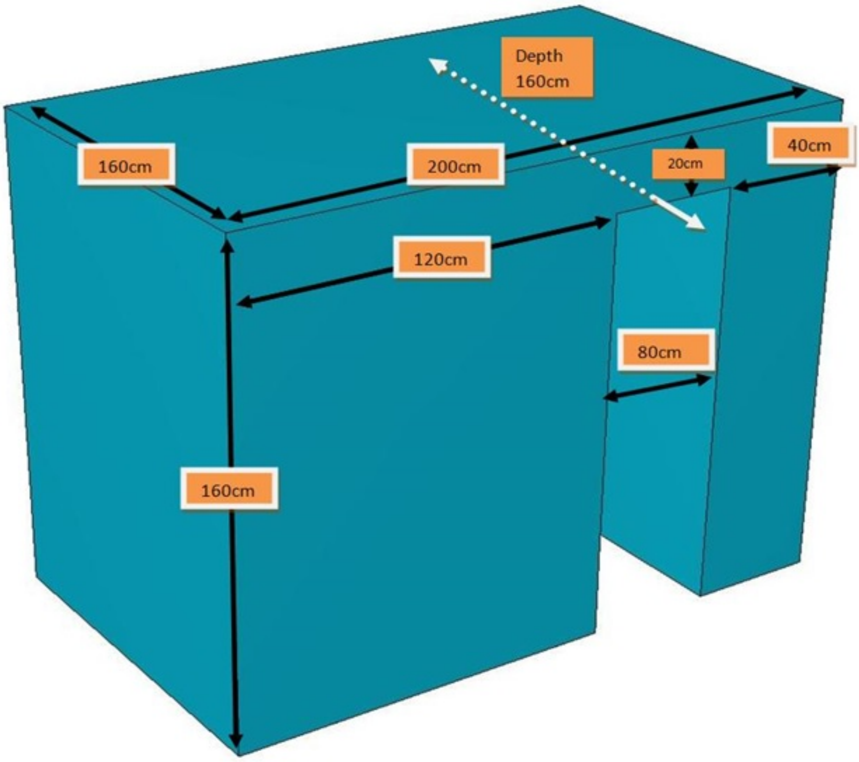

Figure 3.18: *The dimensions of the final design of the bunker. The side that is exposed to the flux of backscattered particles from the target has a total length of 1.2 m.*

Both the camera and the LDV were triggered by the beam. The camera was configured to also store 20 frames before the trigger, in order to allow for any trigger jitter. These 20 pre-trigger frames correspond to a time window of 10 ms for a framerate of 2000 fps and to 20 ms for a frame rate of 1000 fps. A total of 2000 frames could be stored in the camera's internal memory. After the trigger pulse, both the 20 pre-trigger and the 1980 post-trigger frames were recorded on the camera's memory, and had to be downloaded into the computer's hard disk before the subsequent shot.

The camera's field of view was configured to about 12.5×7 cm and the resolution of the obtained images was 768×480 pixels, thus corresponding to a pixel size of 161 μm on the horizontal axis and of 157 μm on the vertical axis. An example of the camera field of view is shown in Figure 3.20.

The LDV sampling frequency was set to the maximum available of 10.24 MHz. A total time window of 12 ms was recorded for each shot. As for the camera, the system recorded in a loop storing the signal in the internal memory and saved to disk 10% of the available sampling buffer preceding the beam trigger together with 90% of the signal following the beam trigger. The laser beam was focused on the target through the mirrors and the quality of the signal (as evaluated by the instrument itself) was quite satisfying, despite the long distance, the reflection through two mirrors and the beam permeation through the two observational windows of the apparatus.

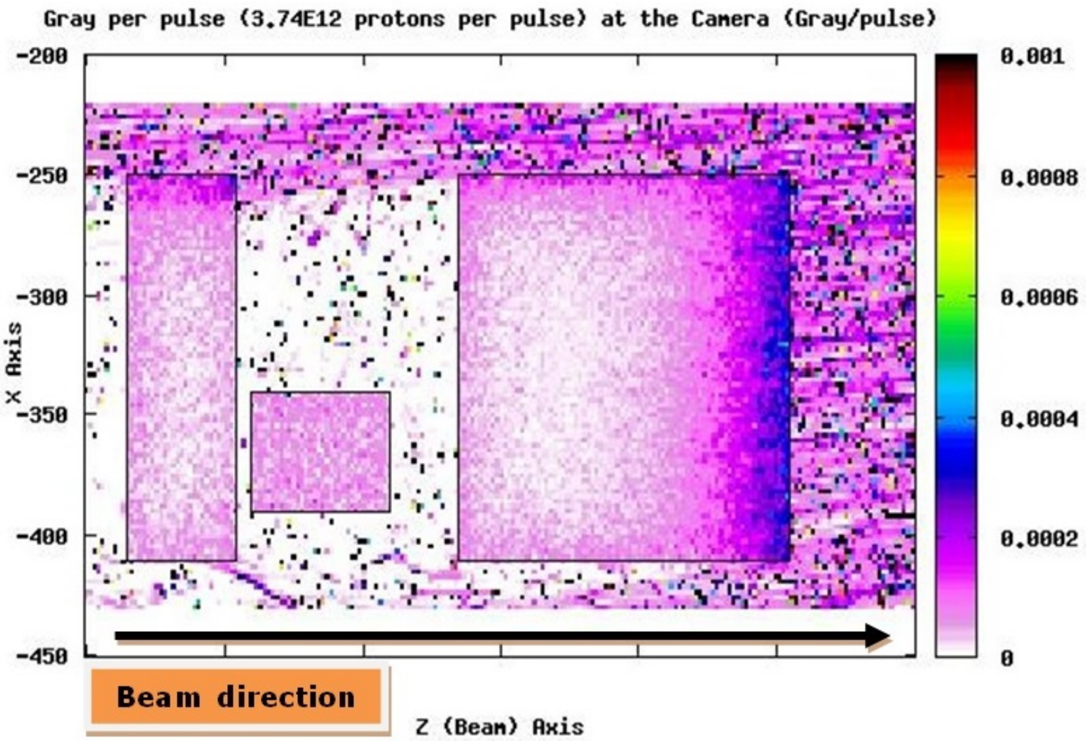

Figure 3.19: *The calculated dose on the camera (modeled as a box constructed by silicon) for an assumed proton pulse of* 3.74×10^{12}*. The dose on the camera was calculated to be about 0.2* mGy*.*

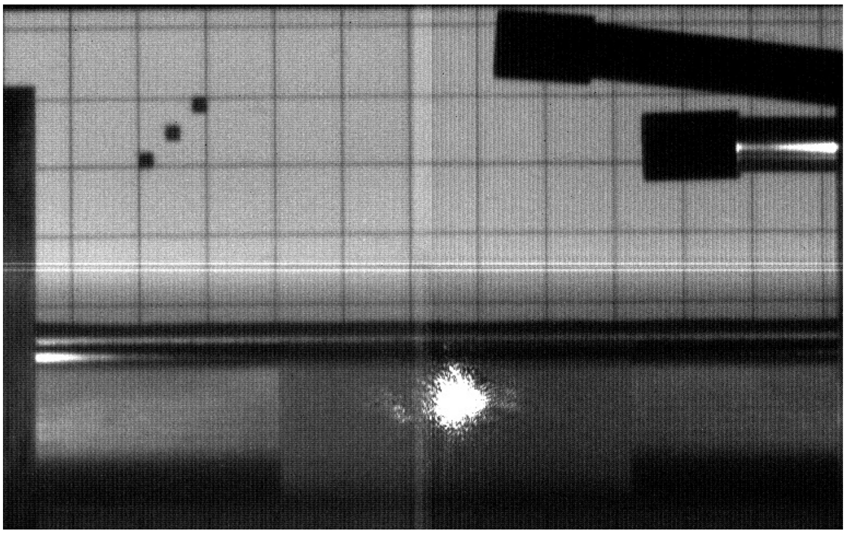

Figure 3.20: *One frame as recorded by the optical observation system (before beam impact). The upper surface of the powder is located at the lower edge of the 1-cm grid. The beam direction is from the left. The bright spot in the lower part of the image is the LDV beam pointed at the trough. The resolution of the photo is about* 160 μm *per pixel.*

3.4 Data taking

The experiment took place on 31/5/2012. In Table 3.2 information about the exact beam intensity, the spot size as well as the position of the LDV beam (inner or outer trough) can be found. A plot depicting the pulse intensity as a function of the shot number, can be seen in Figure 3.21.

During the data-taking procedure, coordination of the experimental team with the SPS control room was necessary. Each pulse had to be optimized in terms of intensity and spot size before being delivered on target; during these optimizations the experimental apparatus was moved out of the beam trajectory and the extracted preparatory shots were shot onto the dump. When the measured beam pulse parameters were matching the experiment's specifications, the target was moved back into the beam's trajectory, and the LED's were turned on.

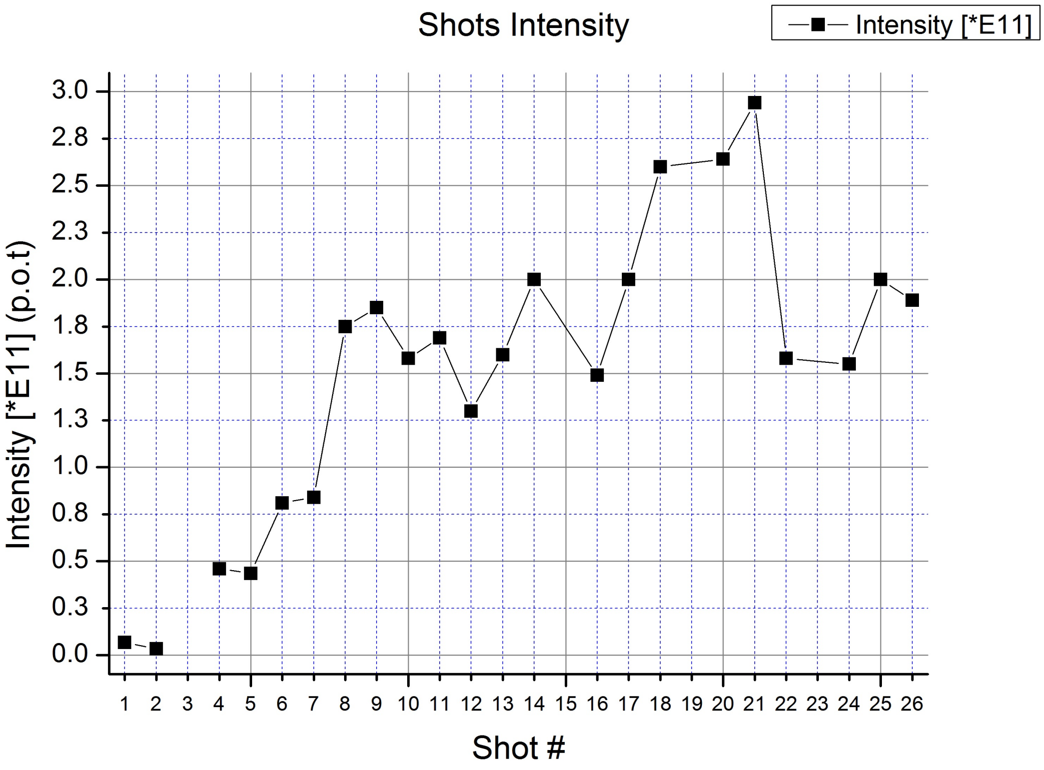

Figure 3.21: *The intensity of the pulses on target. From shot #22 and onwards, a different beam position was used.*

After the download of the data, a quick review of the high-speed images was performed, in order to roughly evaluate if any visible effect was present. The first major powder disruption appeared for an intensity of 1.75×10^{11} protons, at much lower intensity than expected from simulations with ANSYS (predicting the disruption threshold to be at 10^{12} protons). Therefore, the original pulse list of a maximum intensity of 3.74×10^{12} protons on target was abandoned, since for 2.94×10^{11} protons, the powder disruption was already very significant. That was the maximum intensity shot on target. It was decided instead of further increasing the intensity, to try changing the beam position by 2 mm higher in the vertical direction, in order to investigate the possibility that the beam position plays an important role in the powder disruption. The total number of protons shot on target for both beam positions was 3.31×10^{12}.

During the experiment's data taking procedure, the temperature of the LED stations was constantly monitored, as well as the pressure of the containers' helium atmosphere. No significant indications on these sensors appeared during the experimental procedure.

3.5 Activation of the target & decommissioning

In order to asses the necessary cooling time before a possible post-irradiation analysis of the target, a detailed set of Monte - Carlo simulations was performed for several cooling times. The results from these simulations, for a cooling time of 1 hour and 4 months, assuming the final total proton budget of the experiment to be equal to 3.31×10^{12} protons, are illustrated in Figures 3.22 and 3.23. As can be seen from the Figures, at least 4 months of cooling time were necessary in order for the dose rate in contact with the container to be less than 3 $\mu Sv/h$. Therefore, the mobile table with the experimental apparatus was remotely transferred to the facility's cool-down area, where it remained for almost 4 months after the experiment. After this time, the outer container was dismantled, and, without opening the inner container, photos of the powder surface inside the primary trough and the disrupted powder were taken. More information concerning the activation of HRMT-10 as well as the radionuclide inventory of the activated target can be found in [64].

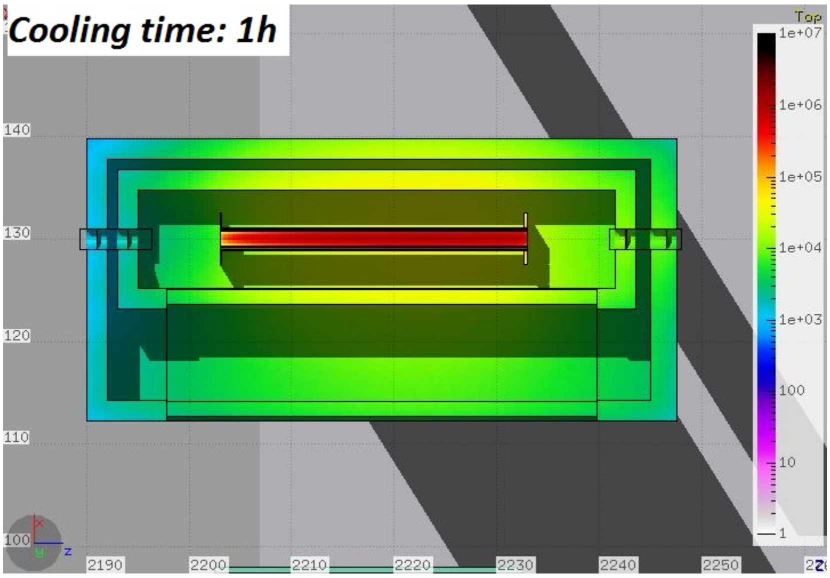

Figure 3.22: *Activation of the experimental apparatus, after a total proton budget of* 3.31×10^{12} *protons and a cooling time of 1 hour. The results are expressed in* $\mu Sv/h$.

#	B/p*	Intensity $\times 10^{11} p.o.t$	$\sigma_x[mm]$	$\sigma_y[mm]$	LDV pos.	f[kHz]	Pos.
1	1	0.068	N/A	N/A	IN	2	N
2	1	0.035	N/A	N/A	OUT	2	N
3	–	–	–	–	–	–	–
4	6	0.46	0.45	1.00	IN	2	N
5	6	0.43	0.76	1.09	OUT	2	N
6	6	0.81	0.77	1.23	IN	2	N
7	6	0.84	0.80	1.20	OUT	2	N
8	6	1.75	1.17	1.60	IN	2	N
9	6	1.85	1.07	1.30	OUT	2	N
10	6	1.58	0.93	1.66	IN	1	N
11	6	1.69	1.10	1.60	IN	2	N
12	6	1.30	2.15	1.61	IN	2	N
13	6	1.60	2.14	1.69	IN	1	N
14	6	2.00	2.33	1.88	OUT	1	N
15	–	–	–	–	–	–	–
16	36	1.49	1.00	1.51	IN	1	N
17	36	2.00	1.10	1.70	IN	1	N
18	36	2.60	1.37	1.79	OUT	2	N
19	–	–	–	–	–	–	–
20	36	2.64	1.31	1.81	IN	1	N
21	36	2.94	1.39	1.85	IN	1	N
22	36	1.58	0.92	1.66	IN	1	UP
23	–	–	–	–	–	1	UP
24	1	1.55	0.94	1.65	OUT	1	UP
25	1	2.00	0.94	1.66	IN	1	UP
26	1	1.89	1.22	1.41	IN	1	UP

Table 3.2: *The pulse list of the HRMT-10 experiment. In the third column the abbreviation "B/p" stands for "Bunches per pulse". In the pilot shots, information of the beam spot size was not available, while in shots #3, #15, #19 and #23 the beam was not extracted from the SPS. The error on the beam intensity and the spot size is around 3%. The abbreviation "IN" in the LDV position column means that the LDV was pointing on the inner trough, while the abbreviation "OUT" means that it was pointing on the outer trough. In the last column, the position of the beam is indicated. The abbreviation "N" means the beam was pointing in the nominal (6 mm below the powder free surface) position, while the abbreviation "UP" means that the beam was pointing in a higher position, i.e 4 mm from the powder's free surface. The total number of protons for the experiment was* 3.31×10^{12} *protons on target.*

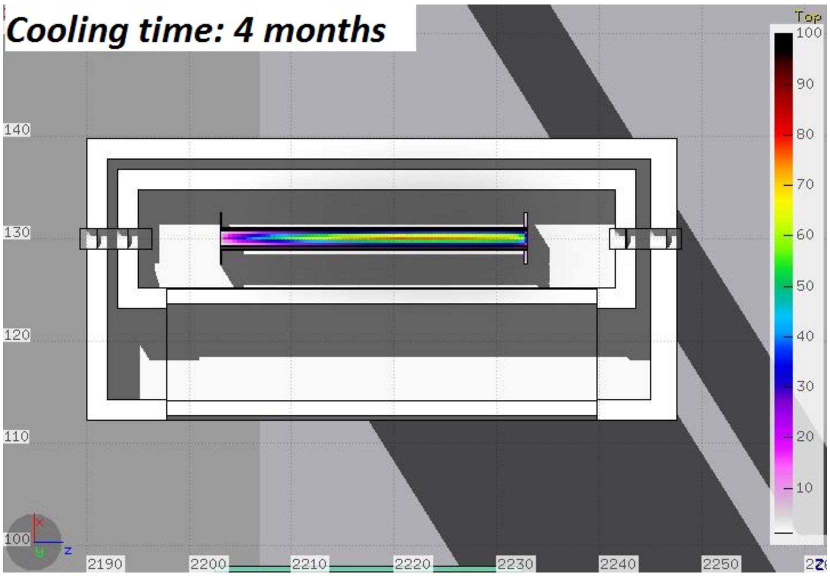

Figure 3.23: *Activation of the experimental apparatus, after a total proton budget of* 3.31×10^{12} *protons and a cooling time of 4 months. The results are expressed in* $\mu Sv/h$.

4 Data Analysis and Results

4.1 High Speed Images

4.1.1 Analysis

The images obtained during the data taking procedure were saved under the non-compressed **T**agged **I**mage **F**ile **F**ormat (TIFF) format. The data of each one of these images, could be extracted as a 480 × 768 array of values, each one within the range of 0 - 255 (8 bits), where 0 corresponds to black color and 255 to white. In order to observe and analyze the movement of the powder, the pixel values of a vertical ”stripe” corresponding to the average of 5 pixels along the horizontal (beam) axis, near the simulated shower maximum (~11 cm from the target front) was chosen (Figure 4.1).

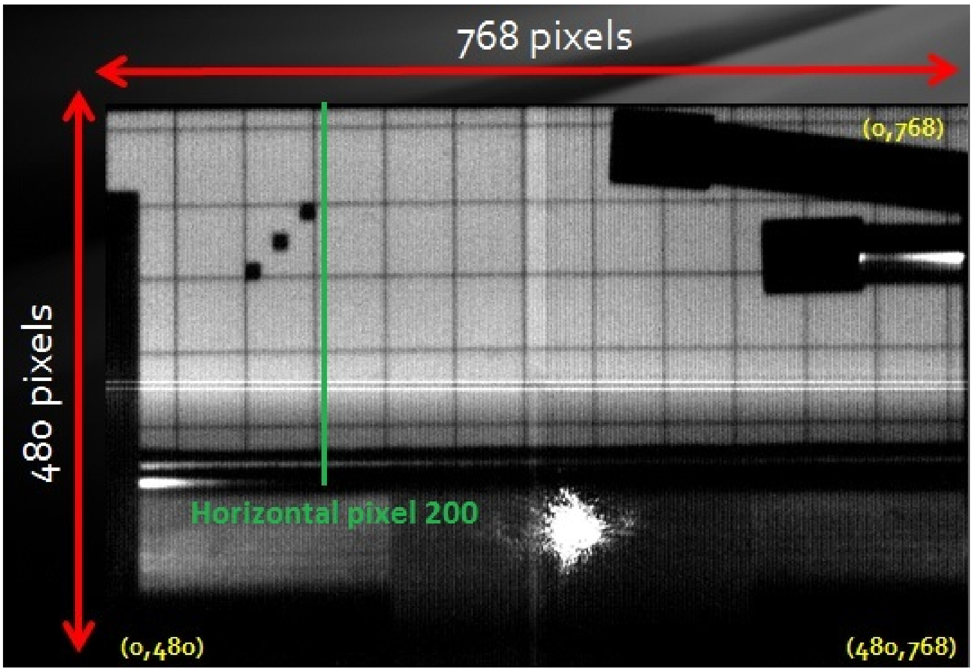

Figure 4.1: *One frame acquired by the high-speed camera. The green vertical line represents the average of 5 neighboring pixels around horizontal pixel # 200, which is about 11 cm from the target front.*

In order to algorithmically detect the powder movement in the chosen vertical stripe for all the frames of each one of the shots, two approaches could be followed. (a) The definition of the "background" (in terms of positions and corresponding pixel values) from the pre-trigger frames of each shot and its later subtraction from each post-trigger frame. Since the powder position in the vertical stripe changes in each frame, the difference between the pixel values of each frame and the background would define the position of the powder. An alternative approach would be, (b) the definition of a "threshold" pixel value. In each frame, the pixel values of the vertical stripe would be examined from top to bottom. The first pixel of the stripe that would have a value less than the threshold would define the powder height in the specific frame. However, in the digital images of HRMT-10 experiment, two factors made the approach (a) impractical to apply. These two factors were:

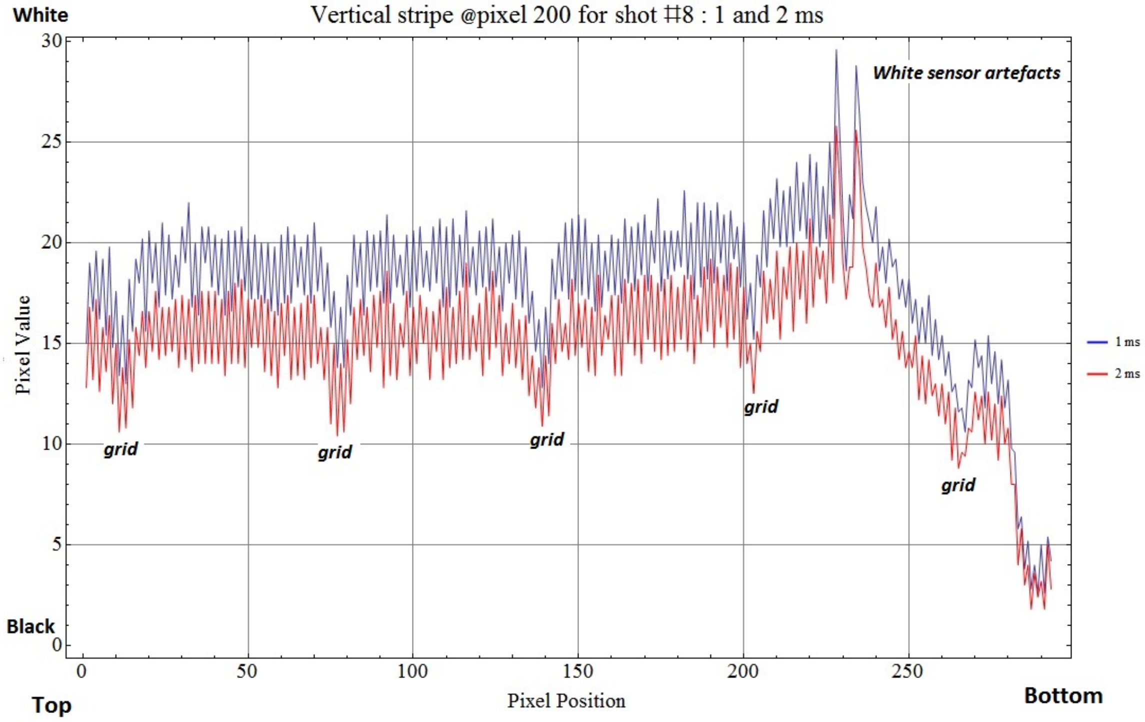

Figure 4.2: *An illustration of the pixel values of the vertical stripe for 1 and 2 ms after the trigger. The x-axis is the pixel position from top to bottom (corresponding to the powder height) where the y-axis corresponds to the pixel value (in bytes, where 0 corresponds to "black" and 255 to "white"). It can be seen that at 2 ms, due the LED failure, the whole background went darker. In some of the shots, after some milliseconds, the lighting was re-estated as discussed in the text.*

1. The failure of the LED's due to radiation. It was observed that, 1 ms after the beam impingement on the target, some of the LED's were turned off and, in some cases, after some milliseconds were observed to turn back on. The cause of this effect is the amount of prompt radiation impinging on the LED's. Therefore the

defined background at the pre-trigger frames was different from the post-trigger ones, and therefore could not be subtracted. An illustration of the background difference due to the LED failure for shot #8 can be seen in Figure 4.2.

2. The shadow of the powder and the trough. The direct light by the LED's illuminating the target, cast a shadow of the trough and the powder itself which was visible in the photograph background (Figure 4.3). As the powder was disrupting, the shadow movement was preceding the powder movement, changing therefore in each frame the background, compared with the pre-trigger. An illustration of the effect can be seen in Figure 4.4.

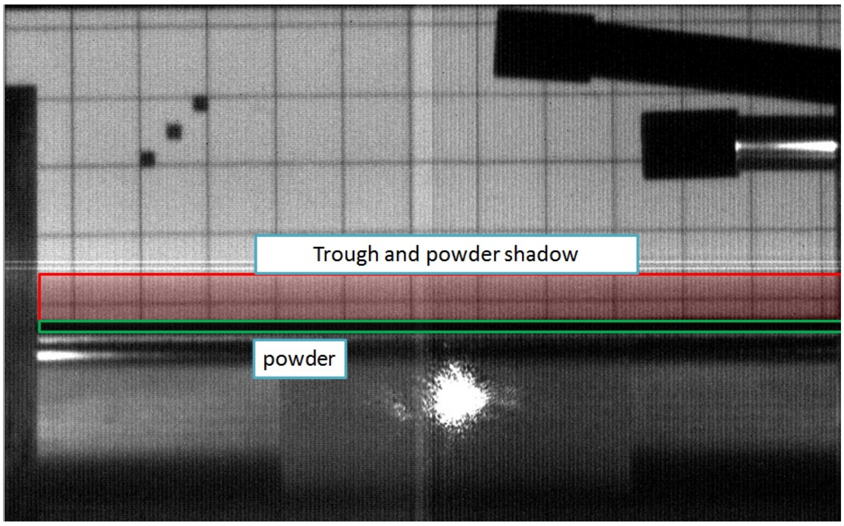

Figure 4.3: *The pre-trigger frame of shot #8. The shadow of the trough and the powder cast in the background is illustrated inside the red box.*

For the aforementioned reasons, approach (b) was chosen in order to define, in each frame, the position of the powder. The threshold should be quite strict in order to be robust in the background changes due to the shadow and the failure of the LED's. In order to correctly choose the threshold value, the pixel values of the first 40 pixels (from the top) of the chosen vertical stripe were extracted for the 20 pre-trigger frames. These pixels were enough to define the background, since they include the white background and the grid line. The threshold was defined as a multiple of the maximum standard deviation found in any of these values, subtracted from the minimum pixel value found in these 40 pixels. The resulting pixel value was defined as "threshold". The powder height corresponding to 6 thresholds (3 strict & 3 lenient) were applied for each shot in order to define the powder movement. The final dataset for each shot consists of the mean value of the six results along with their standard deviation.

After the definition of the threshold in each shot, for each one of the recorded frames, the algorithm detects the pixel values of the vertical stripe described above and compares them with the chosen threshold. The first pixel (from top to bottom) that will be

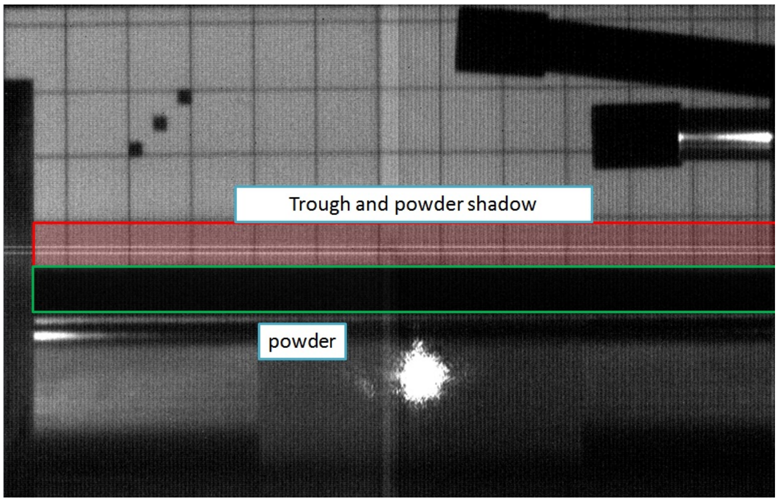

Figure 4.4: *The frame corresponding to 15 ms after the beam impact, for shot #8. The powder has disrupted, and its shadow precedes its movement. The background is different compared with the pre-trigger frames.*

found in each frame to have a value lower than threshold, is recognized as the "powder height" at the specific frame. An illustration of the pixel values for the stripe and the chosen threshold can be seen in Figure 4.5.

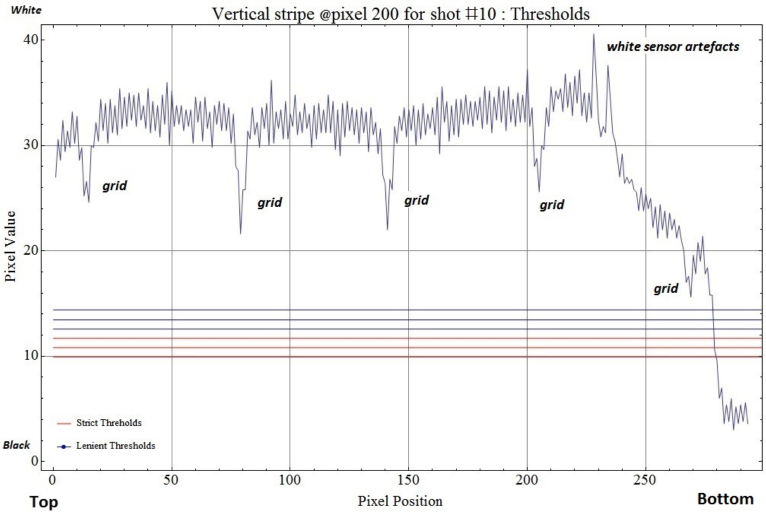

Figure 4.5: *An illustration of the chosen thresholds, for shot #10, for the frame corresponding to 5 ms after the beam impact. The x-axis corresponds to the pixel position (from top to bottom) while the y-axis corresponds to the pixel value (in bytes, 0 corresponds to "black" and 255 to "white"). The three horizontal red lines correspond to the three strict thresholds chosen to determine the powder height, while the three blue correspond to the three lenient thresholds. The final height is determined from the mean height given from all six thresholds and their standard deviation. The five spikes at positions < 270 correspond to the black grid lines, while the two spikes near pixel 240 correspond to two artefact lines of the camera sensor.*

Type-I error correction

In addition to the threshold choice algorithm, an algorithmic module to correct Type-I (false positives) errors of powder detection was implemented. This module applies each time that the powder height is detected, for all 6 thresholds. More specifically, if the pixel in a vertical position k has a value lower than the defined threshold, the algorithm checks the value of the pixel positioned in k+10 pixels. If the value of the pixel positioned at k+10 still has a lower value than the defined threshold, then the algorithm recognizes position k as the powder height in the specific frame. In the opposite case, it recognizes a false positive continuing to scan the stripe's pixel values.

This module assumes that the powder moves homogeneously in the stripe and during the disruption the grain clusters are not vertically separated by more than 1.6 mm (distance that corresponds to 10 pixels). Due to the resolution of the photographs, the detection of a single grain was not possible. A visualisation of the calculated powder height for shot #10 can be seen in Figure 4.6, and example of the result of the data extraction algorithm alongside with the Type-I error correcting module can be seen in Figure 4.7.

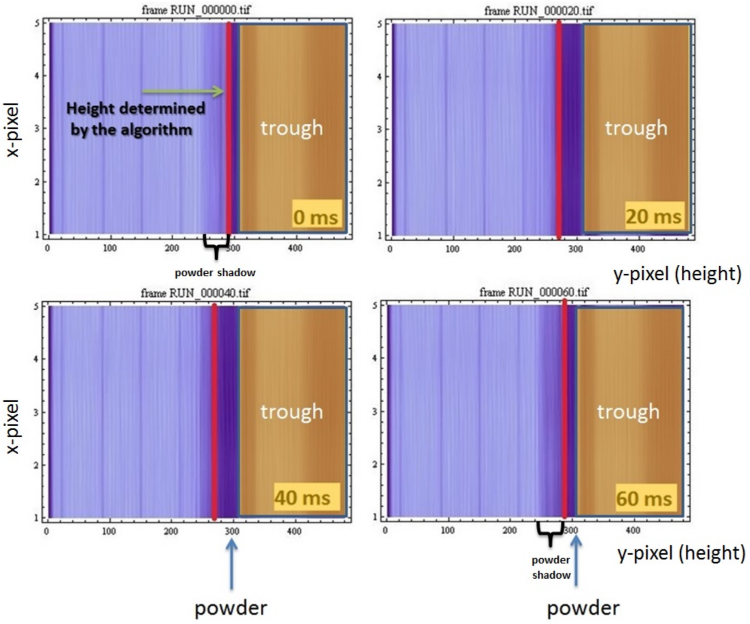

Figure 4.6: *Selected frames from shot #10. The frames are rotated by 90 degrees for visualisation reasons. The y-axis corresponds to the five horizontal pixels over which the analysis is averaged (in this case pixels 198 - 202). The x-axis corresponds to the vertical pixel lane. Near pixel 300 the powder can be distinguished. The red line corresponds to the powder height defined by the algorithm for each frame for that shot, for 3rd out of the 6 thresholds. The label of each frame indicates the millisecond after the beam impact. At any case, it is clear that the algorithm detects very well the vertical movement of the powder.*

The final result of the data extraction, after conversion of pixel positions to millimeters and of frames to milliseconds (the resting position of the powder, was chosen by convention to be 0 mm), can be seen in Figure 4.8 for shot #10 as illustration. The height

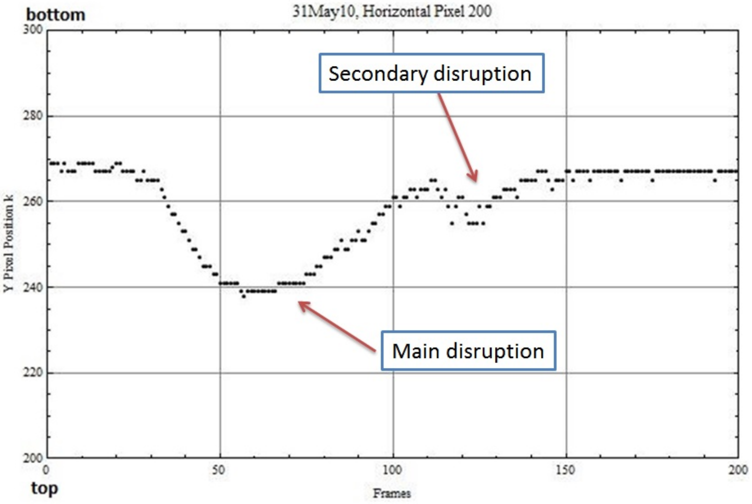

Figure 4.7: *The result of the data extraction algorithm and the Type-I error correcting module for shot #10. In the pre-trigger frames, the powder does not move, and its position remains the same throughout the frames. As the beam arrives, the powder movement through the frames is detected. The x-axis corresponds to the frame number, while the y-axis is the vertical pixel position, where the top corresponds to pixel 0 and the powder position at the pre-trigger is around pixel 270. Around frame 120, a secondary disruption begins in shot #10, which is also detected by the algorithm.*

of all the powder shots can be found in the appendix A.

From Figures 4.8 and 4.9 can be seen that the algorithm detects very well the powder movement. In the specific shot, the powder disruption is relatively homogeneous in the first 25 ms, and there is no big deviation between the different thresholds. As the powder reaches its maximum height, some grains start falling and some others continue moving up. The density of the powder is reduced, and therefore the deviation between the thresholds is bigger. The powder descent detection therefore has bigger uncertainty than the ascent.

4.1.2 Results

During the experiment, the powder disrupted in many different ways. The results of the digital image analysis for three different pixel stripes, corresponding to horizontal pixels #200, #210 and #220 are hereby presented. These three pixel stripes are located at a distance of 11.15, 11.30 and 11.45 cm from the target front. Their position is indicated in Figure 4.10. The specific pixel stripes were chosen for the analysis because they are located near the expected shower maximum of the hadronic interaction of the beam with the target. The horizontal distance between the three stripes is ~1.5 mm.

Maximum Powder Height

In Figure 4.11 the maximum height of the powder as a function of the pulse intensity is presented for the three different pixel stripes. It is obvious that the maximum height of

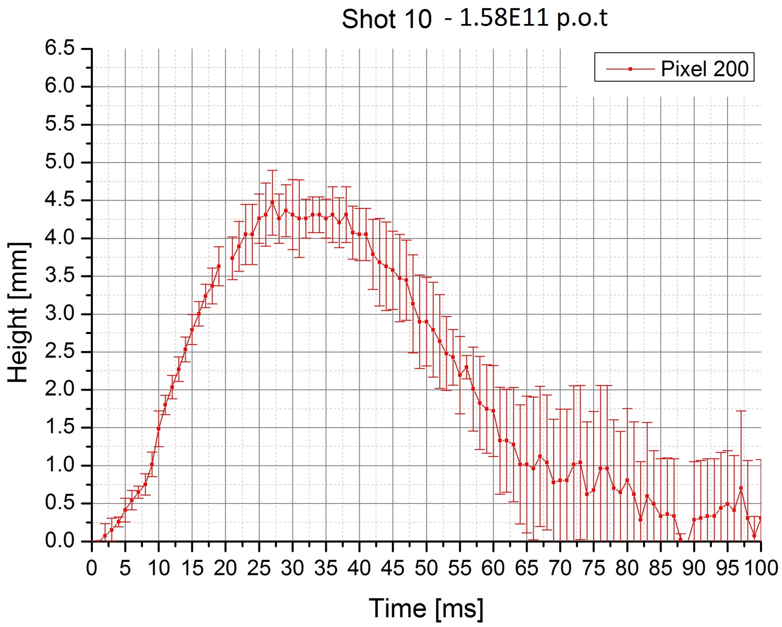

Figure 4.8: *Movement of the tungsten powder for shot #10. The data points represent the mean value of the powder position from 6 different thresholds, and the error bars the standard deviation of this value. In this specific shot a secondary disruption was observed, as it can be seen in times* $90\ ms$.

the powder scales with the beam intensity, and no big differences appear between the three different pixel stripes. The maximum height appears for 2.94×10^{11} protons on target, which was the most intense shot of the experiment.

It is obvious that the maximum height of the powder scales with the beam intensity, and no big differences appear between the three different pixel stripes. The maximum height appears for 2.94×10^{11} protons on target.

Time Evolution of the Disruption

The first and most subtle movement of the powder occurred after the impact of 8.40×10^{10} protons on target. In all subsequent shots with higher intensity than that, a disruption was observed. Shots with lower intensity did not cause any observable powder disruption. The evolution of the disruption as a function of the beam intensity is illustrated in Figure 4.12. From that plot it is verified that the duration of the disruption scales with the pulse intensity, as expected.

The first major disruptions - Shot #8 and Shot #9

As mentioned earlier, up to shot #5 (intensity 4.36×10^{10} p.o.t), no movement of the powder was observed. At shot #6, the first slight movement of powder was observed. Therefore, in can be stated that the threshold of powder disruption lies between 4.36 and 8.1×10^{10} p.o.t. In shot #8, where the beam had an intensity of 1.75×10^{11} protons

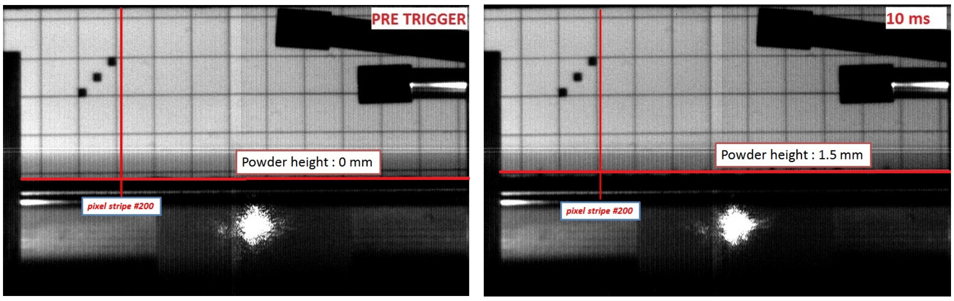

(a) *pre-trigger* **(b)** *10 ms*

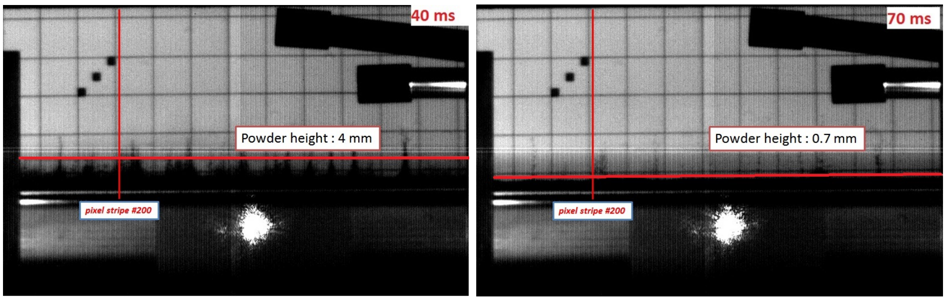

(c) *40 ms* **(d)** *70 ms*

Figure 4.9: *Disruption Evolution of shot # 10, (1.58×10^{11} p.o.t). The vertical red line corresponds to the position of the vertical stripe of pixel #200, and the horizontal to the powder height in every frame, plotted for visualisation reasons.*

on target, the first major disruption was observed. The powder disrupted quite homogeneously, without filaments [1]. The height of the powder as a function of the time for the specific shot can be seen in Figure 4.13, while selected frames of the disruption can be found in Figure 4.14.

In all the subsequent shots, the disruption of the powder included filaments. This behavior can be explained by the fact that, after the disruption of shot #8, the powder surface was not smooth anymore. An increased roughness on the powder surface can possibly account for the behaviour of shot #9, which, despite having a similar intensity with shot #8 (1.85×10^{11} p.o.t), disrupted in a totally different way (see Figure 4.15).

---

[1] Filament: An elongated thread of powder.

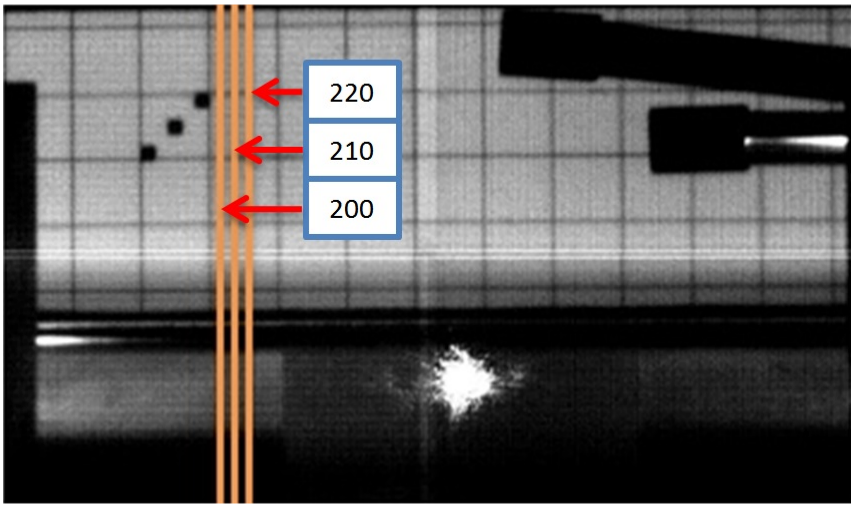

Figure 4.10: *The positions of pixel #200, #210 and #220 are indicated with the orange vertical lines. The horizontal distance between them is ∼1.5 mm.*

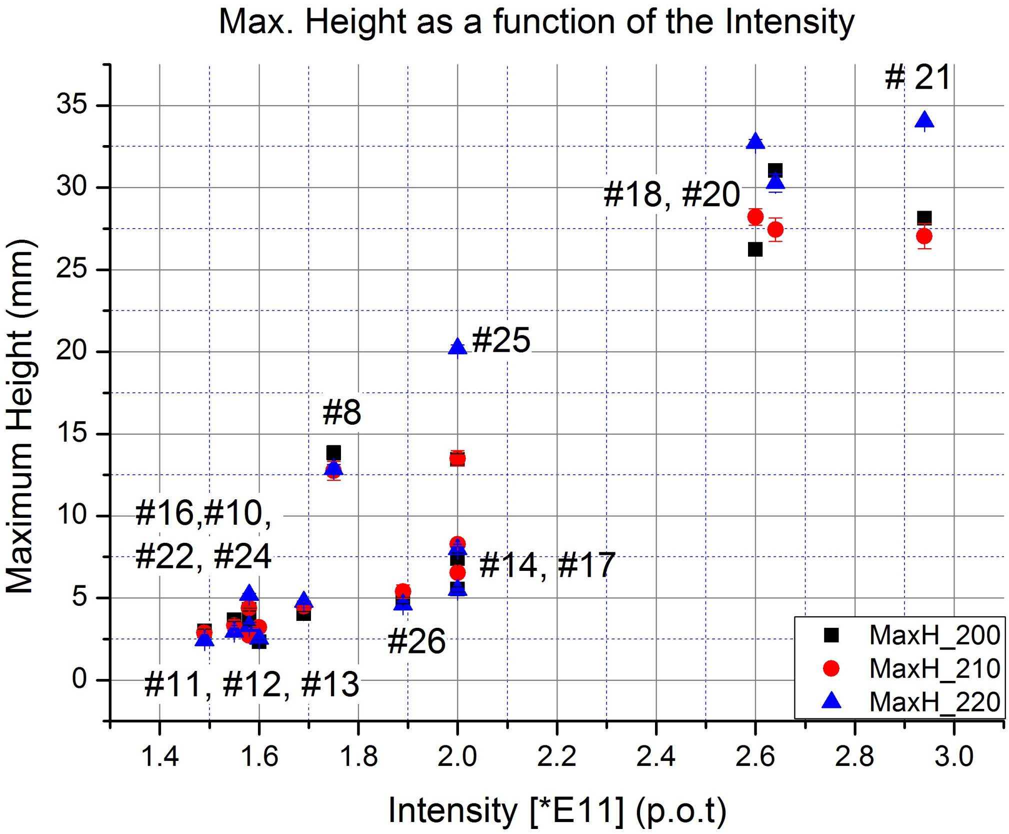

Figure 4.11: *The maximum height as a function of the intensity, for all the shots in the nominal beam position. Values are given for the three different stripes described in the text.*

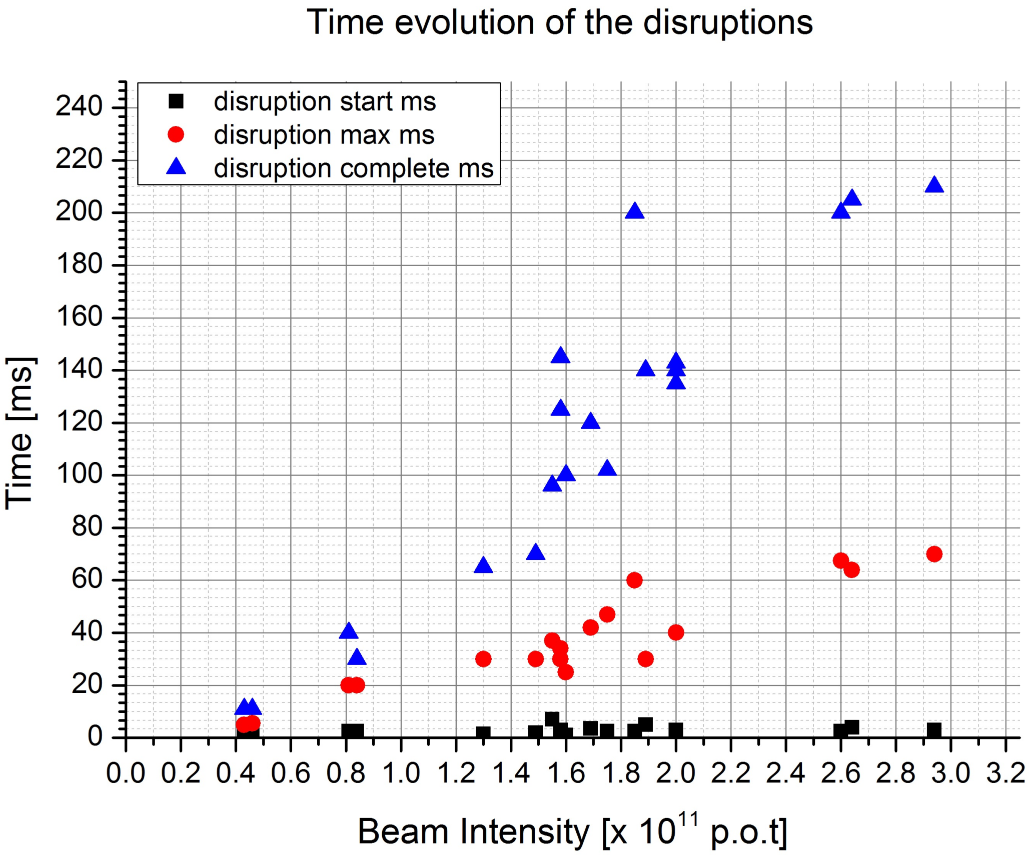

Figure 4.12: *Evolution of the powder disruption as a function of the beam intensity. The black points correspond to the time that the disruption begins; the red points correspond to the time that the disruption is at its maximum height; the blue points correspond to the time that the disruption has been completed, and the powder has returned to stagnation. The disruption evolution scales with the beam intensity.*

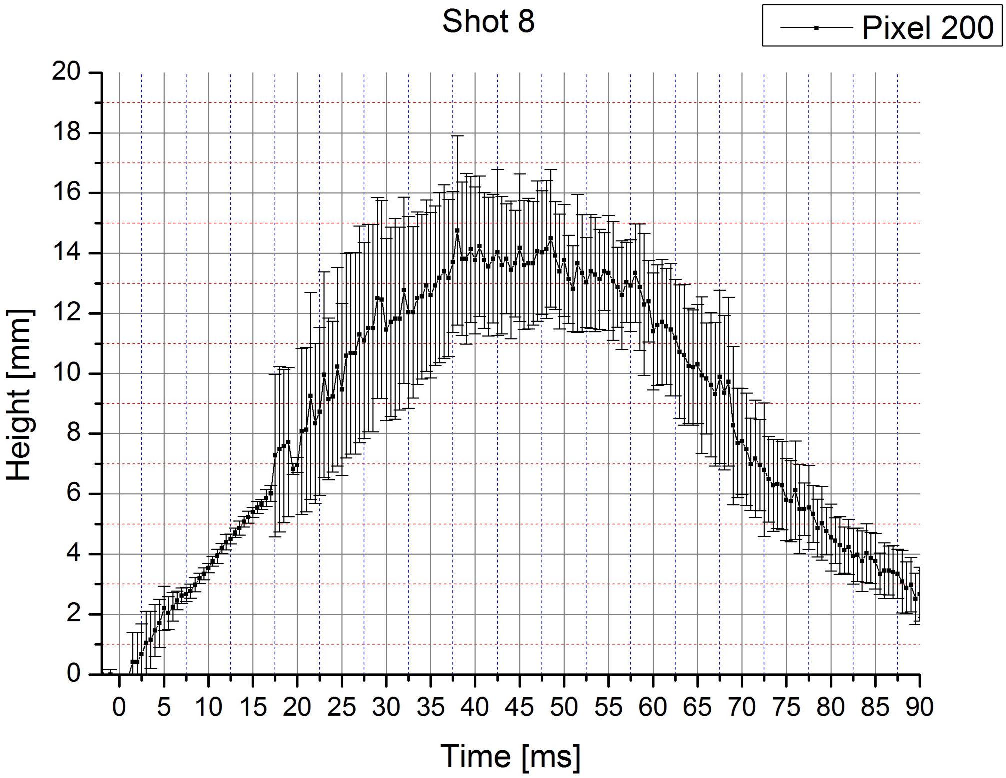

Figure 4.13: *The powder movement for pixel # 200 of shot #8. We can see that for the first 17* ms *the powder disrupts homogeneously. The bigger error bars for* $t \geq \sim 17ms$ *are due to the fact that few and smaller grains clusters are seperated from the main powder body adding therefore uncertainty in the determination of the exact position of the powder.*

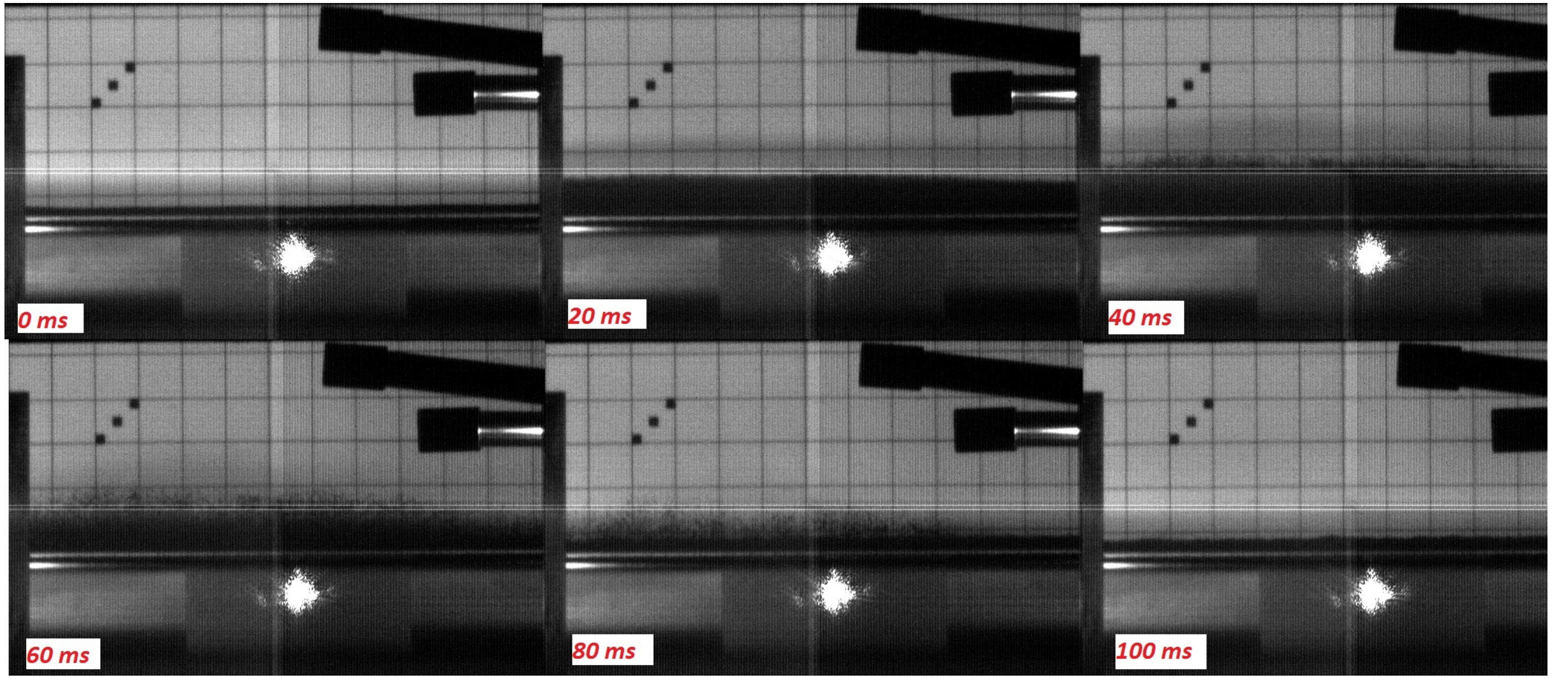

Figure 4.14: *Selected frames from shot #8, where the first major disruption was observed. The beam impinges from the left, 6* mm *below the powder free surface. The maximum height reached by the grains is* 13.84 ± 0.44 mm *after* 40 ms*, while the maximum grain velocity is measured to be* 0.41 ± 0.11 m/s.

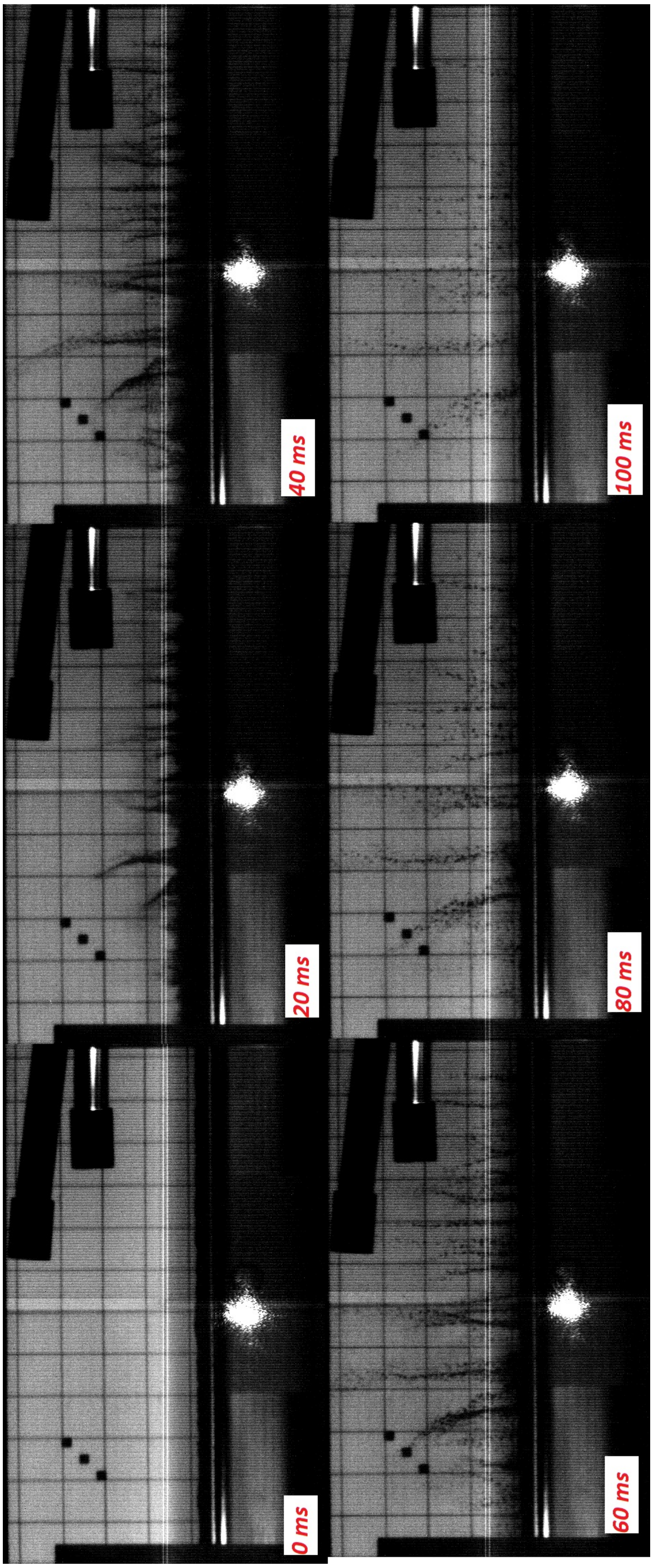

Figure 4.15: *Selected frames from shot #9. The extended filamentation is most probably due to the roughness of the powder surface, caused by shot #8.*

Secondary Disruptions

In shot #10 for the first time, and in only for the next four subsequent shots, two secondary disruption spots appeared after the conclusion of the main disruption the powder (at about ~65 ms). The powder in these disruptions reaches at lower maximum height compared with the main disruption. It can be theorized that these secondary disruptions correspond to a shock wave propagation inside the target trough. A plot showing the duration of these secondary disruptions as a function of the beam intensity can be seen in Figure 4.16, and the frames into which the disruptions appear for first time at shot #10 can be seen in Figure 4.17.

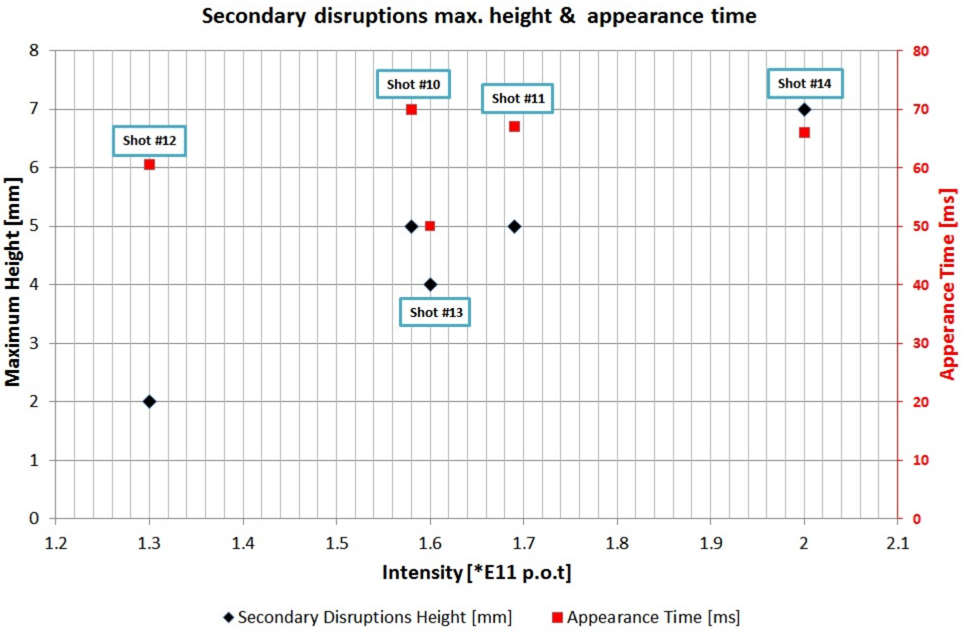

Figure 4.16: *The black data series and the left y-axis correspond to the maximum height of the powder (in mm) during the secondary disruptions. It can be theorized that the secondary disruptions correspond to a traveling shock wave inside the powder target, as discussed in the text. The red data series and the left y-axis correspond to the ms after the beam impact that the secondary disruptions appear for first time.*

4.2 LDV Data

4.2.1 Analysis

As already mentioned, the sampling frequency of the LDV was 10.24 MHz. The data of the troughs velocity were extracted as a 131072×2 array of data, the first column of which corresponds to the time (in intervals of 9.76×10^{-8} seconds) and the second to the velocity of the inner/outer trough in m/s. An example of the extracted LDV data for shot #9 can be seen in Figure 4.18.

Applying **F**ast **F**ourier **T**ransform [65] on the velocity data, the frequency spectrum of the movement was obtained. An example of the frequency spectrum corresponding to shot #9 can be seen in Figure 4.19.

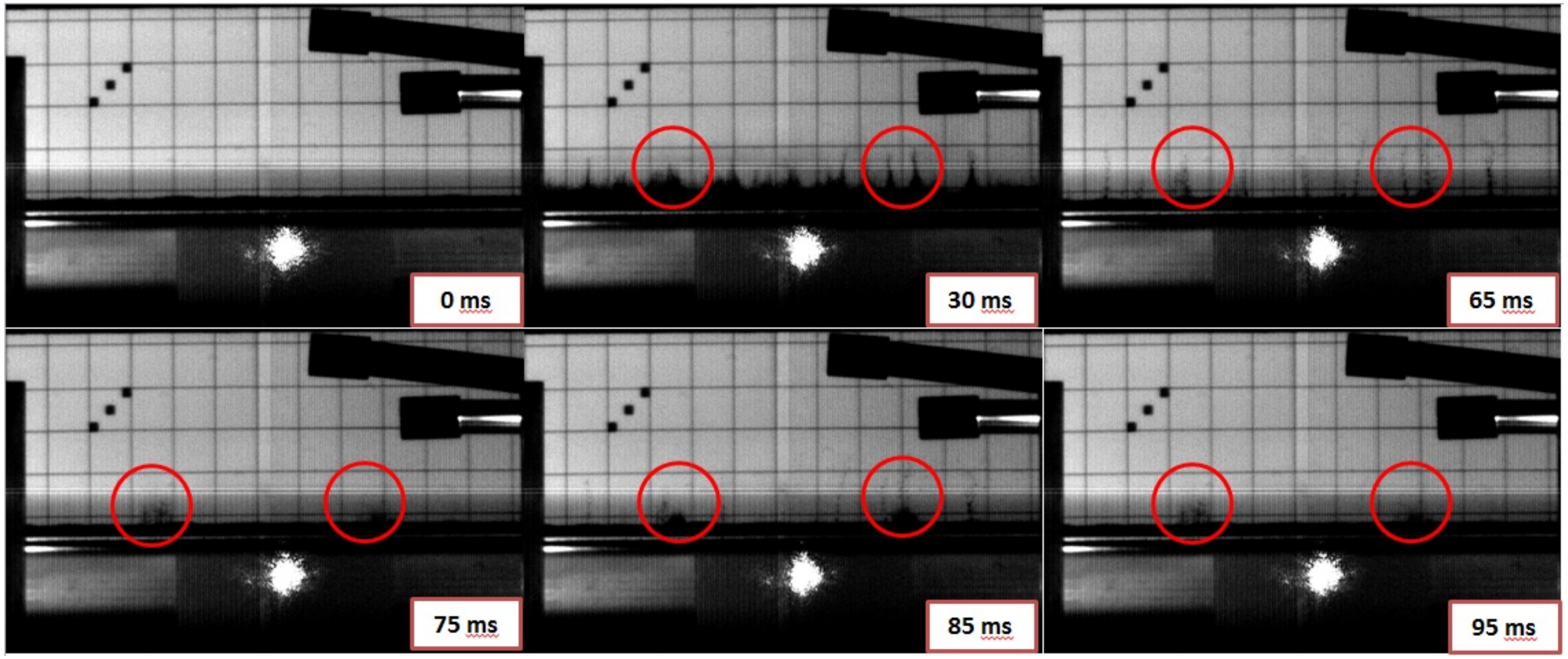

Figure 4.17: *The secondary disruption spots as they appear in shot #10. At ~65 ms the first secondary spot appears, while only a few ms later the second appears. For visualization reasons a red circle is enclosing the secondary disruptions.*

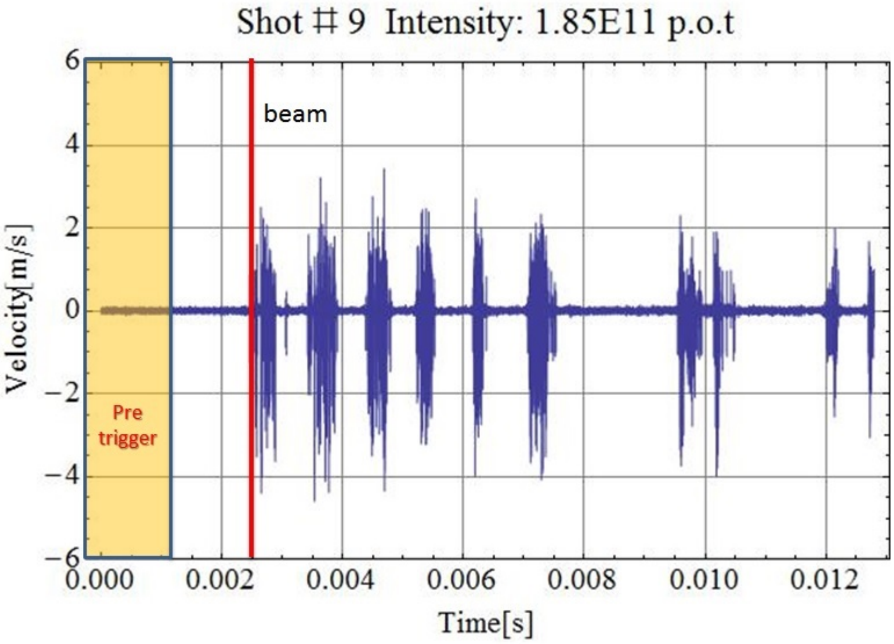

Figure 4.18: *The extracted LDV data for shot #9. The x-axis corresponds to the time, and the y-axis to the measured velocity of the trough. For the specific shot, the LDV was pointed in the secondary trough. The difference between the beam impact and the end of the pre-trigger frames is due to a jitter, as discussed in the text.*

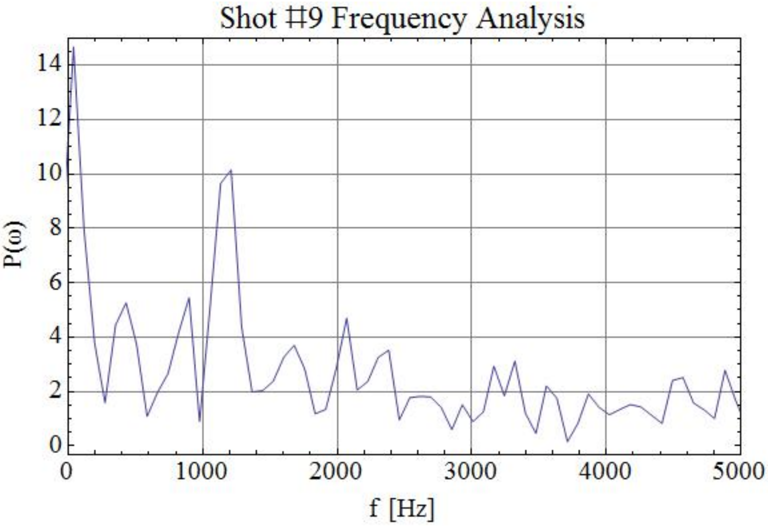

Figure 4.19: *The frequency spectrum for shot #9. Frequencies higher than 5 kHz have been omitted from the plot for visualization purposes. A dominant frequency of ~1.2 kHz can be seen.*

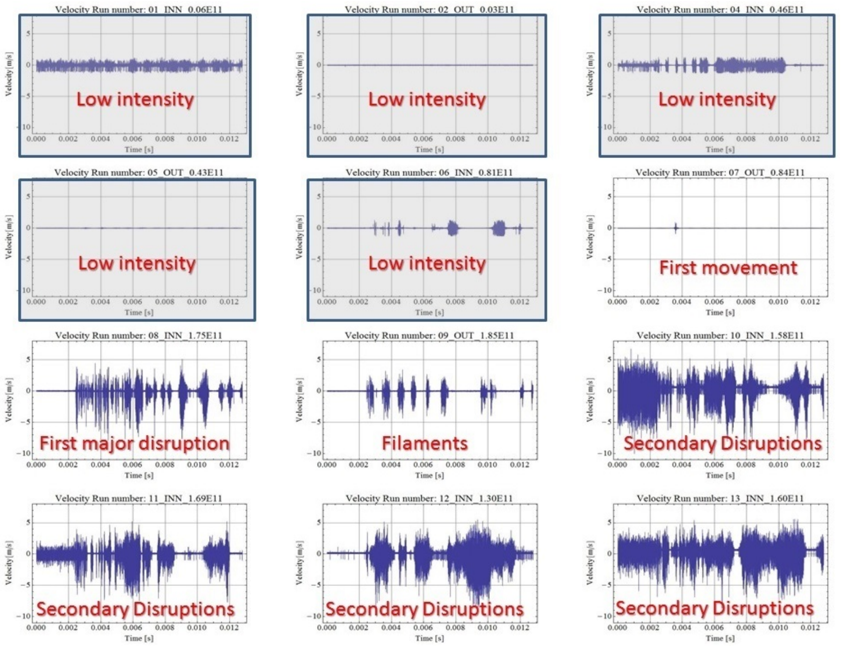

Figure 4.20: *The velocity data recorded by the LDV for the shots 1-13. Shot #3 is omitted since no beam was extracted on target. The x-axis of each plot corresponds to the time, on a total recording window of 12* ms*. The first* 1.2 ms *correspond to the pre-trigger signal, while the beam arrives at about* 1 ms *after the end of the pre-trigger window, as discussed in the text. The title of each plot declares the shot number(as it appears in Table 3.2). The abbreviation "INN" on each plot's label means that the LDV beam was pointing in the inner trough, while the abbreviation "OUT" on the outer. In shot #10 noise of unknown source and large amplitude exists in the pre-trigger frames, as in shot #13. It can be noticed that despite the observations from the high-speed images, no concluding evidence concerning the observed phenomena can be deducted from the LDV data.*

4.2.2 Results

The results of the velocity measurements recorded by the LDV for all the shots can be seen in Figures 4.20 and 4.21. During the first, lower intensity pulses, the magnitude of the gas pressure was not enough to move the powder grains, however it caused a vibration of the containers. The first major disruption occurred in shot #8, with an intensity of 1.75×10^{11} protons and a spot size equal to 1.87 m^2. The recorded trough velocity in this shot was significantly increased compared with the previous ones. From the analysis of the velocity measurements from all the shots, it was observed that in some of them, higher background noise was recorded during the pre-trigger time window. For example, the signal from shot #8 has much less background noise compared with shot #10. The source of this increased background noise in some of the shots remains still unknown. It can be however theorized that this behavior is due to the radiation impact on the LDV itself or the readout card installed inside the data-acquisition computer.

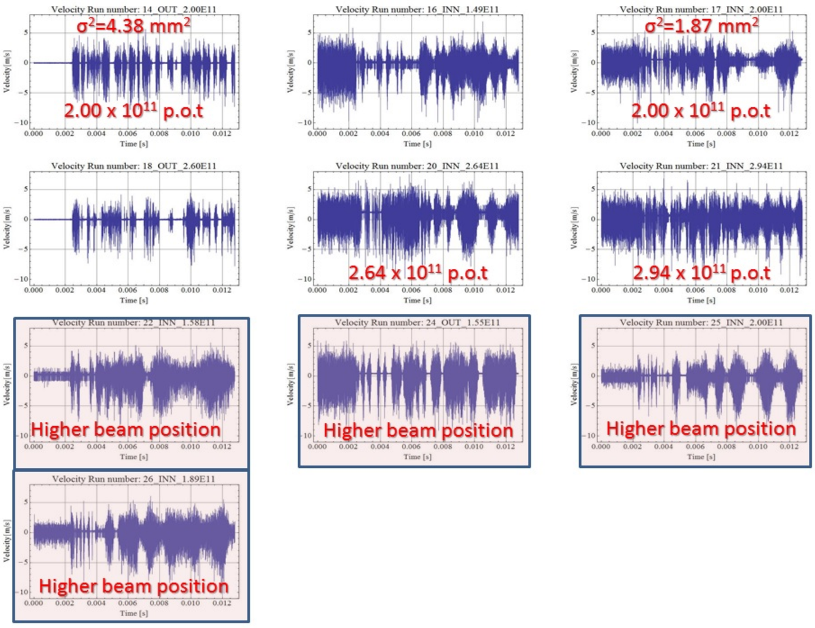

Figure 4.21: *The velocity data recorded by the LDV for the shots 14-26. Shots #15, #19 and #23 are omitted from the plot since no beam was extracted on target. In shot #21 the most violent powder disruption was observed. In shots #16, #17, #20, #21 and #24, noise of unknown source and large amplitude appears in the pre-trigger frames.*

Beam trigger jitter

An electronic signal ("trigger") was sent to the LDV and the high-speed camera for indicating the beam extraction and activate the camera and the LDV. However, this trigger was subject to an intrinsic jitter, of the order of magnitude of a few ms. Therefore, there is a slight difference between the end of the pre-trigger time-window of the instruments and the actual presence of the beam. Nonetheless, since the secondary particles due the beam interaction with the target cause **S**ingle **E**vent **U**psets (SEU) on the camera sensor, the exact frame of the beam arrival could be determined. In addition, from the LDV data the first vibrations could be distinguished within an uncertainty of 10 % - 15% from the pre-trigger background signal. All this information is concentrated in Figure 4.22, from which it can be determined that the trigger jitter is, at any case, less than 2.2 ms.

Frequency Analysis

A Fourier analysis performed on the LDV data revealed the underlying frequencies of the vibrations. An overview plot of the frequency analysis of each shot can be seen in Figure 4.23. Due to the high noise of the measurements, not clear deductions concerning any dominant frequencies can be made. However, comparing the frequency spectrum and the calculated displacement from shots #8 (intensity 1.75×10^{11} p.o.t) and shot #9 (intensity 1.85×10^{11} p.o.t), it can be seen that (a) the velocity of the primary trough is greater than the velocity of the outer and (b) a resonant peak is present at around 1.2 kHz, which had been predicted by ANSYS simulations [67].

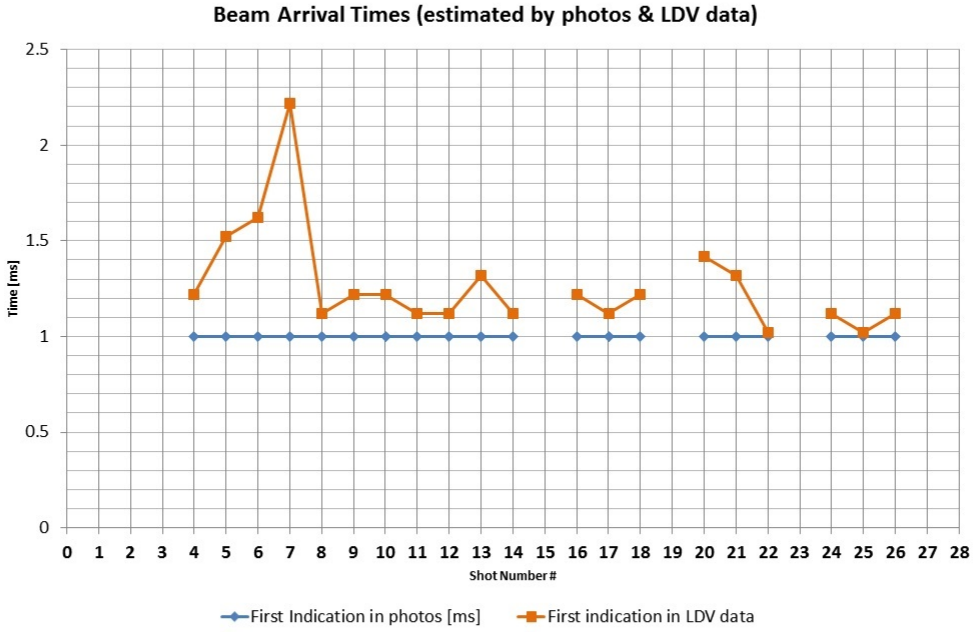

Figure 4.22: *Estimation of the beam arrival time by the photos and the LDV data. For shots #1 and #2 no single event upsets or clear indication of the start of a vibration could be found, due to the very low beam intensity. In shots #3, #15, #19 and #23 no beam was extracted. In the majority of the shots the beam arrival is estimated to be between* 1 *and* 1.5 ms*, thus indicating a jitter of this magnitude in the electronic trigger. In shot #7, the beam arrival time is estimated to be between 1 and 2.2* ms*.*

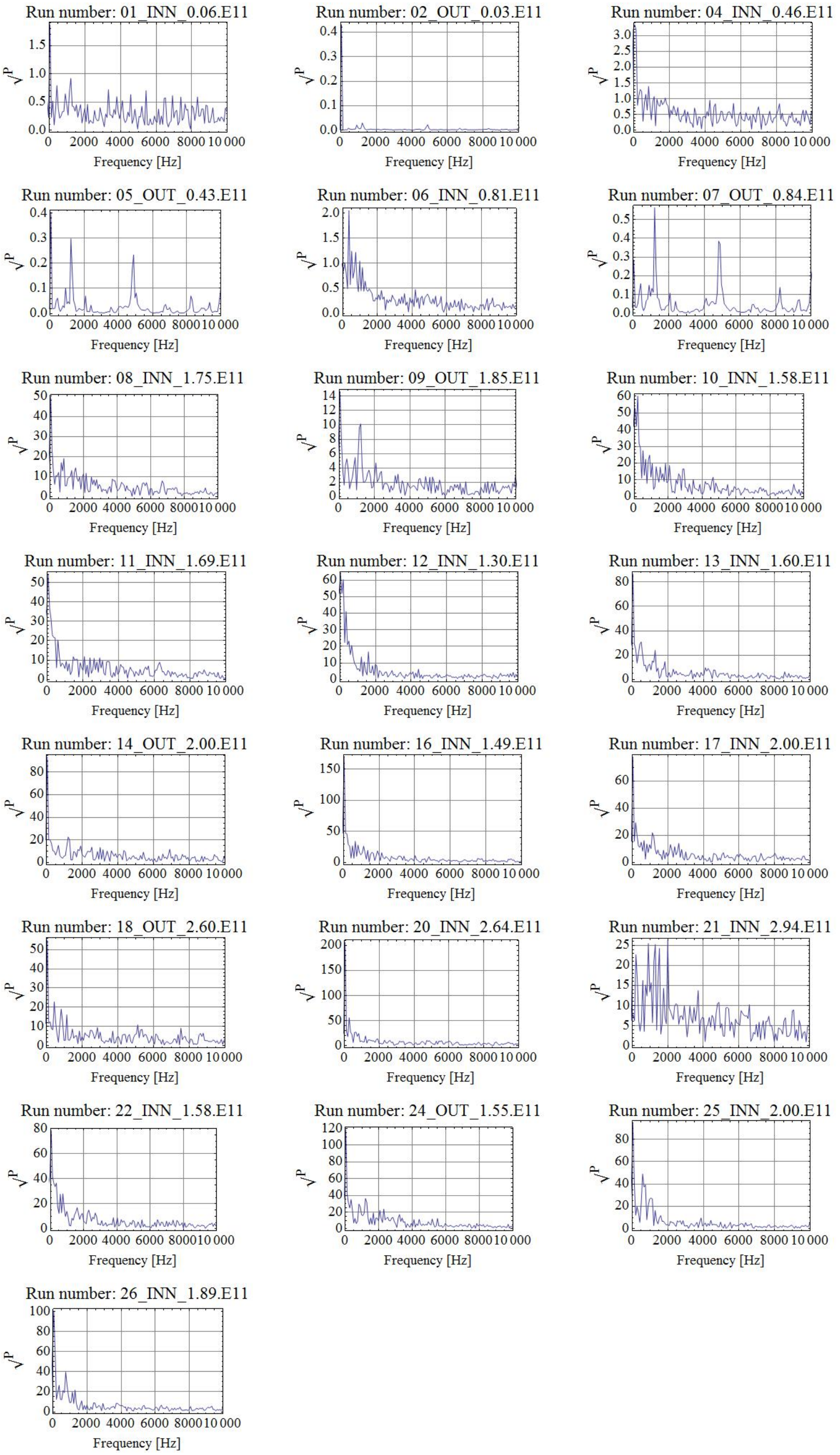

Figure 4.23: *An overview plot with the frequency analysis of all the plots. As in Figures 4.20 and 4.21, shots #3, #15, #19 and #23 are omitted from the plot since no beam was extracted on target. The x-axis of each plot is the frequency in Hz. The y-axis is the square root of the fourier power amplitude, indicating the "strength" of each frequency. The title of each plot declares the shot number(as it appears in Table 3.2). The abbreviation "INN" on each plot's label means that the LDV beam was pointing in the inner trough, where the abbreviation "OUT" on the outer.*

Conclusions

Despite the limitations, the following information was extracted from the LDV data analysis:

- **Resonant Peak around 1.2 kHz**. The frequency analysis of the LDV data confirms a resonant peak around 1.2 kHz which corresponds to a predicted (by simulations) harmonic of the trough around 1 kHz.
- **The measured velocity of the primary trough is greater than the one of the secondary one**. As expected, the outer trough moves slower than the inner trough. That observation suggests that the movement of both containers is propagating from the powder to the primary trough and then subsequently to the secondary. Therefore the possibility that the outer container causes the powder movement can be excluded.

The high-amplitude noise of unknown source and the lack of absolute beam stamp in the LDV data in order to exactly determine the beam arrival time, make the resolution of the propagation speed of a possible shock wave impossible. No conclusive evidence concerning the presence of such a wave exists, except from the indication provided by the aforementioned secondary disruptions inside the powder.

5 Theoretical Model

The results of the digital image analysis revealed that the sequence of physical phenomena that take place right after the beam impingement on the target are:

1. The beam deposits its energy on the target.
2. The temperature of the W-grains increases.
3. Thermal expansion of the grains starts.
4. The temperature of the surrounding gas increases due to heat transfer from the grains.
5. The surrounding gas starts to expand, dragging along the smallest (and more light) of the powder grains.

Processes (1-4) are completed before the movement of the grains starts, that is in $t \leq \sim 1ms$. The expansion of the gas continues until its pressure is completely relieved. We assume that the time that the increased gas pressure reaches the atmospheric pressure of the inner container, the gas stops expanding. At $t = t_c$, the expansion of the gas finishes; the observed grain (or cluster of grains) has detached from the rest of the powder and for $t \geq t_c$ follows a trajectory of a ”vertical projectile” in the He gas atmosphere of the container. This critical time (t_c) corresponds in most of the cases to ~10 ms after the beam impact.

Two theoretical models have been developed to describe the movements in these two time regimes. For reasons of simplicity and better presentation of the results, the second regime (t $\geq t_c$) will be presented first.

5.1 Second time regime: $t \geq t_c$

In this time regime, the movement of the powder grains in the He gas atmosphere of the inner container, can be described as the movement of a body in a continuous, viscous gas. Assuming spherical grains, a drag force is acting on the grains due to the gas viscosity. This force, known as the *Stokes drag force*, is equal to:

$$F_d = -6\pi R\eta \cdot u \tag{5.1}$$

where R is the radius of the grain, η is the dynamic viscosity of the gas, and u the speed of the grain. An illustration of the grain and the forces acting during its movement in the gas, is shown in Figure 5.1.

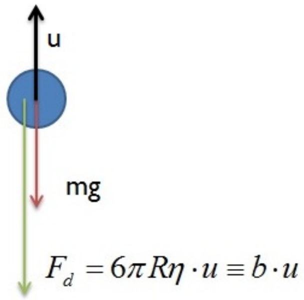

Figure 5.1: *The forces acting on the grain during its movement in the gas atmosphere, for $t \geq t_c$.*

Assigning for simplicity $b \equiv 6\pi R\eta$ for the Stokes drag force coefficients, the equation of motion of the grain becomes:

$$\frac{du}{dt} = -g - \frac{b}{m} \cdot u \tag{5.2}$$

Where m is the mass of the grain. Equation 5.2 is of the form $\frac{du}{dt} = au - b'$ the solution of which is :

$$u = \frac{b'}{a} + ce^{at} \tag{5.3}$$

Substituting in Equation 5.3 the values $a = -\frac{b}{m}$ and $b' = g$ along with defining the quantity $V_t \equiv \frac{mg}{b}$, and applying the initial condition $u(t = 0) = u_0$ the solution of the equation becomes:

$$u(t) = -V_t + (V_t + u_0) \cdot e^{-\frac{b}{m} \cdot t} \tag{5.4}$$

where V_t is the *terminal velocity* of the grains due to the friction of the gas. Integrating Equation 5.4 and applying the initial condition $y(t = 0) = 0$, we obtain the motion equation of the powder grains:

$$y(t) = -V_t \cdot t + (V_t + u_0)\frac{m}{b}(1 - e^{-\frac{b}{m} \cdot t}) \tag{5.5}$$

The limit of Equation 5.5 as b approaches zero is:

$$y(t) = u_0 t - \frac{1}{2}gt^2 \tag{5.6}$$

Equation 5.6 corresponds to the trajectory of a vertical projectile with an initial speed

u_0 in vacuum. We define the quantity:

$$\alpha = \frac{m}{b} = \frac{\rho V}{6\pi R\eta} = \frac{2\rho R^2}{9\eta} \tag{5.7}$$

and with an addition of a time-offset term t_0 allowing for the trigger jitter, Equation 5.5 becomes:

$$y(t) = \alpha g \cdot (t - t_0) + (ag + u_0) \cdot \alpha \cdot (1 - e^{-\frac{t-t_0}{a}}) \tag{5.8}$$

The data points corresponding to the height of the powder movement for all shots, were fitted with Equation 5.8 where α, u_0 and t_0 were treated by the algorithm as free fit parameters. A weighted fit was performed, in order to take into account the standard deviations of the data points given by the extraction algorithm. This way the error of the fit parameters was calculated. In all cases, the goodness of fit was very satisfactory, an example of the p-values given from several goodness of fit tests performed for shot #10 are shown in Table 5.1. It must be noted that the parameter u_0 calculated by the fitting algorithm using equation 5.5 corresponds to the value of the fit function for $t = 0$. This value has no physical meaning, since Equation 5.8 is only valid for $t \geq t_c$ and not at $t = 0$. The maximum powder speed u_0, defined at the moment $t = t_c$, when the expanding gas has accelerated the grains at their maximum speed, and they are simultaneously detached from the main powder body remaining in the trough, is calculated by the slope of the fitting curve at $t = t_c$.

Test name	Statistic Value	P-value data - fit agreement
Anderson - Darling	0.179473	0.99504
Cramer-von Mises	0.0342077	0.9990794
Kolmogorov - Smirnov	0.0930233	0.990794
Kuiper	0.286545	0.295776
Pearson Chi Square	7.03342	0.63364
Watson U^2	0.0237956	0.977406

Table 5.1: *The results of several goodness of fit tests, all of them using as null hypothesis that the data are in agreement with the fit equation, and alternative hypothesis that they are not. It can be seen that the p-value of the null hypothesis is very high in all cases - fact that confirms the good agreement of the data with the fit equation. The results of the goodness of fit tests were satisfying for all the shots of the experiment.*

An illustration of the importance of the gas friction to the powder movement can be found in Figure 5.2, along with the fitted data points corresponding to the powder height for shot #10.

A plot of the calculated *maximum speed*, u_0 at $t = t_c$ (given by the slope of the fitted curve) for all the shots with the beam at nominal position (up to shot #21 as is shown in Table 3.2)) is given in Figure 5.3, and a combined plot of the shots intensity and the measured maximum speed of the grains, showing the correlation of the two, can be found in Figure 5.4.

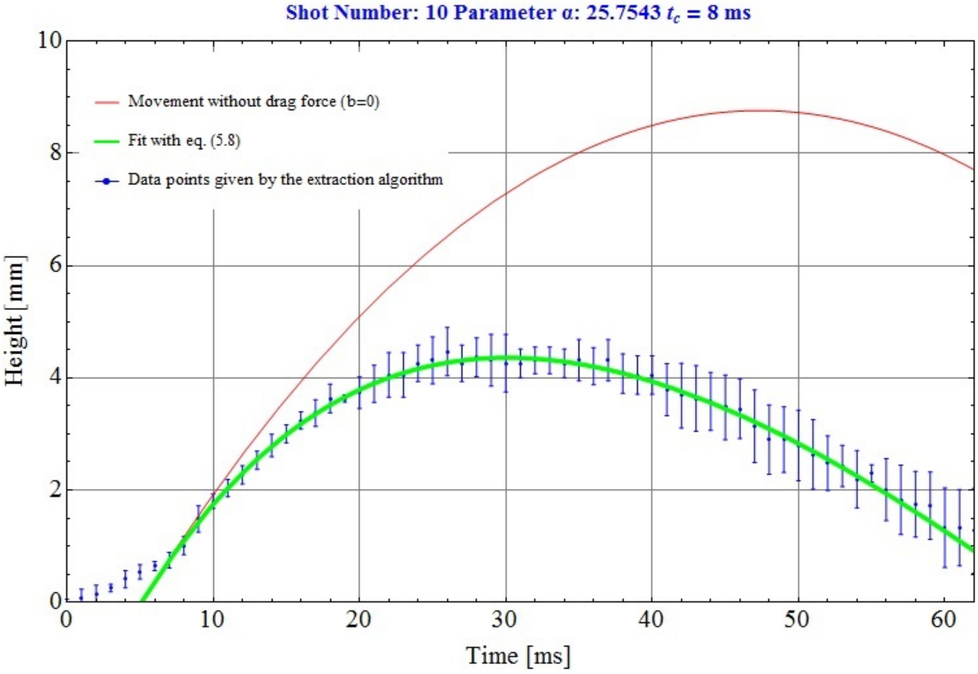

Figure 5.2: *An illustration of the importance of the drag force on the movement of the powder grains. The red curve illustrates the movement of the powder grains with the calculated initial speed from the slope of the fitted curve at $t = t_c$, if there was no friction from the gas. The green fit curve is projected to $t = 0$ for better visualization of the result.*

It is clear from Figure 5.3 that the maximum speed of the powder grains scales linearly with the beam intensity. In all cases, and for all three analysed stripes, the maximum measured speed does not exceed $1.5\ m/s$.

As defined in Equation 5.7, the free parameter α is a function of the powder density, the grain radius and the dynamic viscosity of the He gas, which for a temperature of 20 degrees has the value of $1.96 \times 10^{-5}\ \frac{kg}{m \cdot s}$, while the density of a tungsten grain is $19.3 \frac{g}{cm^3}$. Solving Equation 5.7 for R we obtain:

$$R = \sqrt{\frac{9\eta\alpha}{2\rho}} \tag{5.9}$$

Parameter α versus the grain radius is plotted in Figure 5.5, and the calculated radii for the three analyzed stripes are concentrated in Figure 5.6. The error bars of the radii are calculated through error propagation from the error given by the fit of the data with Equation 5.9 for parameter α. In all cases, the measured grains radii do not exceed 25 μm (or 50 μm diameter).

5.2 Initial Acceleration: $t \leq t_c$

As already discussed, in the time regime after the critical time t_c, the acting forces on the powder grains which define their movement are the gravity and the drag force due to the gas atmosphere of the inner container. However, it was observed that in the first

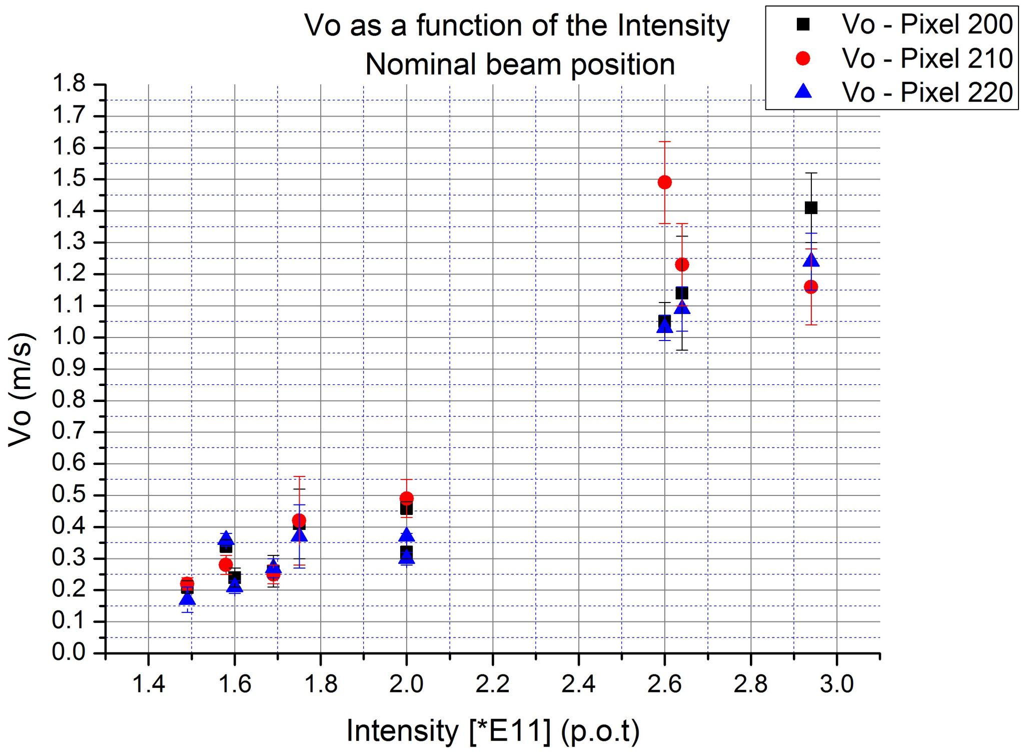

Figure 5.3: *The maximum velocity of the powder grains at* $t = t_c$ *for the three stripes used in the analysis, corresponding to a position of ~11* cm *from the target front.*

time regime ($t < t_c$), the slope of the measured data points corresponding to the vertical powder movement, is different from the slope of the data in the second regime. More specifically, the powder grains during the first milliseconds are *accelerated*.

Two physical phenomena can account for this observed acceleration of the powder grains:

1. The expansion of the helium gas due to the temperature/pressure increase and subsequent movement of the grains that enclose this expanding gas;

2. The thermal expansion of the tungsten grains due to the energy deposited from the beam.

5.2.1 Expansion of the He gas due to the temperature increase

The deposited energy from the primary beam directly to the gas is negligible compared with the energy deposited to the grains, due to the very small density of the gas ($1.7 \times 10^{-4}\ g/cm^3$). Therefore, any temperature increase of the gas is only due to heat transfer from the powder grains. FLUKA calculations of the target for an assumed proton pulse of 3×10^{11} protons showed a temperature increase of ~230 K for one tungsten grain of a radius 50 μm placed at the shower maximum.

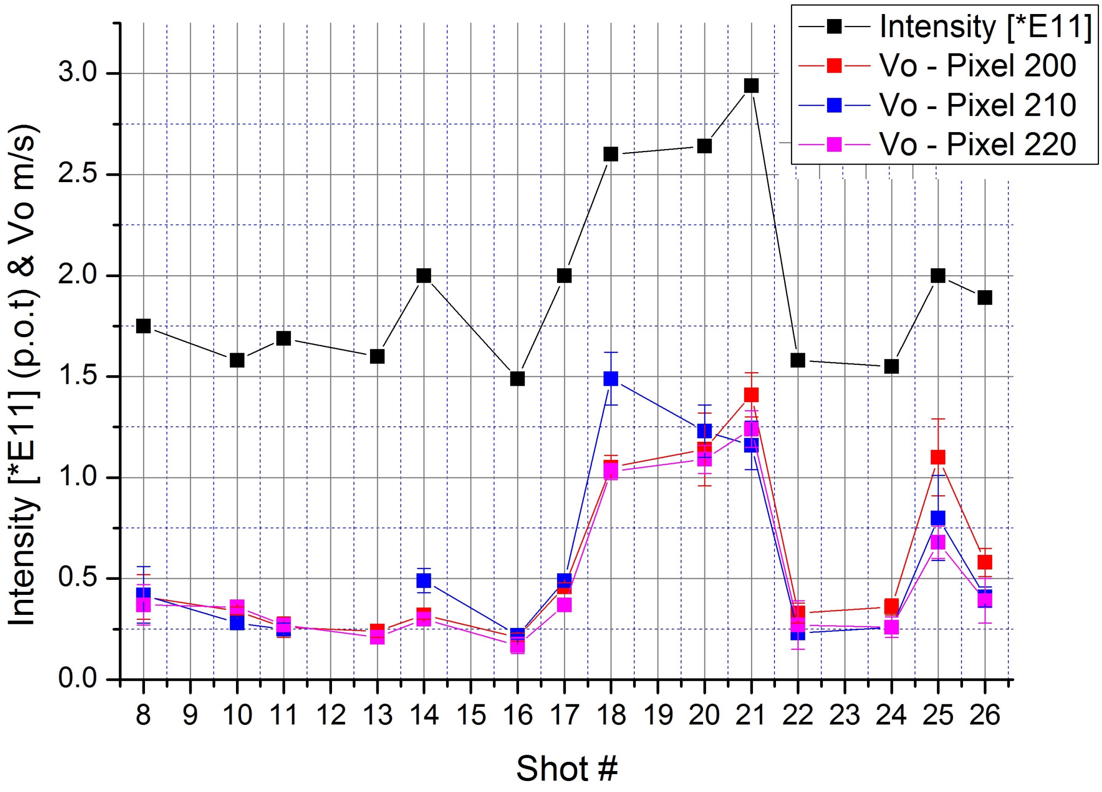

Figure 5.4: *The initial speed of the powder grains at $t = t_0$ for the three pixel stripes used in the analysis. It can be seen that the maximum speed is in direct correlation with the beam intensity.*

Taking into account the heat transfer by convection from the grains to the gas :

$$\dot{Q} = hA(T_f - T_a) \tag{5.10}$$

where h is the heat transfer coefficient, A the grain surface, T_f is the final temperature of the grain and T_a the ambient temperature of the convective gas. We assume a spherical grain with a radius of 50 μm, surrounded by a gas sphere with the same volume as the grain. Assuming that the temperature of the grain is instantaneosly increased by 230 K due to the energy deposition by the beam, from Equations 5.10 the time needed for the gas surrounding this ideal grain to reach at the same temperature with the grain can be calculated. A plot illustrating the temperature as a function of time for two different emissivity constants can be found in Figure 5.7.

It has to be noted that in the above calculation the contribution of many neighboring grains to the heating of the same gas volume has not been taken into account. Therefore, the actual time needed for a very small volume of gas getting heated by many grains simultaneously could be even less. At any case the time needed for the heat transfer from the grains to the surrounding gas is not longer than 1-2 ms.

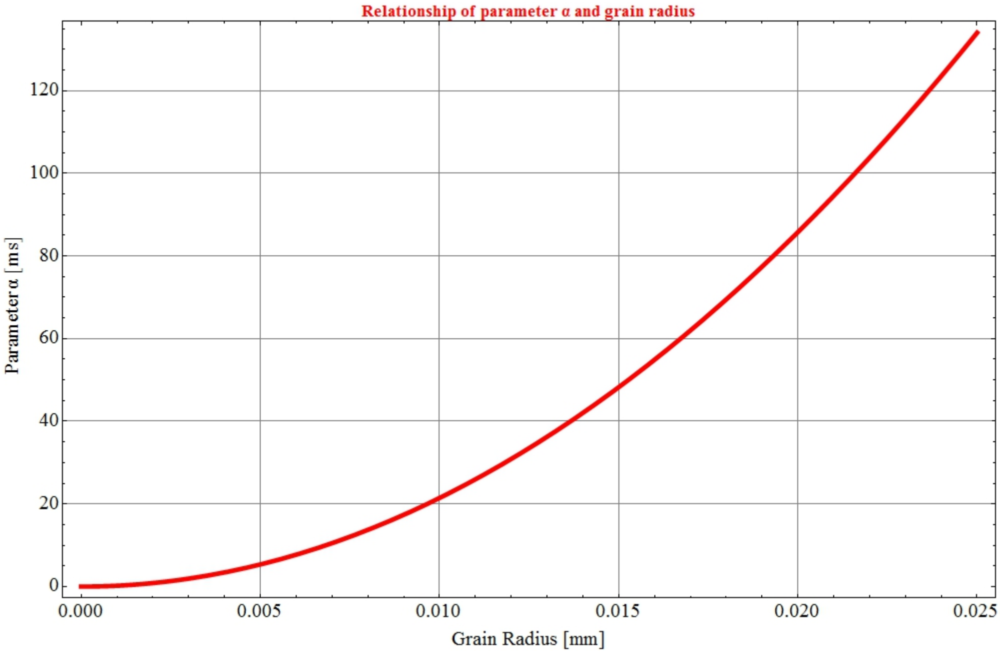

Figure 5.5: *The relationship between the free fit parameter α and the grain radius, based on equations 5.7 and 5.9.*

5.2.2 Thermal expansion of the W-grains

Thermal Expansion of metals due to temperature increase has been extensively studied in the literature [66]. When the temperature changes by ΔT, the length of a rod of initial length L will change by ΔL :

$$\Delta L = \alpha L \Delta T \tag{5.11}$$

where α, the *coefficient of linear expansion*, is the ratio of the fractional change in length to the change in temperature:

$$\alpha = \frac{\Delta L / L}{\Delta T} \tag{5.12}$$

Tungsten has the lowest coefficient of thermal expansion of any pure metal, equal to $4.5\mu m \cdot m^{-1} \cdot K^{-1}$, being therefore relatively robust in terms of thermal expansion. However, the effect of the grain expansion can be expressed through an initial thermal expansion speed u_{exp} which appears instantaneously with the beam, and has an effect on the grains' movement.

Denoting the constant speed of the expanding gas with u_{gas}, the forces acting on the grain in the time regime $t \leq t_c$ are (a) the gravity and (b) the drag force due to its movement in the friction gas field, where the total drag force acting on the grain from the gas is denoted by:

$$F = b(u_{gas} - u) \tag{5.13}$$

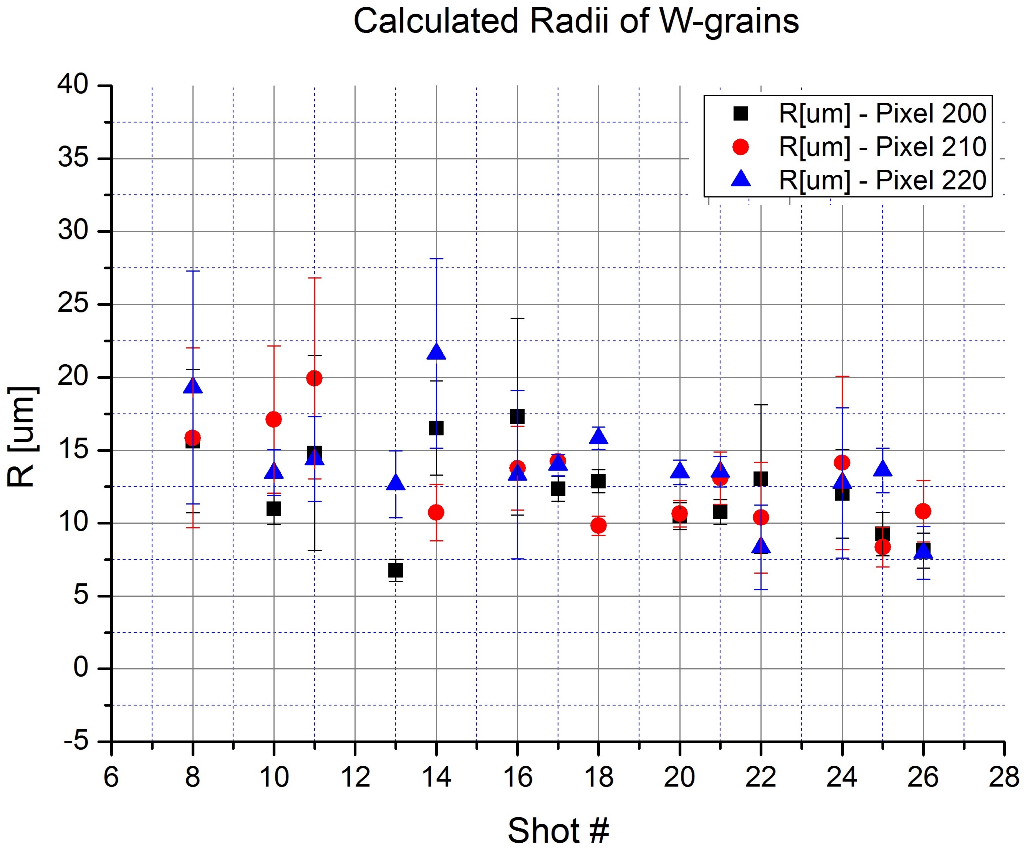

Figure 5.6: *The calculated radii of the tungsten grains under disruption, for the three vertical stripes used in the analysis, for all the shots of the experiment. At shots # 22, # 24, # 25 and # 26, the beam was impinging 4* mm *below the powder free surface. The error bars are calculated through error propagation of the errors given by the fit of the data with Equation 5.9.*

Where $b = 6\pi\eta R$ is the drag coefficient.

An illustration of the grain and the forces contributing to its movement can be seen in Figure 5.8.

The equation of motion of the grain is :

$$\frac{du}{dt} = -\frac{b}{m}u + \frac{b}{m}u_{gas} - g \tag{5.14}$$

Since the thermal expansion takes place instantaneously, we can assume a constant initial speed of the grains to be equal to the thermal expansion speed :

$$u_0 = u_{exp}$$

Integrating the solution of Equation 5.14 applying the initial condition $y_0(t = 0) = 0$ the vertical position of the powder as a function of time for this time regime where $t \leq t_c$

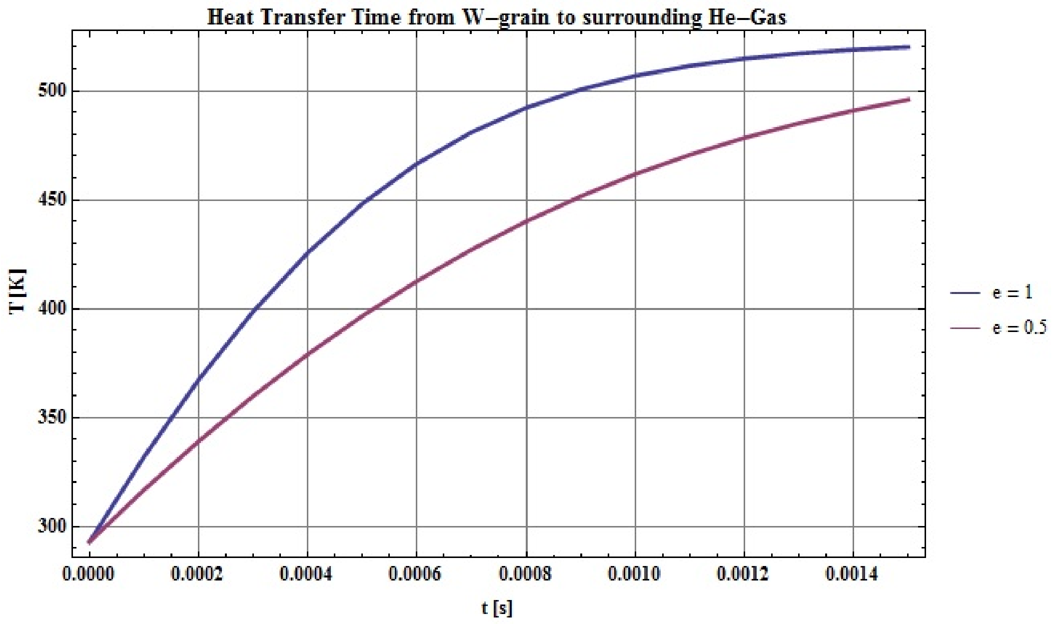

Figure 5.7: *The time needed for the surrounding gas of a W-grain with a radius of* 50 μm *to reach a temperature of* 523 *K through radiative and convective heat transfer, using Equations 5.10 and assuming the heat transfer coefficient between iron and air. Two emissivity factors are studied. The time needed in both cases is less than* 2 ms.

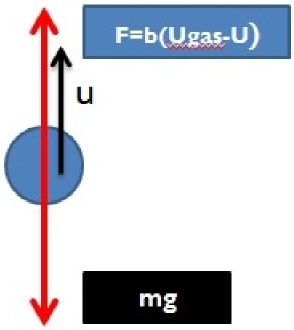

Figure 5.8: *The forces acting on the grain during its movement in the gas atmosphere, for* $t \leq t_c$

.

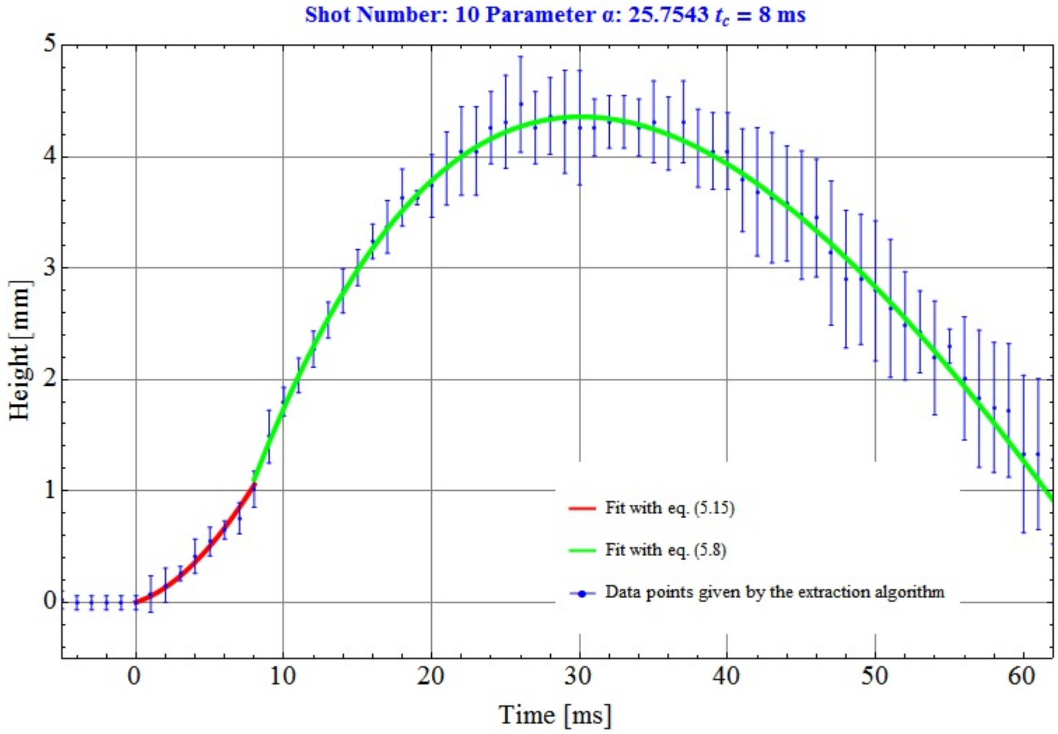

Figure 5.9: *An example of the result of the fitting algorithms for shot #10. The red line denotes the fit for the regime* $t \leq t_c$*, while the green line denotes the fit for the regime* $t \geq t_c$*. For this specific example, the speed of the gas,* u_{gas} *was calculated to be* 0.93 ± 0.2 m/s.

is:

$$y_0(t) = (-\frac{gm}{b} + u_{gas}) \cdot t + \frac{m(\frac{mg}{b} - u_{gas} + u_{exp})}{b} - \frac{e^{-\frac{bt}{m}} m(\frac{mg}{b} - u_{gas} + u_{exp})}{b} \tag{5.15}$$

The extracted data were fitted with Equation 5.15 where u_{gas} and u_{exp} were treated as free fit parameters. The value of parameter $\alpha = \frac{m}{b}$ was taken from the fit algorithm of the second regime (previously described). As with the data for $t \geq t_c$, a weighted fit was performed in order to take into account the standard deviations of the data points given by the extraction algorithm. An example of the fitted data points (for the first and the second regime) for shot #10 can be seen in Figure 5.9.

5.3 Speed of the expanding gas

For reasons of simplicity, in the theoretical model of the first time regime ($t \leq t_c$) it is assumed that the gas expands with a constant speed, u_{gas}. In Figure 5.10 the expanding gas speed is illustrated as a function of the pulse intensity.

As can be seen from Figure 5.10, the estimated gas speed is within the range of $0 - 6$ m/s. The error bars, corresponding to the error of the fit algorithm are increased com-

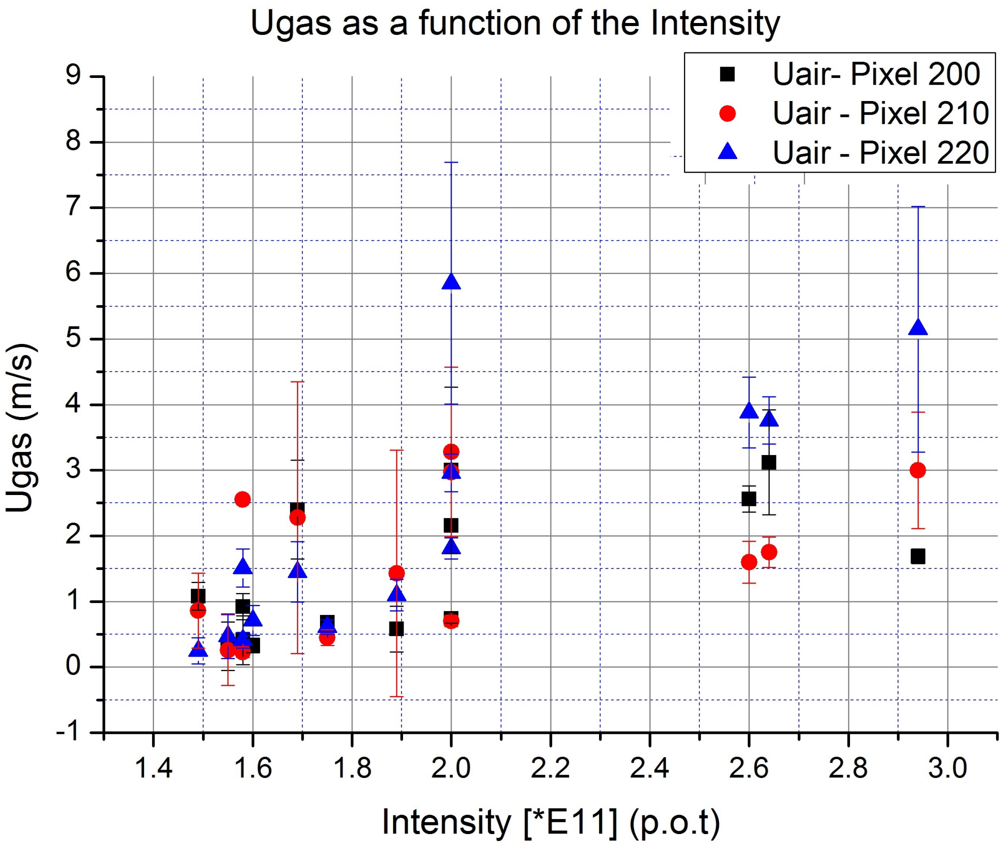

Figure 5.10: *The calculated speed of the expanding gas. No significant differences appear between the three horizontal pixels chosen, and in all cases the speed of the expanding gas is calculated between 0.1 and 6 m/s.*

pared with the error bars of the initial velocity, due to the lack of data points concerning this time regime.

5.4 Higher beam position

After shot # 21, and for the last four shots, the beam position was moved up by 2 mm, that is 4 mm below the tungsten free surface. The grain velocity measured in this case, as a function of the beam intensity is plotted in Figure 5.11.

As in the case when the beam was impinging 6 mm below the powder free surface, the measured maximum speed of the grains appears to be scaling linearly with the pulse intensity. Therefore the higher beam position does not play significant role in the scaling of the maximum grain speed with the beam intensity. Additionally, the velocities measured remain in the same order of magnitude as in the nominal beam position.

5.5 Post-Irradiation observation

After 6 months of cooling time the calculated dose rate in contact with the outer container of the experimental apparatus was negligible, fact which was confirmed by mea-

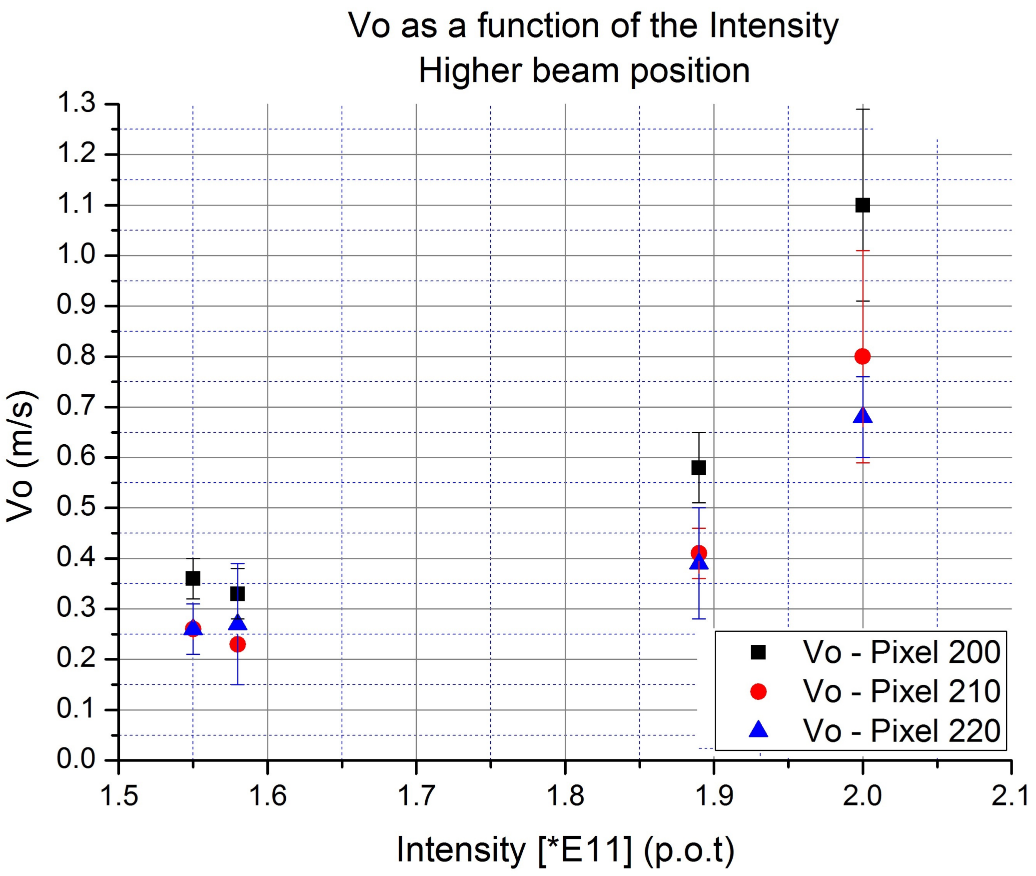

Figure 5.11: *The maximum velocity of the powder grains for $t = t_c$, for the three vertical stripes used in the analysis, for the last 4 shots at a higher beam position than before.*

surements by the CERN RP service. However, as predicted by the simulations, the target itself was slightly radioactive and the danger of the escape of activated powder grains in the atmosphere was significant. Therefore, with the purpose of a post-irradiation observation of the target, it was decided to dismantle and open the outer container keeping the inner one closed. High quality photos were taken from several angles in order to observe the amount of powder fallen outside of the trough, as well any visible effect of the proton beam on the powder surface. In Figure 5.12, a post irradiation photo of the target can be seen.

From Figure 5.12 it can be observed that the target was displaced symmetrically on both sides of the container, and now traces of powder can be found on the trough sides (where before the experiment the powder was carefully installed only inside the inner trough. See Figure 3.12). However, this bilateral displacement seems to be of a small amplitude, since only a small amount of powder was found on the bottom of the inner container. Comparably small amount of powder seems to have been displaced and fallen beyond the upstream end of the target (Figure 5.13).

A zoom on the disrupted powder's surface can be found in Figure 5.14. A "trench",

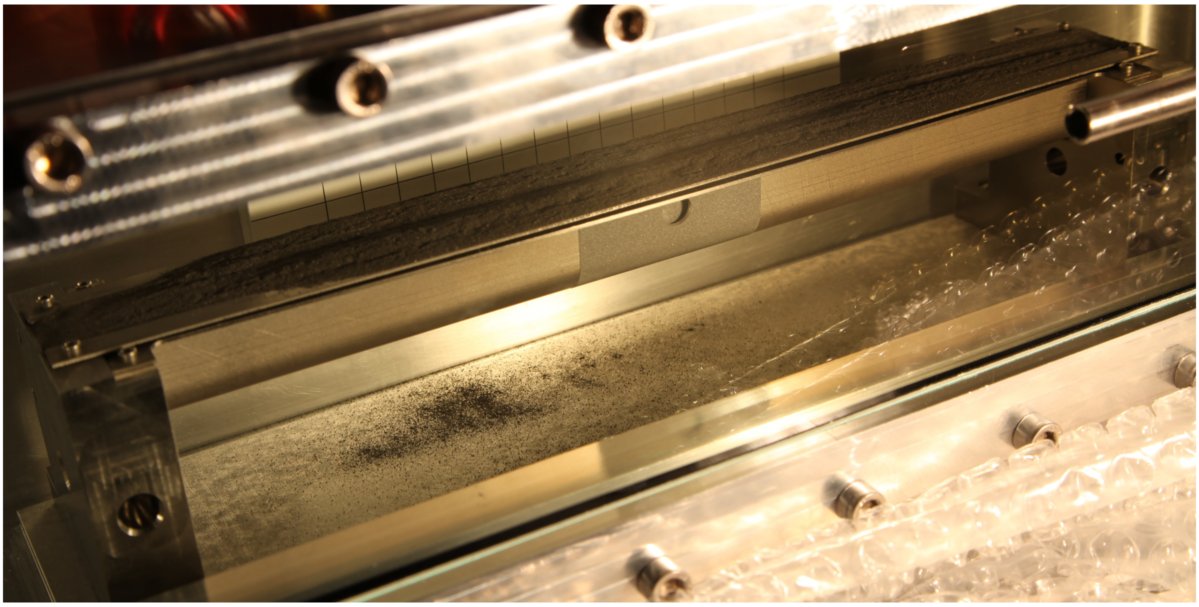

Figure 5.12: *A photo of the target trough after the irradiation. A bilateral displacement of the powder can be observed. However, the total amount of powder fallen out of the double trough system is very small.*

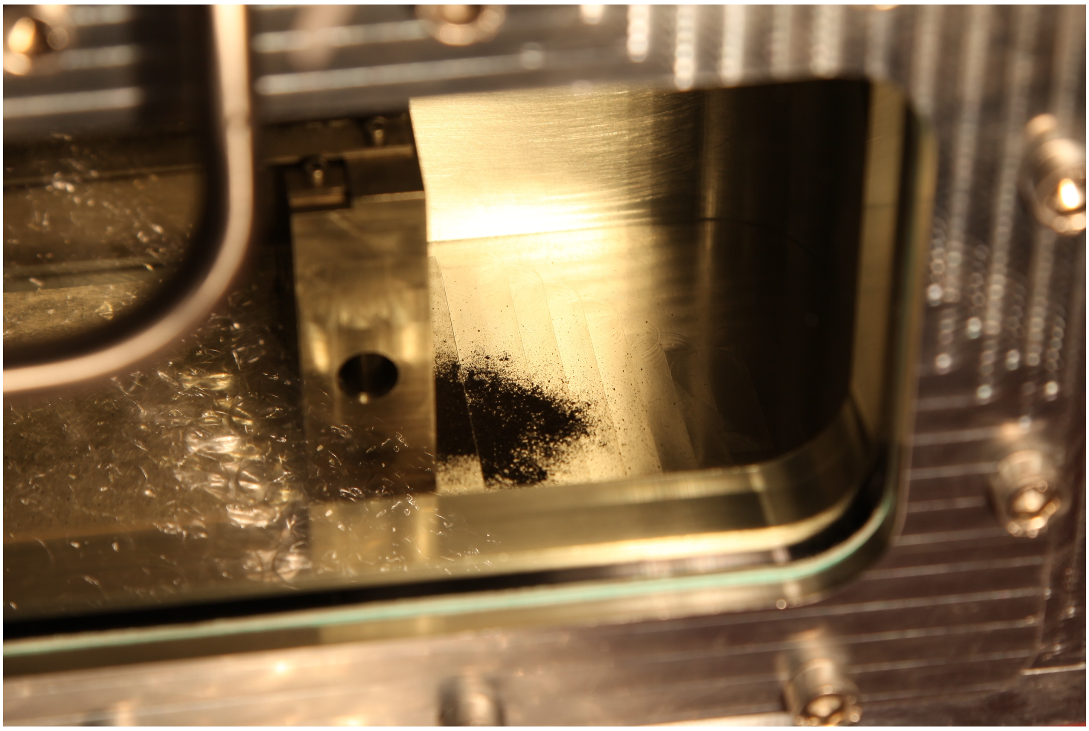

Figure 5.13: *A small amount of powder was found to have fallen in the forward direction, after the upstream end of the target.*

of approximate estimated depth of 2 mm and width of 5 mm was observed at the center of the target. The existence of this trench suggests that only the amount of powder at the center of the trough was disrupted and therefore displaced. The rest of the powder seems not to have suffered any displacement. The existence of this trench around the beam impact point and the absence of a homogeneous disruption of the powder surface suggests that, even if a pressure wave was present due to the beam, its magnitude was not big enough to disrupt a larger amount of tungsten powder.

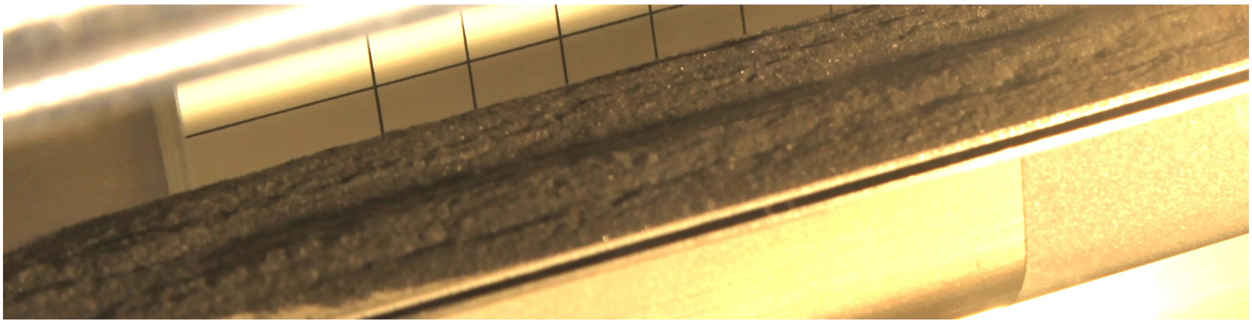

Figure 5.14: *Zoom on the disrupted powder's surface.*

6 Summary & Discussion

6.1 Summary

The HRMT-10 experiment allowed the investigation of the physical laws that dominate the interaction of a granular target with a high-energy proton beam. A disruption of the tungsten powder grains was observed after the beam impact on the target. The maximum measured disruption velocity of 1.5 m/s was observed for a proton beam intensity of 2.6 $\times 10^{11}$ protons per pulse. The maximum grain velocity scales with the beam intensity for both vertical beam positions (Figures 5.3 and 5.11). The first significant disruption was observed after a proton intensity of 1.75×10^{11} protons and a beam spot size of about 1.87 mm^2. Moreover, the diameters of the disrupted grains were measured to be less than 50 μm (Figure 5.6), a size corresponding to the center of the measured grain size distribution (Figure 3.5). The time evolution of the disruption and the maximum height of the disrupted powder also scale with the beam intensity (Figures 4.12 and 4.11)). The speed of the expanding gas has been also calculated to be less than 10 m/s in all cases (Figure 5.10). Additionally, it was confirmed that the observed movement of the powder grains is due to the impact of the beam, and not due to the movement of the containers. The post-irradiation analysis of the target confirms that the disruption was not very violent, since only a very small amount of powder was found outside the troughs.

The maximum intensity shot on target during the HRMT-10 experiment was 2.94×10^{11} protons. Assuming that the observed linear relation between the maximum grain speed and the beam intensity holds for higher intensities, and extrapolation can be made to estimate the response of such a target to a neutrino factory pulse.

6.2 Extrapolation to Neutrino Factory parameters

The neutrino factory baseline proposes a 4 MW proton beam impinging on a mercury target, with a repetition rate of 50 Hz. This beam power corresponds to a pulse intensity of 6.25×10^{13} protons with an energy of 8 GeV. As already explained in section 3.3.2 and shown in Figure 3.3, the maximum deposited energy per gram on mercury after such a pulse is equal to 200 J/g. During the HRMT-10 experiment, the maximum deposited energy for each pulse was calculated and shown in Figure 6.1 as a function of the maximum grain speed measured in each shot. Applying a linear fit to the three speed datasets corresponding to the three vertical stripes, and extrapolating their average for ~1 order of magnitude (200 J/g), the estimated maximum grain speed caused by a neutrino factory equivalent pulse on tungsten powder can be obtained. The results are shown in Figure 6.2. It can be seen that the expected maximum speed of the grains in case of a neutrino factory equivalent pulse depositing on target 200 J/g, does not exceed 30 m/s.

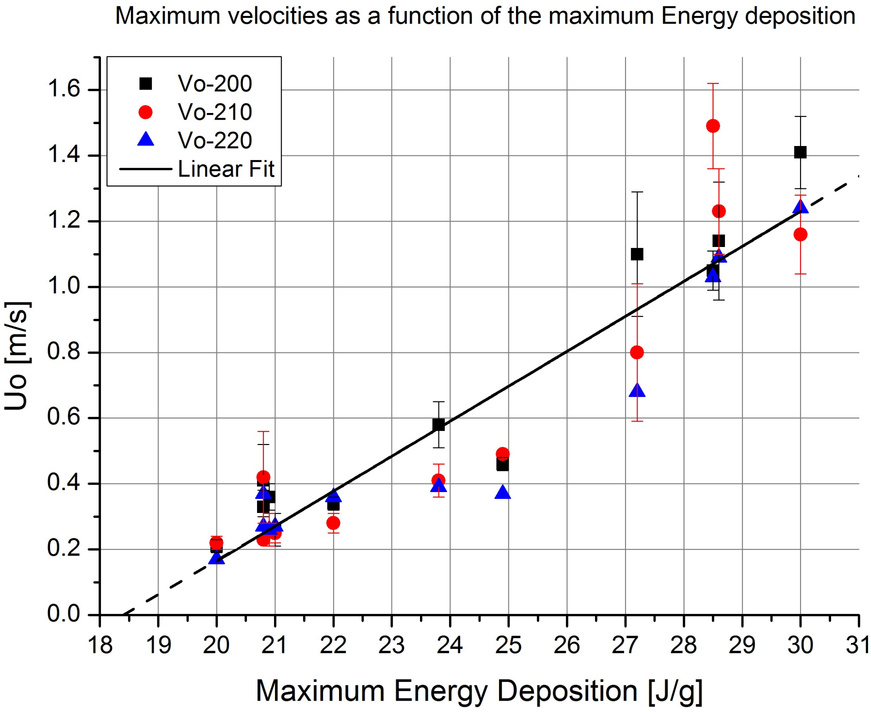

Figure 6.1: *The maximum deposited energy for all the pulses of HRMT-10 experiment. The maximum deposited energy is 30 J/g for* 2.94×10^{11} *protons on target.*

6.3 Discussion

Several studies [68, 69] have shown that erosion on metal or glass surfaces from metallic granular materials becomes significant only when the speed of the incident grains is greater than 100 m/s. This speed value is greater by at least a factor of 3 compared to the extrapolated speed of the grains of 30 m/s predicted for a neutrino factory pulse. This very low speed of the W-grains is an encouraging indication for the stability of a future target container.

Additionally, the maximum temperature increase of the powder grains for a pulse of 3.74×10^{12} p.o.t does not exceed 2000 K (Figure 3.4). Since the melting point of tungsten is 3695 K, the danger of the melting of the target after a single neutrino factory pulse can be excluded.

The pneumatic conveyance of tungsten powder has been demonstrated for speeds

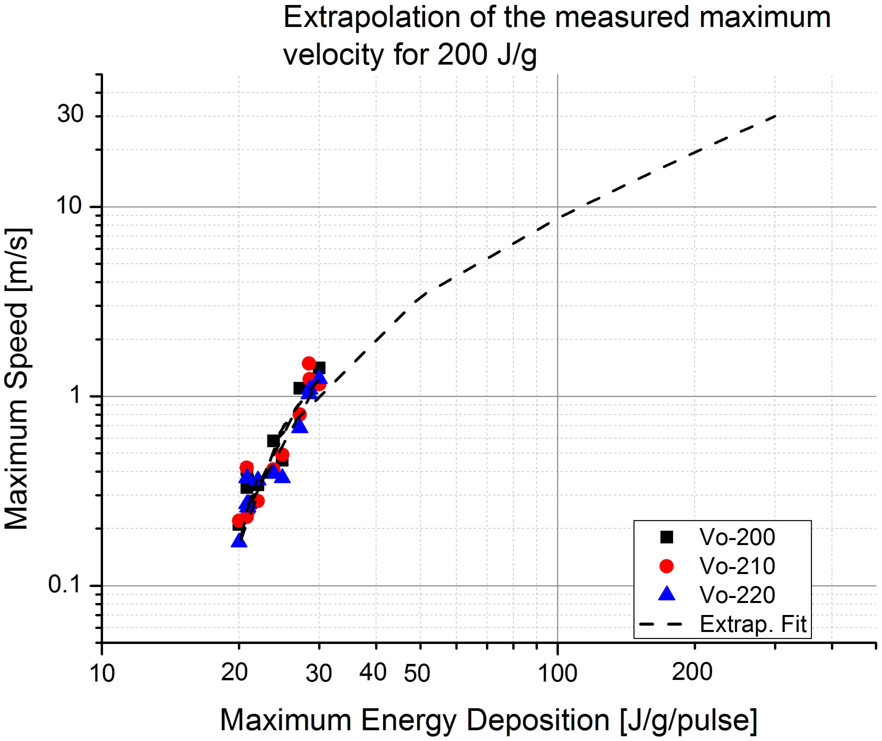

Figure 6.2: *Extrapolation of the measured maximum grains velocity for* 3.74×10^{12} *p.o.t, pulse intensity corresponding to a neutrino factory. The dashed line corresponds to the average linear fit of the experimental data extrapolated for one order of magnitude higher.*

up to 10 m/s, and powder has shown excellent flowability. In addition, the pion yield for a 10 GeV proton beam on tungsten powder has been shown not to be very different from the one of liquid mercury [70]. However, the implementation details of such a target station must be more carefully studied. For example, the possible erosion effects of the target container due to the conveyance must be minimized. Also, the heat-transfer capability of such a system must be carefully studied.

6.4 Future Work

The HRMT-10 experiment was the first step in investigating the complex behavior of a granular material under the impact of a high-energetic proton beam. This field is, until today, highly unexplored. Some of the effects observed during the experiment however, still remain unexplained. For example, the nature of the observed secondary disruptions; the exact cause of the filaments (for example shots #8 and #9); the existence or not of a shock wave. In general, further research is needed in order to better understand the exact physical mechanisms that drive the dynamics of a granular target under the effect of the beam impact. A future experiment must be planned into which the free surface of the target will be visible during the beam impact. This will allow the evaluation of a possible shock wave propagating inside the powder volume. Additionally, since the diameters of the disrupted grains are measured to be less than 50 μm, then it is possible that if the grain size distribution of the target is larger by approximately a factor of 2, then no disruption may occur. Replacing the carrier gas with vacuum would also be very interesting, since it would allow to observe the physical phenomena taking place only due to the beam-grains interaction, without the gas expansion. After these experiments, an even more detailed theoretical model predicting the behavior of tungsten grains under the effect of the beam could be developed and evaluated.

In conclusion, HRMT-10 was the first experiment to investigate the behavior of a granular material under the effect of a high-power beam, and allowed the observation of the physical phenomena that take place in such an interaction for the first time. The results of the experiment were quite encouraging, and tungsten powder definitely merits further investigation concerning its feasibility as a high-power target.

A The movement of the powder as a function of time

In this appendix, the movement of the powder for vertical stripe located near the horizontal pixel #200 can be found, for all the shots of the experiment, with the exception of shot #9, which due to the extreme filamentation could not be analyzed.

In shots #1, #2, #4, #5, and #6 no movement of the powder was observed, while in shots #3, #15, #19 and #23 no beam was extracted on target. The error bars correspond to the deviation between the six chosen thresholds, which in most of the cases are bigger during the powder descent. In shots #10, #11, #12 and #13, the secondary disruptions can be seen occuring after the stagnation of the powder from the main disruption.

The change of slope near $t_c = {\sim}10\ ms$, which denotes the end of the acceleration, is more obvious in the shots with higher intensity. Comments for specific shots can be found in the captions.

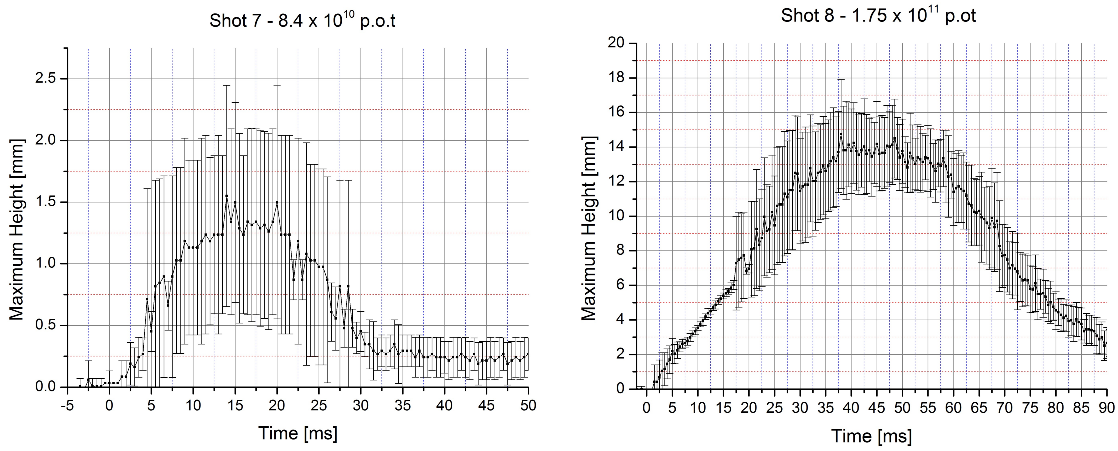

(a) *Shot #7. The first observed disruption of powder. The error bars are very big due to the very slight movement of the powder (maximum powder height < 1.5 mm.)*

(b) *Shot #8. The first major disruption of powder. As discussed in the data analysis chapter, the powder is moving homogeneously up to 20 ms, without filaments, while afterwards filaments are created.*

Figure A.1: *Shots #7 and #8*

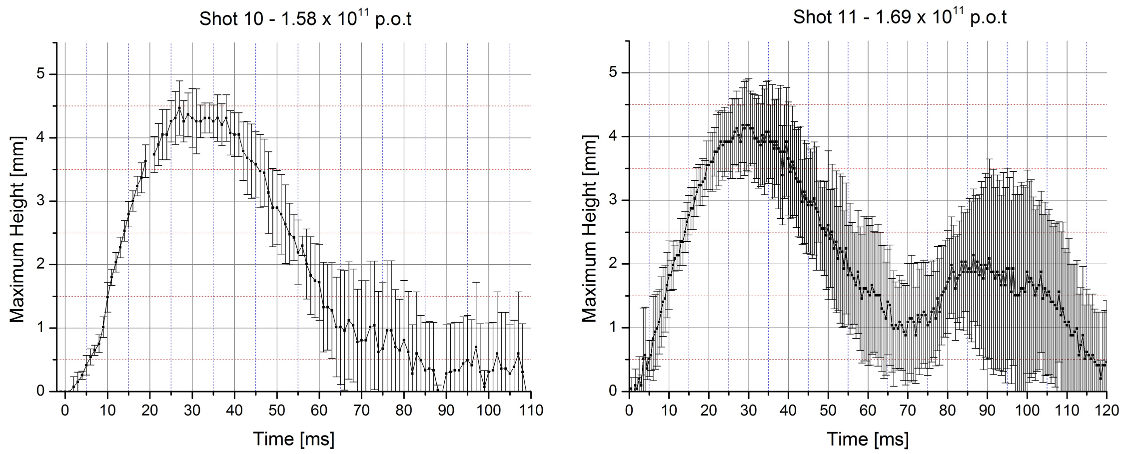

(a) *Shot #10. The secondary disruptions appear for first site at $t = \sim 90\ ms$*

(b) *Shot #11. Secondary disruptions appear also in this shot.*

Figure A.2: *Shots #10 and #11*

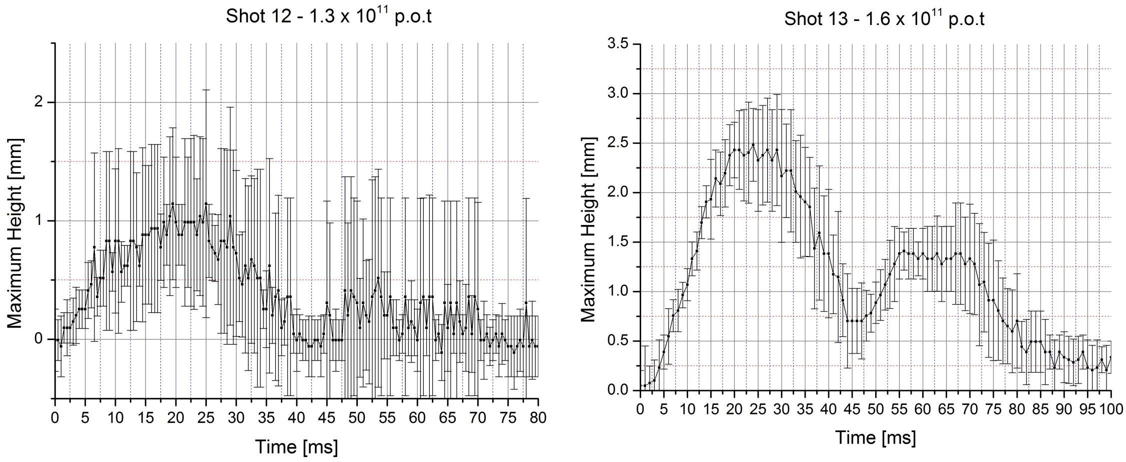

(a) *Shot #12. The disruption in this shot was slight. However, a secondary disruption appears also in this shot.*

(b) *Shot #13. Secondary disruptions appear also in this shot, this time at* $t = \sim 50$*. The height of the secondary disruption does not exceed* $1.5\ mm$*.*

Figure A.3: *Shots #12 and #13*

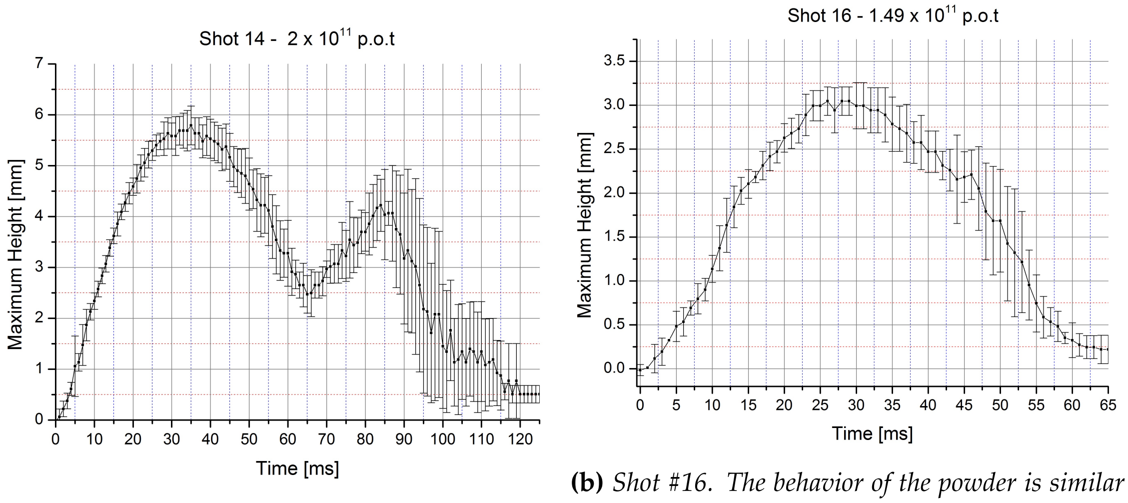

(a) *Shot #14. The last shot into which a secondary disruption was observed.*

(b) *Shot #16. The behavior of the powder is similar in terms of duration with shot #10. No secondary disruption appeared in this shot.*

Figure A.4: *Shots #14 and #16*

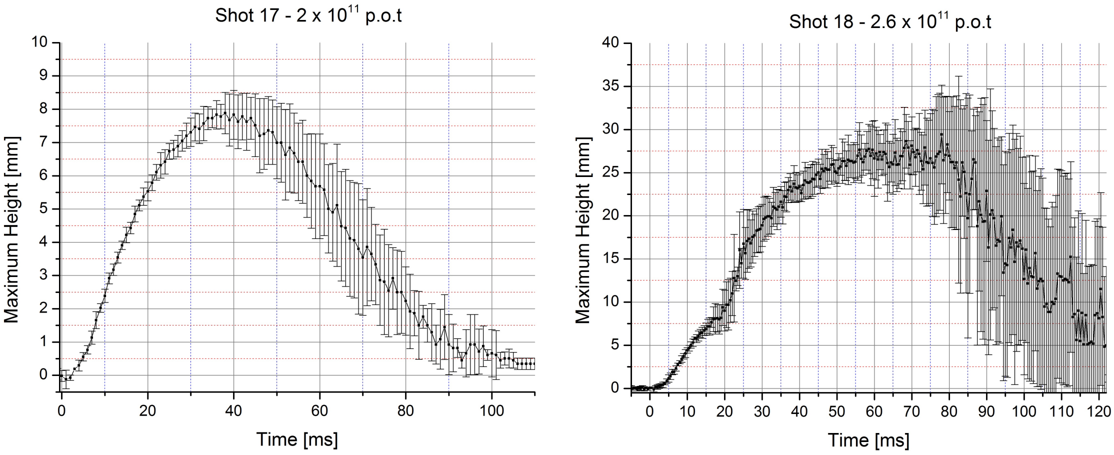

(a) *Shot #17. Even this shot has the same intensity as shot #14, the maximum height in this case is bigger. This behavior can be explained by the difference in the spot size between the two shots. Also, even that the two shots had the same intensity, no secondary disruption appeared in shot #17.*

(b) *Shot #18. This shot had one of the higher intensities of the experiment. The disruption is quite violent, and the powder height is near to the maximum. During the descent of the powder, the error bars are bigger due to the difference in the observed powder's density, caused by the difference on the grain sizes.*

Figure A.5: *Shots #17 and #18*

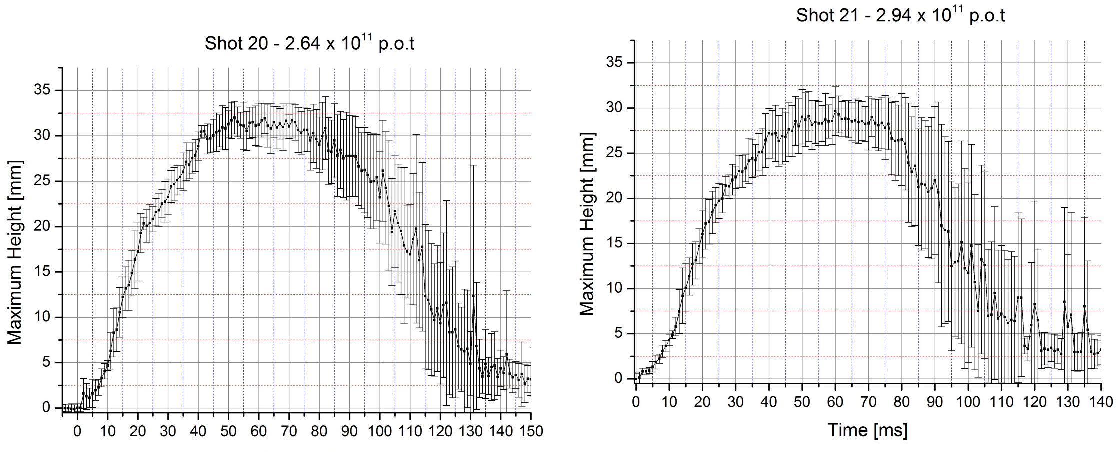

(a) *Shot #20. This shot had the penultimate intensity of the experiment. The disruption lasts* ~ *120* ms.

(b) *Shot #21. The shot with the maximum intensity of the experiment. The powder needs ~120* ms *to fully stagnate.*

Figure A.6: *Shots #20 and #21*

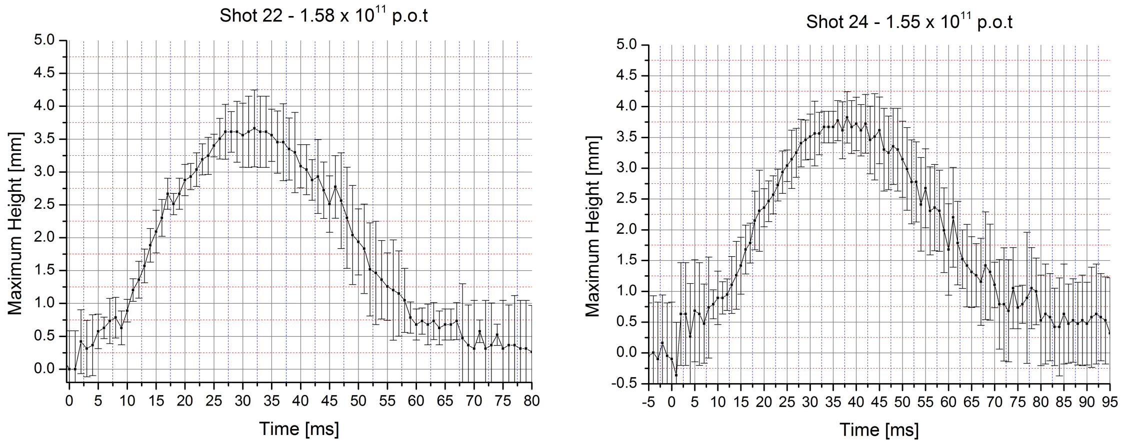

(a) *Shot #22. This was the first shot with the beam shot in a higher beam position (4 mm from the surface).*

(b) *Shot #24. Similar behavior with #10. The different beam position appears to have no effect on the powder disruption.*

Figure A.7: *Shots #22 and #24*

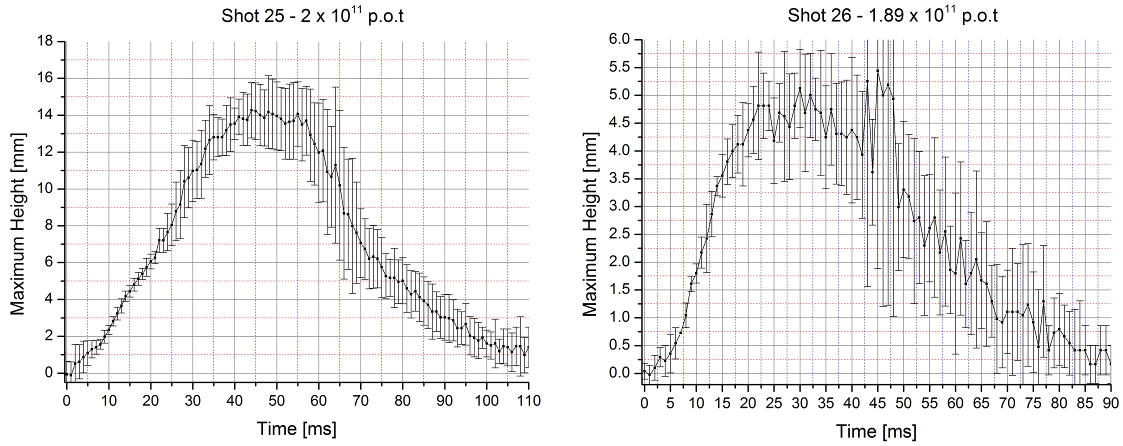

(a) *Shot #25.*

(b) *Shot #26.*

Figure A.8: *Shots #25 and #26*

Bibliography

[1] P. Sievers, *Elastic Stress Waves in Matter Due to Rapid Heating by an Intense High-Energy Particle Beam*, CERN-Lab-2-BT-74-2.

[2] W. Kalbreier, W.C. Middelkoop, P. Sievers, *Heating and Cooling of External Targets at the SPS*, CERN-LAB-2-BT-INT-73-2

[3] S. Timoshenko, J.N. Goodier, *Theory of Elasticity*, McGraw-Hill Book Company, 1951.

[4] H. Bargmann, *Dynamic Response of External Targets Under Thermal Shock*, CERN-LAB-2-BT-INT-73-3.

[5] R. Avery et al, *Shattering Rock With Intense Bursts of Energetic Electrons*, Proceedings IEEE, PAC 1973

[6] A. Bertarelli, V. Boccone, F. Carra, F. Cerutti, A. Dallochio, N. Mariani, *Limits for Beam Induced Damage: Reckless or too cautious?*, Proceedings of Chamonix 2011 Workshop on LHC performance, Chamonix, Switzerland, 2011.

[7] F. Perez, M. Al-Haik, *Analysis of elastic stress wave propagation through a complex composite structure*, Int.J. Theoretical and Applied Multiscale Mechanics, Vol.1, No.2, 2009.

[8] J.A.Zukas, *Introduction to Hydrocodes*, Elsevier, 2004, ISBN: 0-08-044348-6

[9] A. Bertarelli, E. Berthome, V. Boccone, F. Carra, F. Cerutti, A. Dallochio, S.D.M Dos Sandos, P. Francon, L. Gentini, M.Guinchard, N. Mariani, A. Masi, P. Moyret & S. Redaelli, *High Energy Tests of Advanced Materials for Beam Intercepting Devices at HiRadMat Facility*, 52nd ICFA Advanced Beam Dynamics Workshop Proceedings, September 17-21, 2012, Reference: MOP241

[10] A. Bertarelli, E. Berthome, F. Cerutti, N. Charitonidis, C. Charrondiere, A. Dallocchio, P. Fernandes Carmona, P. Francon, L. Gentini, M. Guinchard, N. Mariani, A. Masi, S. D Marques Dos Sandos, P. Moyret, L. Peroni, S. Redaelli, M. Scapin, *An Experiment to Test Advanced Materials Impacted by Intense Proton Pulses at CERN HiRadMat Facility*, CERN-ATS-2013-005

[11] P. Collier, B. Goddard, R. Jung, K.H. Hissler, T. Linnecar, F. Ruggiero, W. Scandale, K. Schindl, G. Schroder, E. Shaposhnikova, L. Vos, *The SPS as Injector for LHC Conceptual Design*, CERN-SL-97-07 DI

[12] O. Bruning, P. Collier, P. Lebrun, S. Myers, R. Ostojic, J. Poole & P. Proudlock, *LHC Design Report*, CERN-2004-003-V-1

[13] D. Autiero, I. Efthymiopoulos, A. Ferrari, E. Gschwendtner, A. Gugliemi, J. Lettry, A. Pardons, F. Piedropaolo, C. Rubbia, P.R. Sala, L. Sarchiapone, H. Vincke, *CNGS neutrino beam for long base-line experiments: present status and perspectives*, Nucl. Physics B (Proc. Suppl), 189 (2009), 263-270.

[14] J. Scott Bert et al, *The International Design Study for the Neutrino Factory*, IDS-NF Contribution to the 54th ICFA Beam Dynamics Newsletter, 2011

[15] A. Bertarelli, O. Aberle, H. Braun, M. Brugger, H. Burkhardt, S. Calatroni, F. Caspers, E. Chiaveri, A. Dallochio, B.Dehning, A. Ferrari, M. Gasior, A. Grudiev, E.B. Holzer, J.B Jeanneret, J.M Jimenez, Y. Kadi, R. Losito, M. Magistris, A. Masi, M. Mayer, E. Metral, R. Perret, C. Rathjen, S. Redaelli, G. Robert-Demoliaze, S. Roesler, M. Santana, D. Schulte, P. Sievers, K. Tsoulou, H. Vincke, V. Vlachoudis, J. Wenninger, I. Baishev, I. Kurochkin & G. Spiezia, *LHC Collimation: Design and Results from Prototyping and Beam Tests*, Proceedings of 2005 Particle Accelerator Conference, Knoxville, Tennessee

[16] J. Lettry, G. Arnau, M. Benedikt, S. Gilardoni, R. Catherall, U. Georg, G. Cyvogt, A. Fabich, O. Jonsson, H. Ravn & S. Sgobba, *Effects of thermal shocks on the release of radioisotopes and on molten metal target vessels*, Nucl. Instruments and Methods in Physics Research B 204 (2003) 251-256

[17] I. Efthymiopoulos, A. Fabich, H.G.Kirk, T. Tsang, F. Haug, J. Lettry, M. Palm, H. Pereira, N. Mokhov, S. Striganov, A.J. Carroll, V.B Graves, P.T Spampinato, K.T. McDonald, J.R.J Bennett, O. Caretta, P. Loveridge & H. Park, *The MERIT (nTOF-11) High Intensity Liquid Mercury Target Experiment at the CERN PS*.Proceedings of EPAC08, Genoa, Italy, Reference: WEPP169

[18] A. Fabich, *High Power Proton Beam Shocks and Magnetohydrodynamics in a Mercury Jet Target for a Neutrino Factory*, PhD Thesis, CERN-THESIS-2002-038

[19] H. Kirk et al. Target studies with BNL E951 at the AGS. proceedings PAC-01, Chicago, 2011.

[20] G. Acquistapace, V. Falaleev, J.M. Maugain, G. Olesen, S. Rangod and J. Zaslavsky *The West Area Neutrino Facility for CHORUS and NOMAD experiments (94-97 operation)*, CERN-ECP-95-14, 31 July 95.

[21] E. Heijne *CERN Yellow Report*, 83-06.

[22] C. Hessler, B. Goddard, M. Meddahi, *The Final Beam Line Design For the HiRadMat Test Facility*, Proceedings of IPAC 10, Kyoto, Japan, Reference: THPEB029.

[23] C. Hessler, M. Arruat, J. Bauche, K. Bestmann, J. Blanco Sancho, N. Conan, K. Cornelis, I. Efthymiopoulos, H. Gaillard, B. Goddard, D. Grenier, G. Gros, A. Habert, L. Jensen, V. Kain, G. Le Godec, M. Meddahi, S. Pelletier, P. Pepinster, B. Puccio, C. Theis, P. Trilhe, G. Vandoni, J. Wenninger, *Results from the HiRadMat Primary Beam Line Commissioning*, Proceedings of IPAC11, San Sebastián, Spain

[24] S. Evrard, M. Picard, *HiRadMat safety file – Descriptive Part*, CERN EDMS No: 1145711

[25] CERN RP Service, *Safety Code*, CERN EDMS No: 335729 v.2, (2006)

[26] A. Ferrari, P.R.Sala, A. Fassò A and J. Ranft, (2005) *FLUKA: a multi-particle transport code*, CERN 2005-10, INFN/TC_05/11, SLAC-R-773

[27] G. Battistoni, S. Muraro, P.R. Sala, F. Cerutti, A. Ferrari, S. Roesler S, A. Fassò and J.Ranft, (2007) *Proceedings of the Hadronic Shower Simulation Workshop 2006 (Fermilab 6–8 September 2006)* ed M Albrow and R Raja (AIP Conference Proceeding 896) 31–49

[28] V.Vlachoudis, *FLAIR: A powerful but user friendly graphical interface for FLUKA*,Proceedings of the International Conference on Mathematics, Computational Methods and Reactor Physics,M&C2009,Saratoga Springs,New York, 2009

[29] L. Sarchiapone, M. Brugger, B. Dehning, D. Kramer, M. Stockner and V. Vlachoudis, *FLUKA Monte Carlo simulations and benchmark measurements for the LHC beam loss monitors*, Nucl. Instruments and Methods in Physics Research A 581 (2007) 511-516

[30] A. Borio di Tigliole, A. Cesana, R. Dolfini, A. Ferrari, G.L. Raselli, P. Sala and M. Terrani, *FLUKA simulations for low-energy neutron interactions and experimental validation*, Nucl. Instruments and Methods in Physics Research A 469 (2001) 347-353

[31] M. Brugger, A. Ferrari, S. Roesler and L. Ulrici, *Validation of the FLUKA Monte Carlo code for predicting induced radioactivity at high-energy accelerators*, Nucl. Instruments and Methods in Physics Research A 562 (2006) 814-818

[32] C. Theis, K. H.Buchegger, M. Brugger, D. Forkel-Wirth, S. Roesler, H. Vincke, *Interactive three dimensional visualisation and creation of geometries for Monte - Carlo calculations*, Nuclear Instruments and Methods in Physics Research A 562, 827-829 (2006).

[33] A. Christov and V. Vlachoudis, *Fluka Simulations for the HiRadMat dump*, CERN Internal Note, *Private Communication*.

[34] A. Vasilescu, *The NIEL scaling hypothesis applied to neutron spectra of irradiation facilities and in the ATLAS and CMS SCT*. CERN Reference: ROSE/TN/97-2.

[35] D. Kramer, M. Brugger, V. Klupak, C. Pignard, K. Roeed, G. Spiezia, L. Viererbl, T. Wijnands, *LHC RadMon SRAM detectors used at different voltages to determine the thermal neutron to high energy fluence ratio*, RADECS 2010 Proceedings.

[36] C. Theis et al, EDMS No: 1070443.

[37] H. Vincke, *Remnant dose rates in the area of a TCDI collimator after 200 days of normal operation and after an accidental beam loss*, CERN-SC-2004-018-RP-TN

[38] N. Charitonidis, I. Efthymiopoulos, C. Theis and H. Vincke, *Prompt, Activation and Background Radiation Studies for the HiRadMat facility of CERN/SPS*, CERN EDMS No: 1144976

[39] N. Charitonidis, C. Theis and S. Roesler, *Radiological Assessment of the Collimator Materials Tests at HiRadMat in 2012*, CERN EDMS No: 1211485

[40] N. Charitonidis and I. Efthymiopoulos, *Radiological Assessement of the Tungsten Powder Test (HRM10) at HiRadMat*, CERN EDMS No: 1218683 v.1

[41] N. Charitonidis and C. Theis, *Activation Studies for HRM-12 Experiment*, CERN EDMS No: 1224528 v.1

[42] Federal Swiss Authorities, *Swiss Legislation Law: Radiological Protection Ordinance (RPO) "RS814.501 Ordinance du 22 Juin 1994 sur la radioprotection (ORaP)*

[43] H. Vincke, D. Forkel-Wirth, D. Perin and C. Theis, *Simulation and Measurements of the Response of an Air Ionisation Chamber Exposed to a Mixed High-Energy Radiation Field*, Radiation Protection Dosimetry (2005), Vol. 116, No 1-4, pp. 380-386.

[44] International Commission on Radiation Units and Measurements, *Average Energy Required to Produce an ion pair*, ICRU report 31 (Washington, DC), 1979

[45] CERN's Timber Logging System, *http://www.cern.ch/timber*

[46] H. Kirk, *Targetry for a* $\mu^+\mu^-$ *collider*, Proceedings of the 1999 Particle Accelerator Conference, New York, 1999

[47] H.G. Kirk, V.B Graves, K.T. McDonald, C.J. Densham, P. Loveridge, F. Ladeinde, Y. Zhan, J. Back, V.B Graves, *A 4-MW Target Station for a Muon Collider or a Neutrino Factory*, Proceedings of IPAC'10, Kyoto, Japan. Ref: WEPE101.

[48] B.J. King, S.S. Moser, R.J. Weggel, N.V. Mokhov, Proceedings of the 1999 IEEE Particle Accelerator Conference, New York City, NY, USA, IEEE 99Ch36366, 29 March–2 April, 1999, p. 3041.

[49] J.R.J. Bennett, AIP Conf. Proc. 542 (2000) 253.

[50] G.S. Bauer, *SINQ-Status Report Oct. 1990*, Proc. ICANS-XI, Tsukuba, 1990 KEK report 90-25 (1991) p.41-60

[51] D J S Findlay et al, *ISIS Upgrades - A status report*, Proceedings of HB2006, Tsukuba, Japan, Reference: MOBP01.

[52] P. Hurth, O. Caretta, T. Davenne, C. Densham, P. Loveridge and N. Simos, *High - Power Targets: Experience and R&D for 2MW*, arXiv:1208.2681

[53] P. Hurth, A. Ammigan, B. Hartsell, R. Tschirhart, *Targetry Challenges at Megawatt Proton Accelerator Facilities*, Reference: THPFI082

[54] K. Haga et al, 2004, *Mercury Target and its Peripheral Devices for 1 MW Spallation Neutron Source*, Proc. of ICONE-12, Washington DC, USA, Paper 49518

[55] P. Sievers, *A stationary target for the CERN-neutrino factory*. Nuclear Instruments and Methods in Physics Research A 503 (2003) 344–347

[56] O.Caretta, C.J.Densham, P. Loveridge and T.W.Davies and R.Woods, *The potential of fluidised powder target technology in high power accelerator facilities*, Proceedings of PAC09,Vancouver, BC, Canada, REF: WE1GRC04

[57] C.Lu and K.T. McDonald, *Flowing Tungsten Powder for Possible Use as the Primary Target at a Muon Collider Source*, Princeton/μμ/98-10, 1998

[58] S. Ozaki, R. Palmer, M. Zisman and J. Gallardo, *Feasibility Study-II of a Muon-Based Neutrino Source*, ed., BNL-52623(2001)

[59] O.Caretta, C.J.Densham, T.W.Davies and R.Woods. Preliminary Experiments on a Fluidised Powder. Proceedings of EPAC 2008, Genoa, Italy,23-27 Jun 2008.

[60] RedLake, *MotionXtra User's Manual,version 3.5.4*, http://www.idtvision.com/documents/hg_cam_user_man.pdf

[61] H. Richter, *Simulating Transient Effects of Pulsed Beams on Beam Intercepting Devices*, PhD Thesis, CERN-THESIS-2011-171

[62] Polytec, *OFV - 505/503 Vibrometer Sensor Head*, http://www.polytec.com/fileadmin/user_uploads/Products/Vibrometers/OFV-50X/Documents/OM_DS_OFV505_2012_06_1000_E.pdf

[63] Polytec, *OFV - 5000 Vibrometer Controller*, http://www.polytec.com/fileadmin/user_uploads/Products/Vibrometers/OFV-5000/Documents/EN/OM_DS_OFV5000_2010_06_E.pdf

[64] N. Charitonidis, I. Efthymiopoulos, *Radiological Assessment of the Tungsten Powder Test (HRMT-10) at HiRadMat*, EPFL-REPORT-182081.

[65] J.W. Cooley and J. W. Tukey, *An Algorithm for the Machine Calculation of Complex Fourier Series*, Mathematics of Computation, Vol.19,No.90 (1965), pp 297-301.

[66] Tipler P.A, Mosca G, *Physics for Scientists and Engineers*, 5ed extended version, W.H. Freeman, 2008

[67] O. Caretta, T. Davenne, P. Loveridge, M. Fitton, J.O'Dell and C.J. Densham, I. Efthymiopoulos & N. Charitonidis, *Analysis of LDV data recorded during proton beam irradiation of tungsten powder*, 01/11/2012, HPT/2012/5.

[68] A.W. Ruff, S.M Wiederhorn, *Erosion by Solid Particle Impact*, NBSIR-78-1575, Interim Report, January 1979.

[69] C. Pourreuix, *Strength of glass eroded by round particles*, Nat.Lab Unclassified Report 029/97, Phillips Electronics.

[70] J. Back, *Pion and muon yields from a 10 GeV proton beam on various targets*, Proceedings of Science, 10th International Workshop on Neutrino Factories, Super Beams and Beta beams, June 30 - July 5 2008, Valencia, Spain, ref: arXiv:0812.3520

Curriculum Vitae

PERSONAL INFORMATION

CHARITONIDIS Nikolaos

74, Rue de Meyrin, F-01210, Ferney – Voltaire, France
☎ +41227679075 +41767391209
nikolaos.charitonidis@cern.ch
http://cern.ch/ncharito

Sex: **Male** | Date of birth: **06/04/1983** | Nationality : **Greek/ Cypriot**

WORK EXPERIENCE

2010 – TODAY

CERN Doctoral Student - University : EPFL Lausanne

EN/MEF group, LE Section.

Supervisors : *Dr. I. EFTHYMIOPOULOS & Prof. L. RIVKIN*

- PhD Student
- Member of HiRadMat Design & Operation Team
- Responsible for the Radiation Protection studies for all HiRadMat Experiments
- Responsible for the design, performance & data analysis of HRM-10 experiment
- Responsible for the design, performance & data analysis of HRM-15 experiment
- Participation in CERF measurements in CERN north area

2009 – 2010

CERN Unpaid Associate

DG/KTT group, LS Section.

Supervisors: *Dr. M. SILARI, Dr. F. CERUTTI, Dr. M. DOSANJH & Prof. E. GAZIS*

- MSc student
- Intercomparison of software databases used in Hadron Therapy
- FLUKA Simulations for near accelerator components material database

2008 – 2009

University Research Assistant

National Technical University of Athens - School of Electrical & Computer Engineering.

- Diploma (MSc Equivalent) Student
- Research Assistant of "BioSim" laboratory
- Full participation in the project : EEG analysis and prediction of Epileptic Seizures

2006 – 2009

Computer Systems Administrator / Technician

National Technical University of Athens - School of Applied Mathematics & Physics

- Voluntary Member of GR-03-HEPNTUA GRID cluster
- Computer Software / Hardware & Network Development & Administration support of the members of the department
- Design, Setup & Administration of the departmental Web Server – *http://www.physics.ntua.gr*

EDUCATION AND TRAINING

2010 - 2013

PhD in Applied Physics

Ecole Polytechnique Fédérale de Lausanne (EPFL) - To be obtained in 2014

- Thesis Title: “Design Optimisation of a High Intensity Beam Facility & Feasibility Experiment of a Solid Fragmented Target”

2008 – 2010

MSc in Physics & Technological Applications

National Technical University of Athens – School of Applied Mathematics & Physics - School of Mechanical Engineering - Research Center “Demokritos”

- Interdisciplinary Post Graduate Program in Advanced Physics
- Overall grade: 8.68/10.0
- Thesis title: “Hadron Therapy: A study on Grid Databases and Monte Carlo Simulations” (graded: 10.0/10.0)

2001 – 2008

Diploma in Applied Physics

National Technical University of Athens – School of Applied Mathematics & Physics

- Majors in : Nuclear & Particle Physics & Optoelectronics and Lasers
- Thesis Title: “Computational Methodologies in Research and Management of Large Amount of Video - Electroencephalographic Data” (graded: 10.0/10.0)
- Overall grade: 7.47/10.0

SCIENTIFIC PUBLICATIONS

Peer reviewed journals

S. Agosteo, R.Bedogni, M.Caresana, ***N.Charitonidis****, M.Chiti, A.Esposito, M.Ferrarini, C. Severino, M.Silari, “Characterisation of extended range Bonner Sphere Spectrometers in the CERF high-energy broad neutron field at CERN”, Nuclear Instruments and Methods in Physics Research A 694 (2012) 55–68*

T. Alexopoulos , F. Cerutti , ***N.Charitonidis****, E.Gazis, M.Kokkoris, E.Skordis, A. Tsinganis , G.Tsipolitis, R.Vlastou, “Experimental study and FLUKA simulations of a prototype micromegas chamber in a mixed neutron and photon radiation field”, Nuclear Instruments and Methods in Physics Research A 677 (2012) 52–60*

N. Charitonidis*, A. Bertarelli, M. Guinchard et al “An Experiment to Test Advanced Materials Impacted by Intense Proton Pulses at CERN HiRadMat Facility“, Nuclear Instruments and Methods in Physics Research B 308 (2013) 88–99*

N. Charitonidis*, M. Silari, G. Manessi et al, « Intercomparison of 5 Neutron Detectors in HiRadmat Facility”. Under preparation, to be published Radiation Measurements, 2013*

N. Charitonidis*, I. Efthymiopoulos, C. Densham, O. Caretta, et al “Observations from the HRM-10 experiment at CERN/SPS “ under preparation, to be published, Physical Review E, 2013*

Conference Proceedings

N. Charitonidis*, I. Efthymiopoulos, A. Fabich et al. “A Feasibility Experiment of a W-powder target in the HiRadMat facility at CERN”, 4th International Particle Accelerators Conference, Shanghai, China, 11-17 May 2013*

N. Charitonidis*, I. Efthymiopoulos, A. Fabich et al. “First Year of Operations in the HiRadMat Irradiation Facility at CERN”, 4th International Particle Accelerators Conference, Shanghai, China, 11-17 May 2013*

J. Blanco Sancho, ***N. Charitonidis****, I. Efthymiopoulos, F. Burkart and C. Maglioni (Eds.) et al. “An Experiment on Hydrodynamic Tunneling of the SPS High Intensity Proton Beam at the HiRadMat Facility”, 52nd ICFA Advanced Beam Dynamics Workshop on High-Intensity and High-Brightness Hadron Beams, Beijing, China, September 17-21, 2012*

N. Charitonidis*, I. Efthymiopoulos, H. Vincke, M. Lazzaroni and M. Meddahi et al. “HiRadMat: A*

New Irradiation Facility For Material Testing At CERN". Second International Particle Accelerator Conference (IPAC´11), Kursaal, San Sebastian, Spain, 4 to 9 September, 2011.

***N. Charitonidis**, F. Cerutti and M. Silari, "Neutron double differential distributions, dose rates and specific activities from accelerator components irradiated by 50 – 400 MeV protons", SATIF-10 International Conference, June 2-4, 2012, CERN, Geneva, Switzerland.*

CERN ATS Notes

*A. Bertarelli, E. Berthome, V. Boccone, F. Carra, **N. Charitonidis**, et al. "An Experiment to Test Advanced Materials Impacted by Intense Proton Pulses at CERN HiRadMat Facility, CERN-ATS-Note-2013-005 TECH*

CERN Internal Publications

***N. Charitonidis**, G.P Manessi & M. Silari, "Test Run for the HRMT-15 (RPINST) experiment ", CERN-DGS-2012-092-RP-TN*

***N. Charitonidis**, G.P Manessi & M. Silari, "Experimental Proposal: Test of radiation protection instrumentation in HiRadMat ", EPFL-REPORT-181193*

***N. Charitonidis**, C. Theis & S. Roesler, "Radiological assessment of the "Collimator Materials test" at HiRadMat in 2012", CERN-DGS-2012-019-RP-TN*

***N. Charitonidis**, I. Efthymiopoulos, C. Theis & H. Vincke "Prompt, Activation and Background radiation studies for the HiRadMat facility of CERN/SPS", EDMS no: 1144976*

***N. Charitonidis**, & I. Efthymiopoulos, "Radiological Assessment of the Tungsten Powder Test (HRM10) at HiRadMat", EPFL-REPORT-182081*

Conference Talks / Posters

***N. Charitonidis,** I. Efthymiopoulos, C. Densham, O. Caretta, M. Fitton, P. Loveridge, T. Davenne & Joe O'Dell, "First observations from the HRM-10 tungsten powder experiment at HiRadMat". 8th International Workshop on Neutrino Beams & Instrumentation, CERN, Geneva, Switzerland (talk)*

***N. Charitonidis**, I. Efthymiopoulos, O. Caretta, T. Davenne and C. Densham et al.* « Feasibility Experiment of Granular Target Options for Future Neutrino Facilities". *XIIth International Workshop on Neutrino Factories, Super beams and Beta beams, Geneva, Switzerland, August 1-6, 2011 (poster)*

***N. Charitonidis**, I. Efthymiopoulos, L. Rivkin, O. Caretta and P. Loveridge et al.* Feasibility Experiment for a High Power Fragmented Solid Target in the HiRadMat Facility at CERN. *4th High Power Targetry Workshop, Malmoe, Sweden, May 2-6, 2011, (talk)*

Summer Schools / Continuing Education

- *CERN Introductory Accelerator School, Varna, Bulgaria (2010)*
- *CERN Advanced Accelerator School, Chios, Greece (2011)*

Doctoral School Courses

- *Particle Detection, EPFL Doctoral School (grade: 5.5/6.0)*

PERSONAL SKILLS

MOTHER TONGUE

Greek

OTHER LANGUAGES

	UNDERSTANDING		SPEAKING		WRITING
	LISTENING	READING	SPOKEN INTERACTION	SPOKEN PRODUCTION	
English	**C2**	**C2**	**C2**	**C2**	**C2**
French	**B1**	**B2**	**B2**	**B2**	**B2**

Levels: A1/2: Basic user - B1/2: Independent user - C1/2 Proficient user
Common European Framework of Reference for Languages

COMPUTER SKILLS

Experienced user of **scientific software packages:**

- FLUKA® Monte - Carlo code
- MADX (Beam Line Optics Software)
- SimpleGeo® 3D Visualiser of Monte – Carlo Geometries
- Wolphram Mathematica ®
- Matlab® (Signal Processing)
- SPECTR (gamma-ray spectroscopy analysis)
- Originlab Origin ® (data/statistical analysis)
- MS Office software suite

Experienced user of **web design software packages:**

- Dreamweaver (web design)
- Adobe Photoshop (image processing)
- Google SketchUp (basic 3D design)
- Video editing with miscellaneous software

Experienced user of **system administration & networking software packages**

- Apache Web Server
- Bind (Network domain server)
- Sendmail (Mail server)
- MySql (Database server)
- Nagios (Network monitoring server)
- phpBB (Electronic forum software)
- IRCd (Online chat server)

Programming Languages

- C++
- Pascal
- Visual Basic
- shell scripting
- HTML
- XHTML
- CSS
- LaTeX typesetting engine

Operating Systems (user and administrator)

- MS Windows (all versions)
- Linux (most of the distributions)
- FreeBSD, OpenBSD, NetBSD
- Sun Solaris

Hardware

- Experienced administrator of computer hardware
- Experienced user of scientific hardware (NIM crates, data acquisition systems)

ORGANISATIONAL / MANAGERIAL SKILLS

- Member of organising committees & technical support in many conferences during my studies
- Students’ supervision in several cases (Nat. Tech. University of Athens & CERN)
- Official CERN guide & First Aider
- Attended Leadership Course in 2009 in Surrey, England.

MISCELLANEOUS

- Driving License category B
- European Computers Driving Licence (ECDL)
- Song & Music theory teacher. Knowledge of piano
- Participation in semi-professional choir